Advances in Hydraulic Fracture Simulation - Dynamic and Quasi-static Analysis

by

Matin Parchei Esfahani

A thesis
presented to the University of Waterloo
in fulfillment of the
thesis requirement for the degree of
Doctor of Philosophy
in
Civil Engineering

Waterloo, Ontario, Canada, 2019

Examining Committee Membership

The following served on the Examining Committee for this thesis. The decision of the Examining Committee is by majority vote.

External Examiner:	Dr. Haim Waisman Associate Professor, Dept. of Civil Eng., Columbia University
Supervisor(s):	Dr. Robert Gracie Associate Professor, Dept. of Civil and Environmental Eng., University of Waterloo
Internal-External Member:	Dr. Maurice Dusseault Professor, Dept. of Earth and Environmental Sciences, University of Waterloo
Internal Member:	Dr. James Craig Associate Professor, Dept. of Civil and Environmental Eng., University of Waterloo
Internal Member:	Dr. Dipanjan Basu Associate Professor, Dept. of Civil and Environmental Eng., University of Waterloo

Author's declaration

I hereby declare that I am the sole author of this thesis. This is a true copy of the thesis, including any required final revisions, as accepted by my examiners.

I understand that my thesis may be made electronically available to the public.

Abstract

Hydraulic fracturing (HF) is an effective technique for permeability enhancement of conventional and unconventional reservoirs. HF is performed by injecting a fluid (usually water-based), sand, and chemicals into a formation under high pressure in order to induce damage and improve the interconnectivity of the fracture network through reopening of natural fractures and generation of new fractures. Hydraulic fracturing is a complex multi-physics process that involves the coupling of several physical phenomena, such as rock deformation, fluid flow, fracture propagation, etc.

The simulation of HF is complex due to its coupled multi-physics nature. Despite recent advancements in HF simulations, relatively little attention has been given to improving the coupling algorithms used in these simulations. In many cases, sequential coupling algorithms are preferred over the monolithic approach due to the availability of independent solvers for each subproblem (e.g., independent deformable solid and fluid flow models), and the costliness of the monolithic approach. However, the available sequential algorithms widely used in the simulation of hydraulic fractures are known to lack robustness and encounter stability and/or convergence issues. The unavailability of efficient and effective sequential algorithms for the simulation of hydraulic fractures is currently one of the major gaps in the literature.

The majority of hydraulic fracture models use quasi-static analysis, which neglects the inertial effects that are important when injection rates are very high or vary quickly in time, as during stimulation by pressure pulsing. The application of the dynamic models currently available in the literature is mainly limited to the dynamic simulations of acoustic wave emissions in porous media. Very few studies, until now, have considered dynamic simulation of fluid driven fractures. Hence, the unavailability of reliable dynamic hydraulic fracture models is another major gap in the hydraulic fracture literature.

This thesis has three objectives. The first objective is to develop a stable sequential coupling algorithm for enforcing the hydro-mechanical coupling in the simulation of hydraulic fractures. The focus of the first objective is on the sequential algorithms that solve the mechanics subproblem first, in each iteration. This objective is realized in Chapter 2 of the thesis. The split is derived using the analogy of the undrained split in poromechanics; hence the new algorithm is named the *undrained HF split*. The undrained HF split converges to the solution of the fully coupled (monolithic) approach. It's also shown to be stable and convergent in applications in which the conventional coupling strategies fail to converge due to oscillations. The convergence of the undrained HF split is generally slower than the fully coupled model.

The second objective of the thesis is to develop a stable sequential coupling algorithm that solves the fluid flow subproblem first, in each iteration. This objective is addressed in Chapter 3 of the thesis. This algorithm is derived using the analogy of the fixed stress split in poromechanics and, therefore, named the *fixed stress HF split*. The fixed stress HF split is stable and shown to converge to the solution of the fully coupled model. The algorithm is shown to successfully simulate nonplanar hydraulic fracture trajectories in flow rate controlled hydraulic fracture simulations.

The third objective of the thesis is to develop a dynamic hydraulic fracture model for investigating the effect of rapidly changing loads, such as those caused by pressure pulses, on the dynamic propagation of hydraulic fractures. Chapter 4 of the thesis addresses this objective. A dynamic HF model with leak-off is developed in Chapter 4. The dynamic HF model is used to study wellbore stimulation by high rate and high amplitude pressure pulses and investigate the effect of formation porosity and permeability on the dynamic response of the system. It is observed that generally, formations with higher porosity and permeability generate shorter and wider hydraulic fractures. The dynamic response of hydraulic fractures is found to contain a phase lag with respect to the applied pressure pulse, which slightly increases with an increase in the porosity and permeability of the formation. Fracture closure mechanism is directly affected by the rate of fluid leak-off from hydraulic fractures, which also depends on the porosity and permeability of the formation. Unique acoustic wave emission patterns are observed from the response of hydraulic fracture and wellbore system to the pressure pulse at each stage of the stimulation.

Acknowledgements

I would like to thank my supervisor, Dr. Robert Gracie, for his guidance and continuous support throughout my time as his student. I would also like to thank the committee members for reviewing this thesis.

I must express my gratitude to my wife, Mahsa, for her eternal love and support. Without her, nothing is possible in my life.

Dedication

To the memory of my beloved mother who was expecting this day

To my better half, Mahsa, my father, and my grandparents

Table of Contents

List of Figures

List of Tables

List of Abbreviations

APM Analogous Porous Medium

BEM Boundary Element Method

CHSIE Complex Hypersingular Equation

CPU Central Processing Unit

DEM Discrete Element Method

DN Dirichlet to Neumann

FC Fully Coupled

FDM Finite Difference

FDEM Finite-Discrete Element Method

FEM Finite Element Method

FSN Fixed Strain

FSS Fixed Stress

FVM Finite Volume Method

GFEM Generalized Finite Element Method

HF Hydraulic Fracture

KGD Khristianovic-Geertsma-de Klerk

LBB Ladyzenskaja-Babuška-Brezzi

LEFM Linear Elastic Fracture Mechanics

ND Neumann to Dirichlet

ODE Ordinary Differential Equation

PDE Partial Differential Equation

PKN Perkins-Kern-Nordgren

P3D Pseudo Three-Dimensional

XFEM Extended Finite Element Method

Chapter 1

Introduction

1.1 An Introduction to Hydraulic Fracture Simulations

The oil and gas industry has significantly changed during the recent decades due to the availability of the technology which enables economic exploitation of unconventional reservoirs. Unconventional resources are known to be the future of oil and gas supply in North America and all around the world [5]. A study by Hartley and Medlock in 2010 [112] has predicted a rapid increase of production from unconventional resources, shale gas in particular, for a period of thirty years until 2040. Their model suggests that the production from shale gas in North America increases from about 2.3 *tcf* in 2010 to about 3.0 *tcf* in 2015 and to more than 14 *tcf* in 2040. It is important to know that the actual natural gas production from shale gas only in the United States has been about 13.6 *tcf* (37.4 *Bcf/d*) in 2015 [34], which is about three times more than the amount predicted by Hartley and Medlock for 2015 in North America. The Annual Energy Outlook 2016 predicts U.S. natural gas production from shale gas to be about 29.2 *tcf* (80 *Bcf/d*) in 2040. U.S. tight oil production is also predicted to increase from about 4.8 million *b/d* in 2015 to more than 7.0 million *b/d* in 2040 [34]. Such a significant increase in production indicates the important role of unconventional resources in the future of oil and gas industry.

Production of natural gas from shale gas is one of the major types of production from unconventional reservoirs in North America [4]. In a shale gas reservoir, natural gas is trapped in relatively low permeability shales. Low permeability of the shale formation is a barrier against free migration of natural gas towards production wells. Hydraulic fracturing is an effective technique for enhancing the permeability of shale gas reservoirs

and maximizing the production rate.

The development of analytical models for hydraulic fracturing dates back to the 1950s when analytical solutions were presented for propagation of simple pressure-driven fractures (e.g. [28, 59, 66, 156]). The problem of hydraulically induced fracture propagation can only be analytically solved for a limited range of simple cases, such as the propagation of planar fractures in homogeneous media, which are unable to describe complex practical problems. The emergence of powerful computers in the 1970s encouraged development of semi-analytical and numerical models for the simulation of hydraulic fractures (e.g [102, 31]). Today, computer simulators are capable of modeling a geomechanical process in different scales from molecular scale to the scale of a reservoir. Such simulators are employed to present a more realistic understanding of geomechanical processes, which cannot be replicated in laboratory, and problems that are too complicated to be solved analytically. It is worth mentioning that there is always uncertainty associated with the input data fed to the simulators. The output data also contain uncertainty associated with the simplifying assumptions made in the model. Hence, the outcome of such computer simulations should also be used carefully.

Hydraulic fracturing is a coupled multi-physics problem. In its simplest form, hydraulic fracturing involves the interaction of the following three major processes[2]:

1. Mechanical deformation of the solid matrix

2. Fluid flow inside the fracture network and porous matrix

3. Propagation of hydraulic fractures (induced and natural fractures)

1.2 Hydraulic Fracture Models

In this section, a brief review of the existing solutions to the problem of hydraulically induced fracture propagation is presented. We discuss a number of analytical solutions which are useful in designing hydraulic fracture treatments as a first order estimate of the actual solution. A brief discussion of numerical models of hydraulic fracture is also presented and corresponding limitations in simulating a realistic hydraulic fracture model are elaborated. Finally, coupling strategies for the numerical solution of the coupled hydro-mechanical problem are presented followed by a short discussion about hydraulic fracture propagation.

1.2.1 Analytical and semi-analytical models of the hydraulic fracture

The first theoretical models of hydraulically induced fracture propagation were introduced in 1950s [2] when Sneddon's plain strain solution [130] for the opening of a stationary fracture under internal pressure forces was employed to develop simplified hydraulic fracture models. Such models were used to study mechanics of hydraulic fracturing [2, 59, 66] and effect of fluid properties on fracture aperture and propagation [64, 156]. The work by Perkins and Kern [110] followed by Nordgren's works [102] resulted in a model which accounts for fluid leak-off from fracture surfaces and is known as the PKN model. The independent work of Khristianoric and Zheltov [156] and Greetsma and De Klerk [47] developed the so-called KGD model. Sneddon also presented an analytical solution for the

problem of a radial fracture under constant pressure [129].

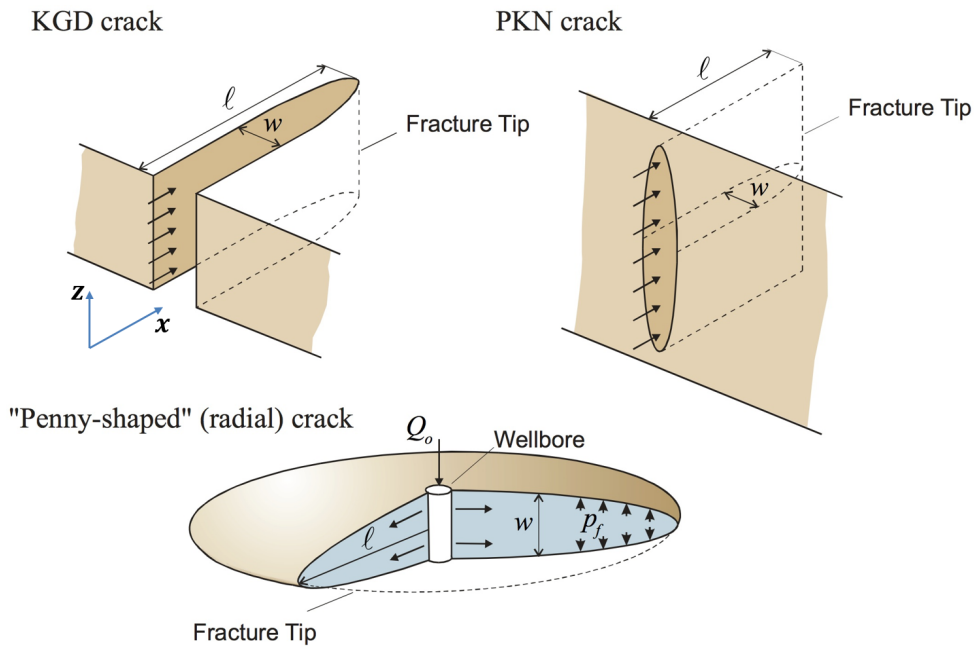

Figure 1.1: Analytical models of hydraulic fracture

Schematics of the PKN, KGD, and radial fracture models are illustrated in Figure 1.1. The PKN model assumes that each vertical cross section of the fracture is an ellipse of fixed height under plain strain conditions. Hence, the PKN model is applicable to long fractures whose length is considerably greater than their height [150].

In the KGD model, the horizontal cross section is assumed to be a half-ellipse under plane strain condition. Such an assumption makes the KGD model applicable to short fractures whose height is considerably greater than their length. Fracture aperture in a KGD model is independent of its height [150].

The radical fracture model is applicable to fractures initiated by injection from a point source in a homogeneous medium [150]. Later studies improved the KGD and PKN models,

for example, by taking into account the effect of non-linear fluid constitutive models [31] and fracture toughness [133].

The Barenblatt condition [12] is applied as the tip boundary condition in derivation of the KGD model in order to remove the stress singularity and develop a more realistic model. Barenblatt condition suggests that fracture aperture vanishes smoothly at the tip with slope of zero in oppose to the infinite slope of the fracture opening in an elliptical crack. Therefore,

$$\left.\frac{dw}{dx}\right|_{x=l} = 0 \tag{1.1}$$

where w, x and l are shown in Figure 1.1. Figure 1.2 compares the shape of the fracture tip for an elliptical fracture and a fracture with Barenblatt condition (cohesive crack).

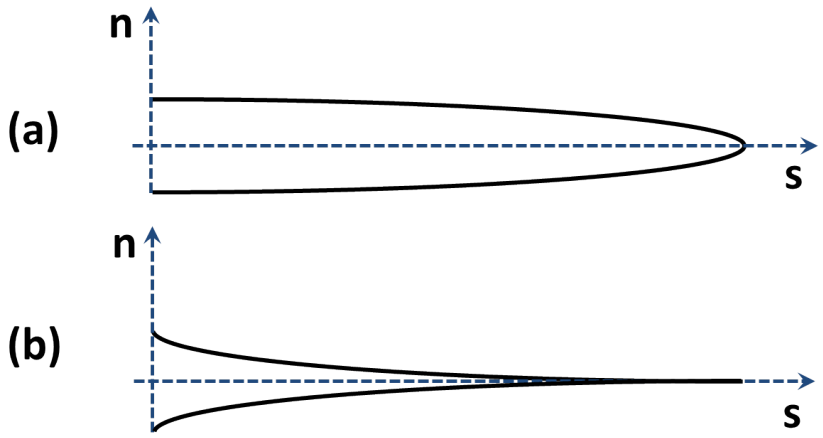

Figure 1.2: Shape of the crack tip for an elliptical crack (a) and a cohesive crack (b)

Hydraulic fracturing treatments were initially used for testing wellbore integrity or breaking the formation. In the 1970s, however, the rise in the price of oil and gas en-

couraged production from unconventional reservoirs which required far larger treatments compare to the initial applications of hydraulic fracturing [2]. Relatively high cost of such large treatments inspired new researches to develop more efficient models for hydraulic fracturing.

Development of pseudo three-dimensional (P3D) models was a simple, yet effective, attempt to extend the PKN model to simulate planer three-dimensional fractures propagating in layered media.

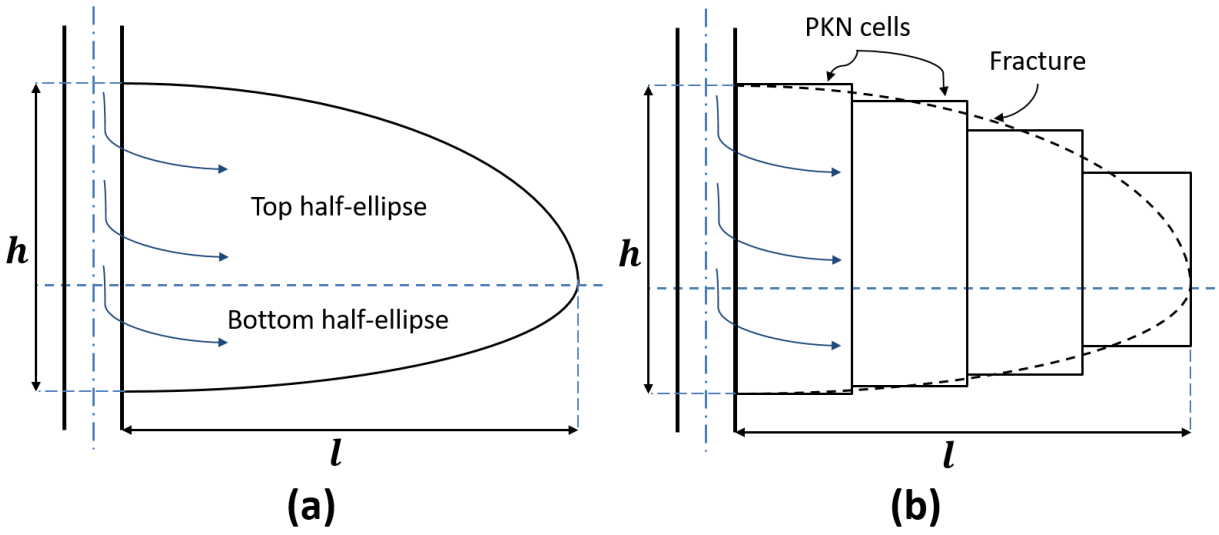

Figure 1.3: Pseudo 3D models of hydraulic fracture: Lumped elliptical model (a) and cell-based model (b) (redrawn after Adachi et al. [2])

There are two types of P3D models, as presented in [86] and illustrated in Figure 1.3:

- The *lumped elliptical model* in which fracture plane at each time step is represented by two half-ellipses of different heights joined along their major axis.

- The *cell-based model* in which fracture plane is represented at each time step by means of a number of discrete constant height PKN fracture cells.

In both types of the P3D model, fluid flow is considered to be one-dimensional along the fracture length [31]. Pseudo three-dimensional models are acceptable when propagation of planer fractures in a layered median with smoothly and monotonically varying properties is concerned [2]. For fractures with irregular shapes, e.g. hour-glass shaped fractures, or non-planar fractures propagating in highly heterogeneous media, such as naturally fractured rock formations, P3D models become deficient.

Availability of powerful computational resources facilitates employment of a number of robust computational methods to simulate hydraulic fractures under more complex conditions. In what follows, a review of the most important computational models of hydraulic fracturing is presented.

1.2.2 Computational models of hydraulic fracture

Boundary element models

The Boundary Element Method (BEM) is a numerical method commonly used for simulating fracture propagation (especially dynamic propagation). The BEM is attractive for simulation of long-term fracture propagation (such as hydraulic fracture propagation) due to its relatively lower computational cost compared to domain-based methods. This is because BEM discritizes only the crack boundary of the domain and the solution at each

point, $\mathbf{x}$, of the domain is computed by numerically integrating the effect of each point of the boundary on point $\mathbf{x}$ over the discretized boundary.

Such an approach requires derivation of analytical Green's functions which are hard to derive, if not impossible, for nonlinear problems or problems containing heterogeneity. BEM, therefore, has limitation in presenting realistic models of hydraulic fracturing, for example, with cohesive fractures or highly heterogeneous domains.

A number of recent studies on simulating hydraulically induced fractures using BEM have presented models to simulate arbitrary propagation of pressure driven fractures around a wellbore [97, 98], propagation of three-dimensional interface hydraulic fractures in layered media [152], arbitrary propagation of pressure driven fractures under non-uniform pressure and non-homogeneous stress fields [6], and interaction of multiple non-planer hydraulic fractures [146, 116, 117].

Finite element family of models

Finite Element (FEM) models, unlike BEM models, have no limitation in solving nonlinear problems. Finite elements models are capable of dealing with multiple nonlinearities, local or global, and are one of the most efficient numerical methods for modeling heterogeneous domains. In the conventional finite element method, a discontinuity is considered as an internal boundary of the domain and the space domain is discretized in accordance with all boundaries including the discontinuity. Evolution of a discontinuity is a moving boundary problem. A finite element model may deal with a moving boundary problem using either of the following two strategies:

1. Re-generating the mesh in accordance with the updated configuration of the moving boundary

2. Allowing the moving boundary to evolve only along the boundaries of the existing mesh

The first strategy is more accurate in terms of predicting the actual fracture trajectory, however, it is computationally far more expensive. The second strategy is the most commonly used technique in finite element models of hydraulic fracture propagation (e.g. [87]). The second technique is of lower accuracy in determining the fracture footprint and is highly mesh dependent. A sufficiently fine finite element mesh may lead to a sufficiently accurate fracture path; yet, with a considerable rise in the computational cost.

The finite element method is also weak in simulating the singular fracture tip. A dense mesh of singular elements is usually required in order to reproduce the singular stress field at the fracture tip [117]. Conversely, simulation of cohesive fracture tip is simply performed by employing cohesive elements, i.e. elements connected by means of a cohesive surface, which act as the potential fracture path in the model [103, 25]. The weakness of such an approach is that fracture path must be presumed *a priori* in order to determine the location of cohesive elements in the model. To address this issue, the cohesive traction-separation law is applied along all element boundaries in the domain [87]. As fracture propagates, using the second evolution strategy discussed above, cohesive surfaces located on the fracture path are activated and a smooth fracture evolution is achieved. The strategy, nevertheless, increases the computational cost as the cohesive law is applied globally along all element boundaries.

Conventional finite element models are also deficient in properly reproducing dynamic response of an elastic system to a high-frequency dynamic excitation [58] (for example the dynamic response to a shock wave). Such deficiency stems from employment of polynomial shape functions which are not capable of reproducing high-frequency oscillations under any circumstances [58]. Such a limitation becomes problematic in hydraulic fracture modeling when simulations of microseismic events induced by hydraulic fracturing operations are concerned.

Finite element simulators of hydraulic fracturing have commonly been used since the 1980s for simulating three-dimensional planar hydraulic fractures in homogeneous [26, 27, 141] and heterogeneous layered reservoirs [3], as well as three-dimensional non-planar hydraulic fractures [20].

Enriched partition of unity finite element methods (XFEM/GFEM) are sometimes employed to address limitations of FEM models in simulating propagating singular [96, 135] and cohesive [157] fractures as well as wave propagation in elastic media [58].

In an XFEM model, cohesive fractures are modeled by means of a cohesive traction-separation law applied only on a limited length of the fracture at its tip (i.e., cohesive zone). Hence, the computationally expensive process of applying the cohesive model to all element boundaries is avoided. Moreover, fracture propagation in an XFEM model is mesh independent; therefore, arbitrary fracture trajectories are modeled without any limitation. These are the two key functions of XFEM in simulating fracture propagation which make it an outstanding option for hydraulic fracture modeling.

An enriched approximation may also be used for fluid pressure if a discontinuity exists

in the pressure field (e.g., across the fracture in a fractured porous medium [115, 67, 11]) or when the asymptotic behavior of the pressure field is modeled (e.g, the pressure singularity at a singular fracture tip without a fluid gap [54]).

Application of XFEM/GFEM for simulating hydraulic fracture propagation is very new; however, a few advanced models for simulating hydraulic fracture propagation under complex conditions are developed recently. Mohammadnejad and Khoei [101, 99] used XFEM models for both fluid and solid matrix to present a fully coupled model of cohesive hydraulic fracture propagation in partially saturated porous media. Gordeliy and Peirce [54, 52] presented novel enrichment functions based on the asymptotic behavior of fluid pressure and fracture aperture in order to come up with an accurate model of singular hydraulic fractures propagating under a viscosity dominated regime. The enrichment functions are derived by means of an asymptotic analysis in order to achieve $\mathcal{O}(h^2)$ convergence rate in their novel sequential coupling strategy [53, 52].

Other researchers have employed XFEM/GFEM models to study propagation of multiple hydraulic fractures [109, 1], or to develop non-planar three-dimensional [56, 57], and multi-scale models [37, 106] of hydraulic fracture.

Discrete Models

Discrete models, in general, are models which consider the domain of analysis as an assembly of separate blocks. Discrete models are instrumental when solution to problems with multiple discontinuities are concerned. In a hydraulic fracture simulation, discrete models are employed to simulate parting of granular media (e.g. [136]) and preconditioning of

naturally fractured rocks (e.g [111]) or to model generation of a new fracture network in a continuum (e.g. [87]). A discrete model should possess the following two capabilities in order to be qualified for simulation of hydraulic fractures [29]:

1. The capability to compute all displacements of discrete blocks (including rotations)
2. The capability to detect contact detachments and the formation of new contacts

Discrete models may either use explicit time-domain integration (e.g. [29]) or implicit time integration (e.g. [65]).

The most common discrete methods in simulating geomechanical processes are *Discrete element methods* and *Hybrid finite-discrete element methods* [85].

Discrete element methods (DEM) In a discrete element method, the space domain is discretized into a finite number of blocks. Each block is also internally discretized and a finite element (FEM), finite difference (FDM), or finite volume (FVM) method is used to compute internal deformations of the block. External interactions of the blocks are modeled using unilateral and frictional contact conditions. When contact forces between two blocks surpass a threshold value, the contact breaks and the link between the blocks is removed. A fracture is assumed to be initiated when a contact link is broken. Fracture propagation is represented by coalescence of a number of broken contacts [85]. A schematic of the contact mechanism between two discrete elements is illustrated in Figure 1.4.

Hybrid finite-discrete element methods (FDEM) In hybrid finite-discrete element method, the domain is discretized as a continuum using, for example, FEM discretization.

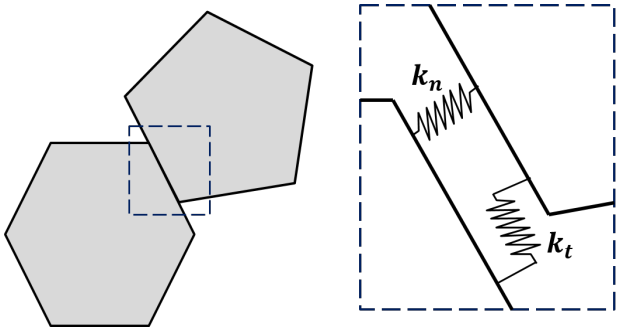

Figure 1.4: DEM contact between two blocks

The FEM model, solves the continuum problem for solid deformations and stresses. When the fracture criterion detects initiation of a new discontinuity, a discontinuous surface is formed between the elements. Interaction between the newly formed contacts is identical to block contacts in the DEM model [85]. A schematic of the FDEM model is presented in Figure 1.5.

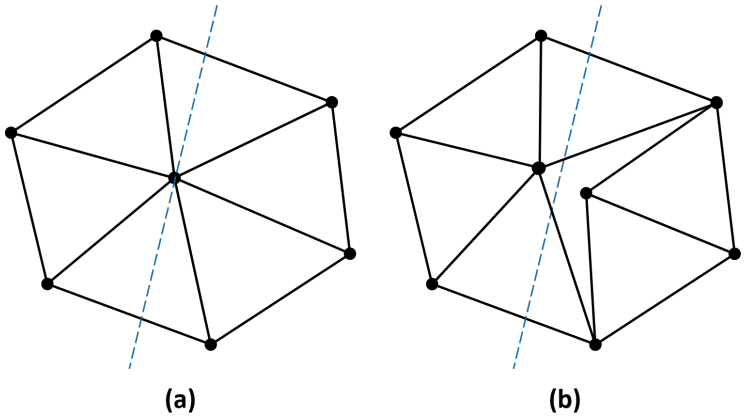

Figure 1.5: Formation of a discontinuity in an FDEM model (redrawn after Lisjak and Graselli [85])

Discrete models are commonly used for simulating the interaction between hydraulic fractures and existing fracture network in a fractured medium. Lisjak and Graselli [85],

have presented a comprehensive review of available discrete models for simulating a variety of geomechanical processes. A review of numerical models for simulating the interaction between hydraulic fractures and natural fracture network is presented in [30].

1.2.3 Hydro-mechanical coupling

The coupled hydro-mechanical problem can be numerically solved using either a fully coupled or an iterative scheme. The fully coupled approach solves the solid and fluid equations simultaneously, using an implicit time integration scheme. Although the fully coupled approach is the most robust [71], it involves the computation and inversion of big Jacobian matrices. Both tasks are nontrivial and computationally expensive. It also requires a unified hydro-mechanical solver which is costly to develop in most cases.

Numerous fully coupled hydraulic fracture models have been developed by means of the finite difference method (e.g [33]), the boundary element method (e.g. [131]), and the finite element family of methods (FEM/XFEM/GFEM)(e.g. [16, 100, 69, 57]).

Alternatively, one may choose to solve the coupled problem sequentially by solving either of the fluid or solid equations first, during each time step. The other equation is then solved using the solution of the first equation. Sequential coupling provides the advantage that each of the subproblem (solid or fluid) can be solved separately using robust specialized solvers tailored for their specific requirements. The process is iterated for each time step until convergence is achieved for the coupled system. Sequential coupling is, however, subject to stability and convergence problems regardless of stability and convergence of the scheme employed for each of the individual sub-systems.

Depending upon which subproblem is solved first, the sequential coupling approach is categorized under either of the following mapping families [52, 54]:

Dirichlet to Neumann (DN) mapping which solves the flow equation for fluid pressure first given the fracture aperture.

Neumann to Drichlet (ND) mapping which solves the solid equation first to determine solid deformations (and fracture aperture) given the fluid pressure.

Gordeliy and Peirce [52, 54] have shown that for an XFEM approximation with appropriate enrichment functions, the ND mapping converges with $\mathcal{O}(h^2)$ while DN mapping converges with $\mathcal{O}(h)$. Therefore, an ND mapping is strongly recommended by Gordeliy and Peirce [54] when XFEM is employed.

In order to separate the hydro-mechanically coupled system of equation, an operator splitting technique is required. In the context of poromechanics, four different operator splitting techniques have been introduced in the literature depending on the mapping (DN or ND) employed [70, 71, 92]. When the solid equation is solved first (ND mapping), the coupled system of equations can be separated using either a *drained* or an *undrained* split. In a drained split, which is the most intuitive, solid equation is solved at each time step given a fixed fluid pressure distribution ($\delta p = 0$) calculated at the previous time step. The fluid pressure is then updated for the current time step by fixing solid displacements ($\delta u = 0$). Conversely, in an undrained split, it is suggested that fluid mass content inside the porous matrix be conserved ($\delta \xi = 0$) when solid equation is solved at each iteration. The fluid pressure is then updated identical to the drained split at each iteration.

If fluid equation is solved first (DN mapping), either the fixed-strain or the fixed-stress

splits may be employed. In the fixed-strain split, the change in the volumetric strain of the solid matrix is assumed to be fixed ($\delta\varepsilon_v = 0$). The volumetric stress is assumed to remain unchanged in a fixed-stress split ($\delta\sigma_v = 0$).

Kim et al. [70] have shown that stability of the drained split is conditional while the undrained split can be unconditionally stable. Moreover, the drained split may not convergent when the number of iterations are fixed while an undrained split is always convergent when a compressible system is solved. As compressibility of the system decreases, the undrained split losses accuracy and becomes non convergent for an incompressible system [70]. The fixed-strain split is also conditionally stable whereas the fixed-stress split is unconditionally stable [71]. Kim et al. [71] also suggest that the fixed-stress split converges faster than the undrained split and remains convergent when incompressible systems are considered.

Sequential coupling strategies are more common in simulating hydraulic fractures as they are computationally less expensive compared to the fully coupled simulators. Examples of sequential coupling strategies are presented in [136, 53, 52, 9]. In the context of hydraulic fracture simulations, the split analogous to the drained split is labelled $P \rightarrow W$, and the one analogous to the fixed-strain is labelled $W \rightarrow P$ [52]. Splits analogous to the undrained split and fixed-stress split do not conventionally exist for the simulation of hydraulic fractures.

1.2.4 A brief discussion on hydraulic fracture propagation

In a fractured medium, hydraulic fractures tend to propagate in the direction of local weak planes (e.g. natural fractures) in order to minimize the work done against the local stress field. In large scale, however, the global orientation of the fracture tends to align with the orientation of maximum in-situ stress (perpendicular to the minimum in-situ stress) [39]. Figure 1.6 illustrates a schematic of the propagation path of a hydraulic fracture initiated from a wellbore in a rock formation containing natural fracture sets. As it is seen, small segments of the fracture conform the local orientation of natural fractures, while the hydraulic fracture in general aligns with the far field in-situ stress. Propagation of hydraulic fractures in a fractured medium mostly occurs in the form of re-opening of existing fractures. In a hydraulic fracture model, fracture propagation can be directly obtained from the solution of the hydro-mechanically coupled problem.

In a continuum model, the stress field at fracture front should be compared against a propagation criterion which determines whether and in which direction the fracture evolves. Propagation criterion should also estimate the length of fracture growth in order to fully determine the new configuration of fracture. In a quasi-static analysis, crack front is normally evolved in the direction defined by the propagation criterion to the point where fracture remains stable under the current state of stress. A dynamic model, requires the propagation criterion to determine the evolution velocity vector at the fracture front, $\mathbf{v}_f$, which shows the orientation and evolution length of the fracture during each time step.

The *maximum hoop stress* criterion is a common and widely accepted criterion in continuum based geomechanical models for brittle fracture propagation [134]. The fracture is

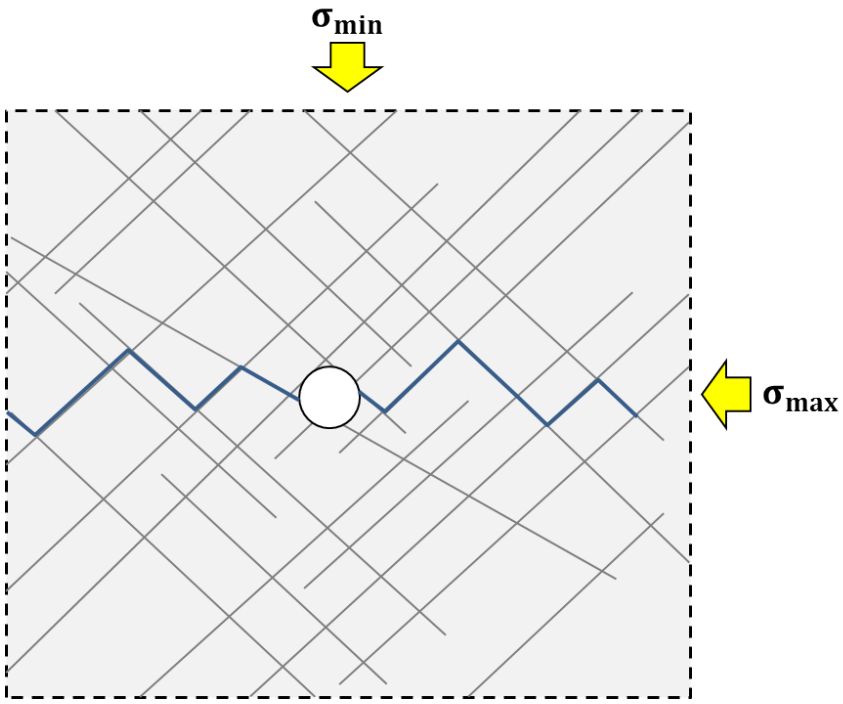

Figure 1.6: Propagation of hydraulic fracture: local vs global (redrawn after Dusseault [39])

allowed to propagate, based on this criterion, when the local maximum principal stress, σ_1, at the crack front reaches the tensile strength of the rock. The direction of propagation is the one in which hoop stress, $\sigma_{\theta\theta}$, reaches its absolute maximum.

1.3 Motivations

The fully coupled (monolithic) approach for enforcing the coupling is known to be the most robust coupling strategy. However, the fully coupled approach is computationally expensive as it contains the computation and inversion of a big Jacobian matrix, which are nontrivial

and computationally expensive tasks. Additionally, the availability of independent solvers for each of the engaged subproblems (e.g., independent deformable solid and fluid flow models), for many problems, inspires using the available solvers and enforcing the coupling through sequential algorithms.

The conventional sequential algorithms for the simulation of hydraulic fractures (the so-called $W \rightarrow P$ and $P \rightarrow W$) have been reported to be problematic [52]. The $W \rightarrow P$ and $P \rightarrow W$ algorithms are analogous to the fixed strain and drained splits in poromechanics analysis which are also known to lack robustness [71, 70, 91].

Contrary to the fixed strain and drained splits, in the context of poromechanics, the undrained and fixed stress splits are known to be robust splits with unconditional stability and good convergence [71, 70, 91]. Previous hydraulic fracture models, however, suffer from the lack of such robust sequential coupling algorithms. The robustness of the undrained and fixed stress splits in the poromechanics context motivates the attempt to develop analogous sequential coupling strategies for the simulation of hydraulic fractures.

The majority of the available hydraulic fracture models in the literature use quasi-static analysis in the simulation of hydraulic fractures. Quasi-static models are deficient in capturing the inertial effects generated by the rapidly changing loads, such as pressure pulses or impact. The induced seismicity due to fracture/fault reactivation and the propagation of hydraulic fractures cannot also be captured by quasi-static models of hydraulic fracturing.

A limited number of works within the literature (e.g.[75, 74]) have considered dynamic simulation of fractured porous media; however, the majority of them have not considered modeling fluid flow within the fractures. Fractures have been treated only as discontinuities

in both solid and fluid domains in these models.

Very few studies in the literature [144, 67, 18, 62] have considered using dynamic hydraulic fracture models to investigate the dynamic aspects of hydraulic fracture propagation, such as the induced seismicity. The limited number of available studies on the dynamic simulations of hydraulic fracturing motivates the research on the development of a dynamic hydraulic fracture model and further investigation of the inertial effects that are missing by the available quasi-static model.

1.4 Research Objectives and Methodologies

In this section, the objectives of the research and the methodologies employed to accomplish each objective are presented.

1: Develop a stable sequential coupling algorithm for hydraulic fracture simulations using the analogy of the undrained split in poromechanics

The extended finite element method is used to model the evolving fractures in the solid domain. The transient flow of a viscous fluid within the fractures is simulated using standard finite elements. A cohesive fracture tip model is used to simulate quasi-brittle fracture propagation. For the purpose of deriving the new sequential coupling strategy, the fracture is assumed to be replaced by an Analogous Porous Medium (APM), and the undrained HF split is developed using the local conservation of mass in the APM. The nonlinear system is solved using the Newton-Raphson method. This objective is fulfilled in Chapter 2 of the thesis which is based on the following article:

Parchei-Esfahani M., and Gracie R., On the Undrained and Drained Hydraulic Fracture Splits, *submitted to the International Journal for Numerical Methods in Engineering*

2: Develop a stable sequential coupling algorithm for hydraulic fracture simulations using the analogy of the fixed stress split in poromechanics

To derive the new sequential coupling algorithm, the fracture is substituted with an APM. The relation between fluid pressure and fracture aperture is derived within the APM using the theory of poroelasticity. The resulting nonlinear system is solved using the Newton-Raphson method. Flow partitioning between the fractures connected to a wellbore is performed by enforcing the global conservation of mass in the wellbore and fractures. This objective is realized in Chapter 3 of the thesis.

3: Develop a dynamic hydraulic fracture model with leak-off for the simulation of dynamic wellbore stimulation using pressure pulses

To develop a dynamic fracture model, the conservation of momentum is numerically solved over the discontinuous domain using the eXtended Finite Element Method (XFEM). A cohesive tip model with a non-recoverable damage flag is implemented to model fracture propagation under dynamic loading. To capture fracture closure, a linear contact model is applied to the fracture surfaces. The inertial terms in the fluid equation are neglected. A one-dimensional leak-off term, based on Carter's leak-off model, is implemented in the fluid equation to account for the volume of fluid leaking off from the fracture due to the permeability of the formation. The fully coupled solution strategy was used in the development of the dynamic hydraulic fracture model. Dynamic wellbore stimulation is investigated through the application of cyclic pressure pulses to the wellbore. This objective

is fulfilled in Chapter 4 of the thesis.

Chapter 2

Sequential Enforcement of Hydro-Mechanical Coupling: Undrained and Drained HF Splits

2.1 Introduction

The simulation of hydraulically induced fracture propagation involves coupling the physics of fluid flow in the fracture, the mechanical deformation of the fracture and surrounding domain, and the propagation of the fracture itself [2]. Hydraulic fracture simulations are governed by a hydro-mechanically coupled system of partial differential equations. Discretization of the governing equations in space and time leads to a system of coupled nonlinear algebraic equations that must be solved at each time step. In this chapter, we present a new and effective sequential iterative scheme, called the undrained HF scheme, for solving the resulting discrete system of equations and demonstrate that the most commonly used sequential scheme in HF simulation is unstable in many practical problems. The undrained HF scheme is introduced in the context of two-dimensional eXtended Finite Element Method (XFEM) simulations of hydraulic fracturing in impermeable domains.

Recent studies on hydraulic fracture modelling have mainly followed one of the two major trends [79]. The first trend focuses on improving the computational aspects of the models by employing state-of-the-art numerical techniques to develop models that overcome the limitations of their existing counterparts. Examples are studies that employed different variations of the boundary integral method [128, 147, 81, 51, 143, 155, 153, 116, 24], finite element method [120, 149, 19, 123, 124], extended/generalized finite elements [52, 53, 54, 78, 68, 40, 101, 100, 99, 119, 88, 56, 57, 61], phase field methods [93, 90, 89, 83, 145, 121], and hybrid Finite Element/eXtended Finite Element-Distinct Element techniques (FEM-DEM or XFEM-DEM) [113, 114, 148, 50] to develop 2D and 3D hydraulic fracture models. Additionally, some recent studies have coupled boundary integral or

extended finite element methods with fracture tip asymptotes and presented efficient multi-scale models of hydraulic fractures under different propagation regimes [108, 53, 82, 80, 106, 37]. The second trend focuses on enhancing the physical aspects of the models by incorporating more physics. Examples are studies that considered nonlinear fluid rheology and proppant transport [22, 36], hydraulic fracture propagation in porous media [15, 19], Acoustic Emissions [73], solid nonlinearity due to bulk plasticity and cohesive fractures [105, 104, 123], and non-local plasticity and damage models [94, 125]. For a detailed review of recent advances in the simulation of hydraulic fractures, the reader is referred to [79, 2, 85, 107, 60]. The focus of this chapter is on the first area of improving the numerical techniques used in HF models.

Despite many advances in the numerical models of hydraulic fractures, relatively little attention has been given to improving the solution algorithms, especially in the context of impermeable media. The many of published articles on the simulation of HF in impermeable media use a simple sequential iterative coupling scheme, which has been labelled the $P \rightarrow W$ scheme by Gordeliy and Peirce [52], will be referred to here as the drained HF split. In the sequential solution scheme that uses the drained HF split, the the equilibrium equation is solved first for the displacement and crack opening, assuming that the pressure is fixed, and then, fluid equation is solved for the fluid pressure, assuming that the fracture aperture is fixed [68, 52, 142, 137, 138, 15, 63]. Alternatively, coupling can be imposed through an approach labelled $W \rightarrow P$ by Gordeliy and Peirce [52]. This sequential approach solves the fluid equation under the assumption of a fixed fracture aperture. Subsequently, solid displacement and fracture aperture are updated by solving the solid equilibrium equation using the pressure obtained from the solution of the fluid equation.

Gordeliy and Peirce [52] have shown that XFEM is $O(h^2)$ accurate with the $P \rightarrow W$ scheme and only $O(h)$ accurate with the $W \rightarrow P$ scheme.

While previous articles have shown reasonable results using the drained HF split for some problems, our observations suggest that the scheme lacks robustness and fails to converge in some other applications. Specifically, our observations show convergence issues when simulating cohesive hydraulic fractures with moderate to low fracture energy (fracture toughness).

Gordeliy and Peirce [52] in their study (perhaps the only previous one) of HF coupling schemes described the drained HF split, which they labelled the $P \rightarrow W$ scheme, along with its counterpart, the $W \rightarrow P$ scheme, as being *problematic*. Here we will demonstrate again that the $P \rightarrow W$ scheme is unstable for non-toughness dominated HF. Gordeliy and Peirce [52] introduced a stable hybrid $P\&W$ scheme for linear elastic fracture mechanics HF models. In this chapter, we will present a new coupling scheme, the undrained HF split, which is applicable to non-linear fracture mechanics HF models with cohesive crack tips.

The most robust solution schemes for coupled systems (generally expected to have the highest convergence rate) are concurrent schemes and are often termed fully coupled schemes [159]. Despite the robustness of fully coupled models, sequential schemes based on operator splitting are preferable in many cases. For one thing, solving a fully coupled system often requires the development of an independent solver tailored to a specific coupled problem. In the case of nonlinear systems solved by Newton-Raphson, this involves both the derivation and implementation of a tangent stiffness (Jacobian) matrix (e.g.,

[57, 88, 99, 100]) - both tasks are non-trivial for complex systems. Moreover, fully coupled solvers (when compared to sequential solvers) require the computation, storage, and inversion of larger matrices which is computationally expensive, especially when the memory available is small compared to the needs of the analysis. Iterative sequential coupling schemes are particularly attractive when robust preexisting models are available for each of the processes to be coupled. In such cases, the coupled problem is split into individual subproblems that are then solved using the available software codes [159].

Methods for the simulation of poromechanics problems, e.g., consolidation of saturated porous media, offer useful analogies for HF simulation. In both cases, conservation of mass of the fluid and equilibrium of the solid must be simultaneously enforced. The simple sequential coupling algorithms in poromechanics are known as the drained and fixed-strain splits; these are respectively analogous to the $P \rightarrow W$ and $W \rightarrow P$ scheme used in some HF simulations. Both the drained and fixed-strain splits have been proven to encounter stability and convergence issues in poromechanics problems [71, 70]. Therefore, it is not surprising that the $P \rightarrow W$ and $W \rightarrow P$ splits used in HF simulation are also described in the literature as problematic [52].

To overcome the limitations of the drained and fixed-strain split used in poromechnics simulation, the undrained and fixed-stress splits were developed, which have been shown to be more robust than the drained and fixed-strain splits in terms of stability and convergence [71, 70, 92, 91]. In the undrained split of poromechanics, the displacement of the solid matrix is updated assuming that the fluid mass content within the solid matrix is fixed (instead of assuming that the pore pressure is fixed, leading to a drained split) [70].

In this chapter, we use the analogy of a porous media to introduce an efficient splitting scheme for HF simulation, which will be referred to as the *undrained HF split*. For the purpose of defining a sequential solution scheme, the fracture is assumed to be replaced by a virtual Analogous Porous Medium (APM), and a unique undrained HF split is derived for the first time for simulating hydraulic fractures in an impermeable medium.

The undrained HF split is implemented within a two-dimensional extended finite element method (XFEM) model of HF in an elastic solid. The continuity equation and the cubic law are used in a finite element framework to model fluid flow within the fractures. We use a cohesive fracture tip model to take into account the energy dissipated at the fracture tip when it propagates. Such energy dissipation is due to the development of a damaged region ahead of the fracture tip when the fracture is loaded by the fluid. We also account for the permeability enhancement within this damaged region by applying a minimum hydraulic aperture to the cubic law in the cohesive zone.

In what follows, we first explain the mathematical formulation of the hydro-mechanically coupled system along with the numerical discretization used for each of the domains of the problem. Next, we discuss the solution strategies and introduce the undrained HF split using the concept of an analogous porous medium. The numerical examples, in Section 4, demonstrate the effectiveness of the undrained HF split through comparison with fully-coupled and the drained HF split ($P \rightarrow W$) commonly used in the literature. A discussion and summary conclude the chapter.

2.2 Mathematical Model

2.2.1 Governing equations

Consider the solid domain, Ω_s, as illustrated in Figure 4.1. The domain is bounded by Γ, defined as $\Gamma = \Gamma_u \cup \Gamma_t \cup \Gamma_c$, such that $\Gamma_u \cap (\Gamma_t \cup \Gamma_c) = \varnothing$, in which Γ_u and Γ_t represent the Dirichlet and Neumann boundary of the domain, respectively, and Γ_c is its internal fracture boundary. The positive and negative faces of the fracture boundary are denoted by Γ_c^+ and Γ_c^- [95].

Static equilibrium of the system is governed by

$$\boldsymbol{\nabla} \cdot \boldsymbol{\sigma} + \rho_s \mathbf{b} = \mathbf{0} \tag{2.1}$$

in which $\boldsymbol{\sigma}$ is the Cauchy stress tensor, ρ_s is the mass density of the solid and $\mathbf{b}$ is the vector of body force per unit mass density of the solid. Conservation of the angular momentum requires the symmetry of the Cauchy stress tensor, i.e., $\boldsymbol{\sigma} = \boldsymbol{\sigma}^\top$.

Assuming linear elasticity, small deformations, and that the domain is initially subjected to an *in situ* stress field, $\boldsymbol{\sigma}_0$, the constitutive equation of the solid (rock mass) is taken to be

$$\boldsymbol{\sigma} - \boldsymbol{\sigma}_0 = \mathbb{C} : \boldsymbol{\varepsilon} \tag{2.2}$$

in which $\mathbb{C}$ is the fourth order elasticity tensor, and $\boldsymbol{\varepsilon}$ is the linear strain tensor. The linear

part of the strain tensor is defined by

$$\boldsymbol{\varepsilon} = \frac{1}{2}\left(\boldsymbol{\nabla}\mathbf{u} + \boldsymbol{\nabla}\mathbf{u}^{\top}\right) \tag{2.3}$$

with $\mathbf{u}$ being the solid displacement field.

A bilinear cohesive model similar to the one presented in [49] is used in this study with the traction-separation law defined as

$$t^{coh}(w) = \begin{cases} f_u \dfrac{w}{w_w} & \text{if } w \leq w_w \\ f_u \dfrac{w_c - w}{w_c - w_w} & \text{if } w_w < w \leq w_c \\ 0 & \text{if } w_c < w \end{cases} \tag{2.4}$$

where t^{coh} is the magnitude of the cohesive traction, f_u is the tensile strength of the solid, w is the fracture aperture, w_c is the critical aperture, and w_w is the weakening aperture, which defines the beginning of the weakening branch of the traction-separation law.

The assumption of an impermeable solid suggests that the interaction between the solid and fluid occurs exclusively along the fracture boundary; therefore, the fracture represents the fluid domain, Ω_f. The fluid domain and its Neumann and Dirichlet boundaries, Γ_q and Γ_p, are shown in Figure 4.1.

The one-dimensional flow of an incompressible viscous fluid within the fractures of an

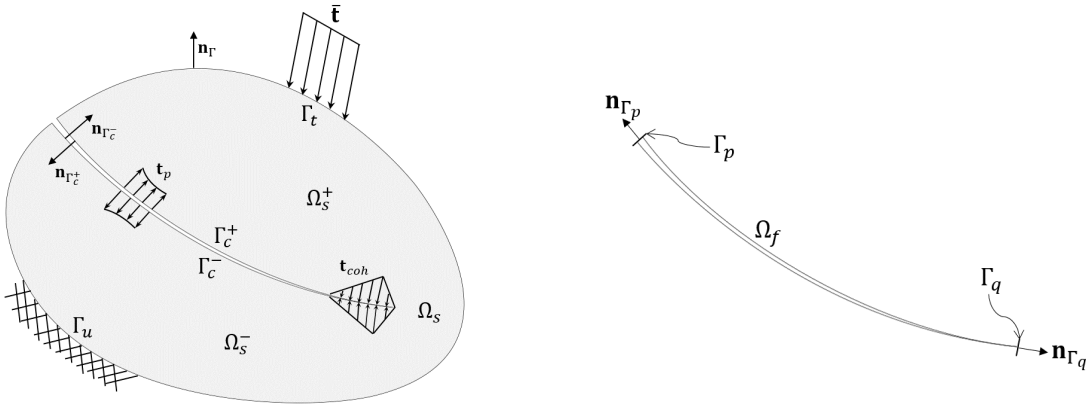

Figure 2.1: Domains of the problem: solid domain (left) and fluid domain (right)

impermeable solid is governed by the conservation of the fluid mass:

$$\frac{\partial w}{\partial t} + \frac{\partial}{\partial s} q = f \tag{2.5}$$

in which w is the fracture aperture, q is the fluid flux, f is the sink/source term, and s denotes the local fracture coordinate measured from its inlet boundary. The assumption of an impermeable solid also requires that the amount of fluid leaking off to the solid from the fracture surfaces be negligible. Therefore, no leak-off term is considered in (3.5). The fluid flux is given by the Cubic law as

$$q = -k(w)\frac{\partial}{\partial s} p \qquad \text{with} \quad k(w) = \frac{w^3}{12\mu}, \forall w > w_c, \text{ else } k = k_c \tag{2.6}$$

where μ is the dynamic viscosity of the fluid. Zhang et al. [154] suggested application of a minimum hydraulic permeability to the fluid model in the regions of closure along the

fracture. In this chapter, we employ a similar minimum permeability, k_c, in the cohesive zone of the fracture where the aperture smoothly vanishes. Since the cohesive zone is representative of the crack tip plasticity/damage in which the induced permeability would be non-zero, this approximation seems reasonable.

The solid domain is subjected to a prescribed traction, $\bar{\mathbf{t}}$, on its Neumann boundary and a prescribed displacement, $\bar{\mathbf{u}}$, on its Dirichlet boundary. Assuming that fluid pressure and cohesive tractions are the only tractions applied to the solid domain along its fracture boundary, the set of boundary conditions of the solid domain are

$$\begin{aligned} \mathbf{u} &= \bar{\mathbf{u}} \quad \text{on } \Gamma_u \\ \boldsymbol{\sigma} \cdot \mathbf{n}_{\Gamma_t} &= \bar{\mathbf{t}} \quad \text{on } \Gamma_t \\ \boldsymbol{\sigma} \cdot \mathbf{n}_{\Gamma_c^+} &= -p\mathbf{I} \cdot \mathbf{n}_{\Gamma_c^+} + t^{coh}\mathbf{I} \cdot \mathbf{n}_{\Gamma_c^+} \quad \text{on } \Gamma_c^+ \\ \boldsymbol{\sigma} \cdot \mathbf{n}_{\Gamma_c^-} &= -p\mathbf{I} \cdot \mathbf{n}_{\Gamma_c^-} + t^{coh}\mathbf{I} \cdot \mathbf{n}_{\Gamma_c^-} \quad \text{on } \Gamma_c^- \end{aligned} \tag{2.7}$$

in which $\mathbf{I}$ is the second order identity tensor, $\mathbf{n}_{\Gamma_t}$ is the outward-facing unit normal vector on the traction boundary, and $\mathbf{n}_{\Gamma_c^+}$ and $\mathbf{n}_{\Gamma_c^-}$ are the outward-facing unit normal vectors on the positive and negative faces of the fracture boundary respectively. The Dirichlet boundary of the fluid domain, Γ_p, is subjected to the prescribed pressure, $\bar{p}$, and the prescribed flux, $\bar{q}$, is applied on the flux boundary, Γ_q. The boundary conditions of the fluid domain are, therefore, defined as

$$\begin{aligned} p &= \bar{p} \quad \text{on } \Gamma_p \\ -k\left(w\right)\frac{\partial}{\partial s}p \cdot \mathbf{n}_{\Gamma_q} &= \bar{q} \quad \text{on } \Gamma_q \end{aligned} \tag{2.8}$$

where $\mathbf{n}_{\Gamma_q} = 1$ at the fracture tip and $\mathbf{n}_{\Gamma_q} = -1$ at the wellbore (inlet) boundary.

Neglecting the body force term in (3.1) and the sink/source term in (3.5), the weak forms of the governing equations are derived by multiplying (3.1) and (3.5) by the test functions, $\delta\mathbf{u} \in U_0$ and $\delta p \in P_0$, respectively, and integrating over the corresponding domains. Hence, the coupled problem is to find $\mathbf{u} \in U$ and $p \in P$ such that

$$\int_{\Omega_s} \boldsymbol{\nabla}\delta\mathbf{u} \colon \mathbb{C} \colon \boldsymbol{\varepsilon} d\Omega - \int_{\Gamma_t} \delta\mathbf{u} \cdot \bar{\mathbf{t}} d\Gamma + \int_{\Gamma_c} [\![\delta\mathbf{u}]\!] \cdot t^{coh}\mathbf{I} \cdot \mathbf{n}_{\Gamma_c} d\Gamma - \int_{\Gamma_c} [\![\delta\mathbf{u}]\!] \cdot p\mathbf{I} \cdot \mathbf{n}_{\Gamma_c} d\Gamma = \mathbf{0} \tag{2.9}$$

and

$$\int_{\Omega_f} \delta p \frac{\partial w}{\partial t} d\Omega + \int_{\Omega_f} \frac{\partial}{\partial s}\delta p k(w) \frac{\partial}{\partial s} p d\Omega + \int_{\Gamma_q} \delta p \bar{q} d\Omega = 0 \tag{2.10}$$

in which $\mathbf{n}_{\Gamma_c} = \mathbf{n}_{\Gamma_c^-} = -\mathbf{n}_{\Gamma_c^+}$, and $[\![\delta\mathbf{u}]\!] = \left(\delta\mathbf{u}\,|_{\Gamma_c^+} - \delta\mathbf{u}\,|_{\Gamma_c^-}\right)$ denotes the jump in the displacement test function on the fracture boundary. The sets of admissible trial and test functions, U and U_0, for the displacement field are defined as

$$\begin{aligned} U &= \left\{\mathbf{u} \,|\, \mathbf{u} \in H^1 \times H^1,\ \mathbf{u} = \bar{\mathbf{u}} \text{ on } \Gamma_u,\ \mathbf{u} \text{ is discontinuous on } \Gamma_c\right\} \\ U_0 &= \left\{\delta\mathbf{u} \,|\, \delta\mathbf{u} \in H^1 \times H^1,\ \delta\mathbf{u} = 0 \text{ on } \Gamma_u,\ \delta\mathbf{u} \text{ is discontinuous on } \Gamma_c\right\} \end{aligned} \tag{2.11}$$

where H^1 is the space of functions whose derivatives are square integrable. Similarly, for

the pressure field, the sets of admissible trial and test functions, P and P_0, are defined as

$$\begin{aligned} P &= \left\{ p \,|\, p \in H^1,\ p = \bar{p} \text{ on } \Gamma_p \right\} \\ P_0 &= \left\{ \delta p \,|\, \delta p \in H^1,\ \delta p = 0 \text{ on } \Gamma_p \right\} \end{aligned} \tag{2.12}$$

Note that the domain is initially in equilibrium under the *in situ* stress field, $\boldsymbol{\sigma}_0$, i.e., $\boldsymbol{\nabla} \cdot \boldsymbol{\sigma}_0 = \mathbf{0}$. Hence, the terms containing $\boldsymbol{\sigma}_0$ vanish from the weak form of the solid equation.

2.2.2 Discretization

The solid domain is discretized by means of quadrilateral elements, as depicted in Figure 4.1. The fracture is discretized by linear segments, passing edge to edge through solid elements, such that the fracture tip is always located at the edge of a solid element.

A discontinuous approximation, without tip enrichments, similar to the one proposed in [43] is used to approximate the solid displacement field. The approximated displacement, $\mathbf{u}_h$, at point $\mathbf{x} \in \Omega_s$ and time t is defined as

$$\begin{aligned} \mathbf{u}_h(\mathbf{x}, t) &= \sum_I N_I(\mathbf{x}) d_I^u(t) + \sum_J N_J(\mathbf{x}) \left[H_c(\mathbf{x}) - H_c(\mathbf{x}_J) \right] d_J^a(t) \\ &\equiv \mathbf{N}^u(\mathbf{x}) \mathbf{d}^u(t) + \mathbf{N}^a(\mathbf{x}) \mathbf{d}^a(t) \equiv \mathbf{N}(\mathbf{x}) \mathbf{d}(t) \end{aligned} \tag{2.13}$$

in which I is the set of all nodes of the mesh and J is the set of enriched nodes. The term $N_I(\mathbf{x})$ denotes the standard finite element shape functions. The standard and enriched degrees of freedom are denoted respectively by $d_I^u(t)$ and $d_J^a(t)$. In matrix form, $\mathbf{d}^u(t)$ and

$\mathbf{d}^a(t)$ are the vectors of the standard and enriched degrees of freedom, $\mathbf{N}^u(\mathbf{x})$ is a matrix of standard shape functions of the element, and $\mathbf{N}^a(\mathbf{x})$ is a the matrix of enriched shape functions. The total N-matrix and degrees of freedom vector for the solid are defined as $\mathbf{N}(\mathbf{x}) = \{\mathbf{N}^u(\mathbf{x}) \;\; \mathbf{N}^a(\mathbf{x})\}$ and $\mathbf{d}(t) = \{\mathbf{d}^u(t) \;\; \mathbf{d}^a(t)\}^\top$ respectively.

The generalized Heaviside function, $H_c(\mathbf{x})$, is defined as

$$H_c(\mathbf{x}) = \begin{cases} -\frac{1}{2} & \text{if } \mathbf{x} \in \Omega_s^- \\ \\ \frac{1}{2} & \text{if } \mathbf{x} \in \Omega_s^+ \end{cases} \tag{2.14}$$

in which Ω_s^+ and Ω_s^- respectively represent parts of the domain located on the positive and negative sides of the fracture.

The fluid domain is discretized into linear elements at its intersections with the solid mesh, as shown in Figure 4.3. A finite element approximation is used for the pressure field. The approximated pressure at point $s \in \Omega_f$ and time t is presented by

$$p_h(s,t) = \sum_L \psi_L(s) p_L(t) \equiv \boldsymbol{\psi}(s)\mathbf{p}(t) \tag{2.15}$$

where L is the set of all nodes of the fluid mesh. The finite element approximation functions and the nodal values of fluid pressure are denoted, respectively, by $\psi_L(s)$ and $p_L(t)$. In the matrix form, the matrix of approximation functions and the vector of nodal pressures are represented by $\boldsymbol{\psi}(s)$ and $\mathbf{p}(t)$ respectively. Similar approximations are used for time derivatives of the displacement and pressure fields.

Referring to (3.18) and (3.23), the spatial derivatives of the displacement and pressure

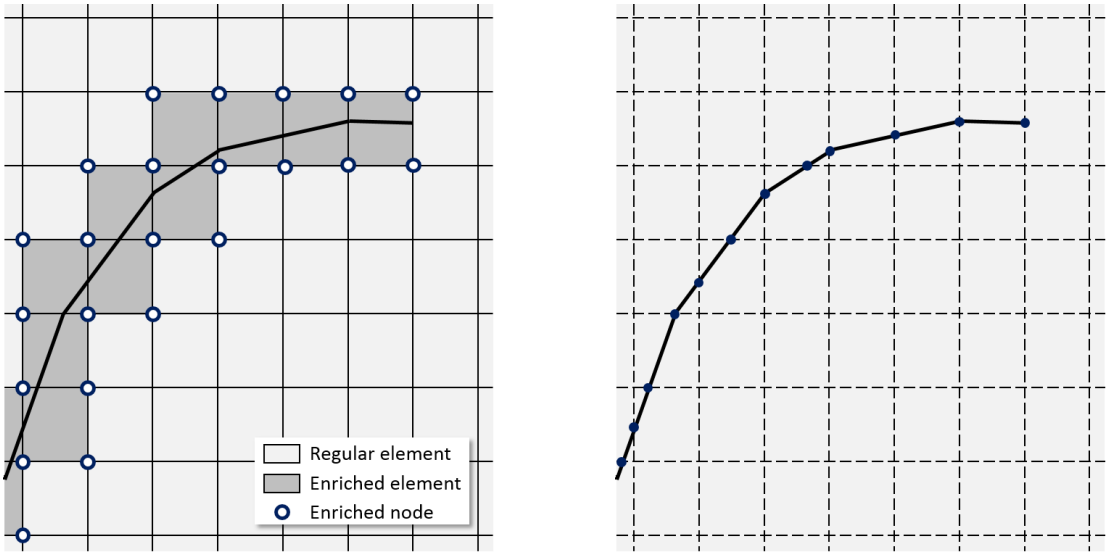

Figure 2.2: Discretization of solid (left) and fluid (right) domains

fields are approximated by

$$\begin{aligned}\boldsymbol{\varepsilon}_h(\mathbf{x},t) &= \sum_I \boldsymbol{\nabla}^s N_I(\mathbf{x}) d_I^u(t) + \sum_J \boldsymbol{\nabla}^s N_J(\mathbf{x}) \left[H_c(\mathbf{x}) - H_c(\mathbf{x}_J)\right] d_J^a(t) \\ &\equiv \mathbf{B}^u(\mathbf{x})\mathbf{d}^u(t) + \mathbf{B}^a(\mathbf{x})\mathbf{d}^a(t) \equiv \mathbf{B}(\mathbf{x})\mathbf{d}(t)\end{aligned} \tag{2.16}$$

and

$$\frac{\partial}{\partial s} p_h(s,t) = \sum_L \boldsymbol{\nabla}\psi_L(s) p_L(t) \equiv \boldsymbol{\nabla}\boldsymbol{\psi}(s)\mathbf{p}(t) \tag{2.17}$$

in which $\boldsymbol{\nabla}^s$ denotes the symmetric gradient operator. $\mathbf{B}^u(\mathbf{x})$, $\mathbf{B}^a(\mathbf{x})$, and $\boldsymbol{\nabla}\boldsymbol{\psi}(s)$ contain the space derivatives of $\mathbf{N}^u(\mathbf{x})$, $\mathbf{N}^a(\mathbf{x})$, and $\boldsymbol{\psi}(s)$ and $\mathbf{B}(\mathbf{x}) = \{\mathbf{B}^u(\mathbf{x}) \;\; \mathbf{B}^a(\mathbf{x})\}$.

Similarly, the jump in the displacement and strain fields across the fracture boundary

are approximated as

$$[\![\mathbf{u}_h]\!] = \mathbf{u}_h\,|_{\Gamma_c^+} - \mathbf{u}_h\,|_{\Gamma_c^-} = \left(\mathbf{N}\,|_{\Gamma_c^+} - \mathbf{N}\,|_{\Gamma_c^-}\right)\mathbf{d} = [\![\mathbf{N}]\!]\mathbf{d} \tag{2.18}$$

and

$$[\![\boldsymbol{\varepsilon}_h]\!] = \left(\mathbf{B}\,|_{\Gamma_c^+} - \mathbf{B}\,|_{\Gamma_c^-}\right)\mathbf{d} = [\![\mathbf{B}]\!]\mathbf{d} \tag{2.19}$$

Using approximations of similar form to (3.18) and (3.23) for the test functions, $\delta\mathbf{u}$ and δp, the semi-discrete form of the coupled system is written so

$$\begin{bmatrix} \mathbf{R}_u \\ \\ \mathbf{R}_p \end{bmatrix} = \begin{bmatrix} \mathbf{K}_{uu}\mathbf{d} - \mathbf{K}_{up}\mathbf{p} + \mathbf{F}_{coh} - \mathbf{F}_{\Gamma_t} \\ \\ \mathbf{K}_{up}^{\top}\dot{\mathbf{d}} + \mathbf{F}_q - \mathbf{F}_{\Gamma_q} \end{bmatrix} = \mathbf{0} \tag{2.20}$$

in which

$$\mathbf{K}_{uu} = \int_{\Omega_s} \mathbf{B}^{\top}\mathbf{C}\mathbf{B}d\Omega \tag{2.21a}$$

$$\mathbf{K}_{up} = \int_{\Gamma_c} [\![\mathbf{N}]\!]^{\top}\mathbf{n}_{\Gamma_c}\boldsymbol{\psi}d\Gamma \tag{2.21b}$$

$$\mathbf{F}_{coh} = \int_{\Gamma_c} [\![\mathbf{N}]\!]^{\top} t^{coh}\left(w\right)\mathbf{n}_{\Gamma_c}d\Gamma \tag{2.21c}$$

$$\mathbf{F}_q = \int_{\Omega_f} \boldsymbol{\nabla}\boldsymbol{\psi}^{\top} k\left(w\right)\frac{\partial}{\partial s}pd\Omega \tag{2.21d}$$

$$\mathbf{F}_{\Gamma_q} = \int_{\Gamma_q} \boldsymbol{\psi}^{\top}\bar{q}d\Gamma \tag{2.21e}$$

$$\mathbf{F}_{\Gamma_t} = \int_{\Gamma_t} \mathbf{N}^{\top}\bar{\mathbf{t}}d\Gamma \tag{2.21f}$$

The fourth order elasticity tensor, $\mathbb{C}$, is represented in the matrix form by $\mathbf{C}$. The vector $\dot{\mathbf{d}}$ denotes the time derivative of the solid degrees of freedom vector, $\mathbf{d}$, and the fracture aperture, w, is defined as

$$w = \mathbf{n}_{\Gamma_c}^{\top} [\![\mathbf{N}]\!] \mathbf{d} \tag{2.22}$$

The time domain is discretized using unevenly distributed time increments, Δt_n, such that $t_n = t_{n-1} + \Delta t_n$, where the subscript n indicates the nth discrete time step. The magnitude of the time increment, Δt_n, is controlled by the stability and convergence requirements of the numerical algorithm at each time step. For the purpose of simplicity, a Backward Euler scheme is used to calculate the time derivative of the displacement field. If the vector of nodal displacements at time $t = t_n$ is represented by $\mathbf{d}^n$, the vector of nodal velocities at the same time step, $\dot{\mathbf{d}}^n$, is approximated by a Backward Euler scheme as

$$\dot{\mathbf{d}}^n \equiv \dot{\mathbf{d}}(t = t_n) = \frac{1}{\Delta t_n}(\mathbf{d}^n - \mathbf{d}^{n-1}) \tag{2.23}$$

Substituting (3.27) into (3.25), the discrete form of the hydro-mechanically coupled system at time $t = t_n$ is written as

$$\begin{bmatrix} \mathbf{R}_u^n \\ \mathbf{R}_p^n \end{bmatrix} = \begin{bmatrix} \mathbf{K}_{uu}^n \mathbf{d}^n - \mathbf{K}_{up}^n \mathbf{p}^n + \mathbf{F}_{coh}^n - \mathbf{F}_{\Gamma_t}^n \\ \frac{1}{\Delta t_n} \mathbf{K}_{up}^{n\top} (\mathbf{d}^n - \mathbf{d}^{n-1}) + \mathbf{F}_q^n - \mathbf{F}_{\Gamma_q}^n \end{bmatrix} = \mathbf{0} \tag{2.24}$$

2.3 Solution strategies

In this section, we use three different solution strategies to solve the hydro-mechanically coupled system of equations (3.28). First, a fully coupled solution strategy based on the Newton-Raphson method is discussed and, subsequently, two sequential coupling strategies are presented. The sequential strategies are developed based on an analogy with the available splitting techniques used for analysis of fluid flow in deformable porous media. In both of the sequential coupling strategies, the solid equation is solved first, at each iteration, given an initial prediction of fluid pressure from the solution of the previous iteration.

2.3.1 Fully coupled solution

To develop a fully coupled strategy for (3.28), we use the Newton-Raphson iterative method to linearize the nonlinear system of equations. The Jacobian of the coupled system for the ith iteration at time $t = t_n$ is defined as

$$\mathbf{J}_i^n = \begin{bmatrix} \dfrac{\partial \mathbf{R}_u}{\partial \mathbf{d}} & \dfrac{\partial \mathbf{R}_u}{\partial \mathbf{p}} \\ \dfrac{\partial \mathbf{R}_p}{\partial \mathbf{d}} & \dfrac{\partial \mathbf{R}_p}{\partial \mathbf{p}} \end{bmatrix}_i^n = \begin{bmatrix} \mathbf{K}_{uu} + \mathbf{K}_{coh} & -\mathbf{K}_{up} \\ \frac{1}{\Delta t}\mathbf{K}_{up}^{\top} + \mathbf{K}_{pu} & \mathbf{K}_{pp} \end{bmatrix}_i^n \tag{2.25}$$

in which

$$\mathbf{K}_{coh}^{n} = \frac{\partial \mathbf{F}_{coh}^{n}}{\partial \mathbf{d}^{n}} = \int_{\Gamma_c} [\![\mathbf{N}]\!]^{\top} \mathbf{n}_{\Gamma_c} \frac{\partial t^{coh}}{\partial w^{n}} \frac{\partial w^{n}}{\partial \mathbf{d}^{n}} d\Gamma = \int_{\Gamma_c} [\![\mathbf{N}]\!]^{\top} \mathbf{n}_{\Gamma_c} \frac{\partial t^{coh}}{\partial w^{n}} \mathbf{n}_{\Gamma_c}^{\top} [\![N]\!] d\Gamma \tag{2.26a}$$

$$\mathbf{K}_{pu}^{n} = \frac{\partial \mathbf{F}_{q}^{n}}{\partial \mathbf{d}^{n}} = \int_{\Omega_f} \boldsymbol{\nabla} \boldsymbol{\psi}^{\top} \frac{\partial}{\partial s} p^{n} \frac{\partial k}{\partial w^{n}} \frac{\partial w^{n}}{\partial \mathbf{d}^{n}} d\Omega = \int_{\Omega_f} \boldsymbol{\nabla} \boldsymbol{\psi}^{\top} \frac{\partial}{\partial s} p^{n} \frac{\partial k}{\partial w^{n}} \mathbf{n}_{\Gamma_c}^{\top} [\![\mathbf{N}]\!] d\Omega \tag{2.26b}$$

$$\mathbf{K}_{pp}^{n} = \frac{\partial \mathbf{F}_{q}^{n}}{\partial \mathbf{p}^{n}} = \int_{\Omega_f} \boldsymbol{\nabla} \boldsymbol{\psi}^{\top} k\left(w^{n}\right) \boldsymbol{\nabla} \boldsymbol{\psi} d\Omega \tag{2.26c}$$

and $\dfrac{\partial w^{n}}{\partial \mathbf{d}^{n}}$ is obtained from (2.22). Therefore, the increments of the primary variables, $\Delta\mathbf{d}$ and $\Delta\mathbf{p}$, at the ith iteration of time $t = t_n$, are determined from the linear system

$$\begin{bmatrix} \mathbf{K}_{uu} + \mathbf{K}_{coh} & -\mathbf{K}_{up} \\ \frac{1}{\Delta t}\mathbf{K}_{up}^{\top} + \mathbf{K}_{pu} & \mathbf{K}_{pp} \end{bmatrix}_{i}^{n} \begin{bmatrix} \Delta\mathbf{d} \\ \Delta\mathbf{p} \end{bmatrix}_{i}^{n} + \begin{bmatrix} \mathbf{R}_{u} \\ \mathbf{R}_{p} \end{bmatrix}_{i}^{n} = \mathbf{0} \tag{2.27}$$

and the primary variables are updated by

$$\begin{bmatrix} \mathbf{d} \\ \mathbf{p} \end{bmatrix}_{i+1}^{n} = \begin{bmatrix} \mathbf{d} \\ \mathbf{p} \end{bmatrix}_{i}^{n} + \begin{bmatrix} \Delta\mathbf{d} \\ \Delta\mathbf{p} \end{bmatrix}_{i}^{n} \tag{2.28}$$

Table 2.1 summarizes the algorithm for performing the fully coupled solution for the hydro-mechanically coupled system.

Table 2.1: Fully coupled solution algorithm

1.	Set $i = 0$, $\mathbf{d} = \mathbf{d}_i^n$, and $\mathbf{p} = \mathbf{p}_i^n$
2.	Compute $\mathbf{R}_i^n = \left\{\mathbf{R}_u^n \quad \mathbf{R}_p^n\right\}_i^\top$ from (3.28)
3.	If $\frac{\|\|\mathbf{R}_i^n\|\|_{L2}}{\|\|\mathbf{R}_0^n\|\|_{L2}} < \tau^*$, go to step 9
4.	Construct $\mathbf{J}_i^n$ from (3.31)
5.	Calculate $\Delta\mathbf{d}_i^n$ and $\Delta\mathbf{p}_i^n$ from (3.30)
6.	Update $\mathbf{d}_{i+1}^n$ and $\mathbf{p}_{i+1}^n$ from (2.28)
7.	$i \longleftarrow i + 1$
8.	Go to step 2
9.	End

* τ is the admissible error of the Newton-Raphson iteration

2.3.2 Sequential solutions

In the analysis of fluid flow in porous media, the hydro-mechanically coupled system can be split into two equations (sub-systems), which are then solved sequentially. In this section, we use the analogy with porous media to split and sequentially solve the coupled system of equations (3.28) for hydraulic fracture propagation in an impermeable medium. The focus of this chapter is on the sequential schemes for the simulation of hydraulic fractures that solve the mechanical subproblem first (i.e., drained and undrained splits).

Drained HF split

The term *drained split*, in the analysis of fluid flow in porous media, refers to the iterative process in which, at each iteration, solid deformations are determined through solving

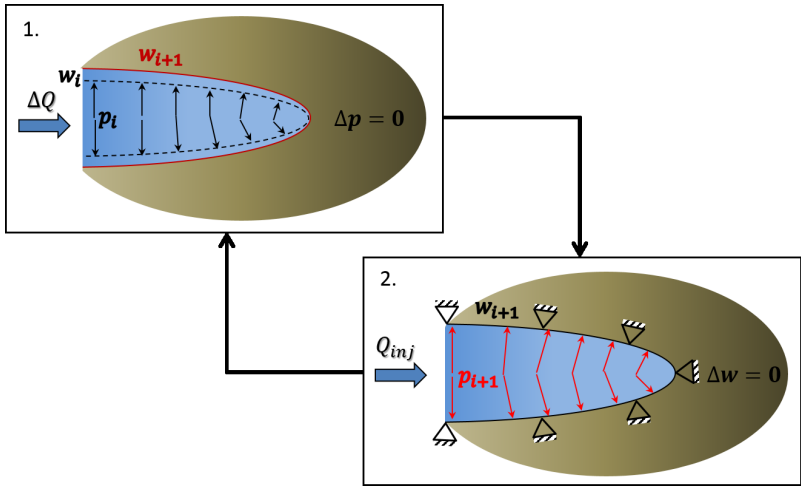

Figure 2.3: Schematic of the drained HF split for a hydraulic fracture in an impermeable medium. Quantities shown in red are solved for in each step and quantities shown in black are frozen during that step.

the mechanical problem with the assumption that fluid pressure within the solid matrix remains unchanged. Once solid displacements are updated, the fluid equation is solved given the updated solid displacements. The assumption that solid deforms under a fixed fluid pressure requires that fluid be flowed into or out of the solid matrix as the matrix deforms. The term *drained* stems from this physical interpretation.

In this section, we summarize the *drained HF split*. A schematic of the drained HF split iterative scheme for a pressure driven fracture in an impermeable medium is shown in Figure 2.3.

At each iteration of every time step, first the solid displacements are estimated given that the fluid nodal pressure are $\mathbf{p}_i^n$. So the increment in the solid displacement at iteration i is

$$\Delta \mathbf{d}_i^n = -\left(\mathbf{K}_{uu}^n + \mathbf{K}_{coh_i}^n\right)^{-1} \mathbf{R}_{u_i}^n \tag{2.29}$$

and the vector of the solid degrees of freedom is updated as

$$\mathbf{d}_{i+1}^n = \mathbf{d}_i^n + \Delta \mathbf{d}_i^n \tag{2.30}$$

Next, the nodal values of fluid pressure are directly updated using the fluid equation given displacements $\mathbf{d}_{i+1}^n$:

$$\mathbf{K}_{pp}^n \mathbf{p}_{i+1}^n = \mathbf{F}_{\Gamma_q}^n - \frac{1}{\Delta t_n} \mathbf{K}_{up}^{n^\top} \left(\mathbf{d}_{i+1}^n - \mathbf{d}^{n-1}\right) \tag{2.31}$$

The drained HF split presented above is identical to the $P \rightarrow W$ algorithm for the simulation of hydraulic fractures in impermeable media. The algorithm for performing the drained HF split is summarized in Table 2.2.

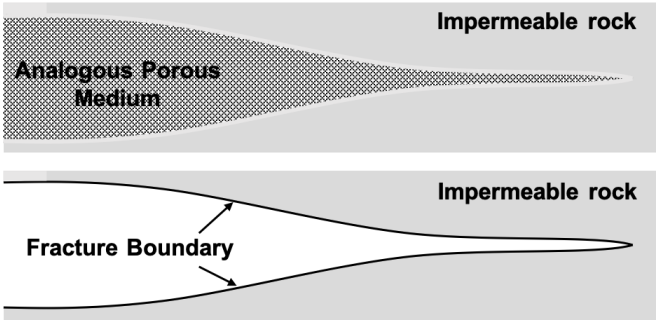

Figure 2.4: Substitution of the fracture with its analogous porous medium

Table 2.2: Drained HF split algorithm

1.	Set $i = 0$ and initialize $\mathbf{d} = \mathbf{d}_i^n$ and $\mathbf{p} = \mathbf{p}_i^n$
2.	Construct $\mathbf{K}_{uu}^n$ from (3.26a) and $\mathbf{K}_{up}^n$ from (3.26b)
3.	Construct $\mathbf{K}_{coh_i}^n$ from (3.32a) and $\mathbf{K}_{pp_i}^n$ from (3.32c)
4.	Compute $\mathbf{R}_{u_i}^n$ from (3.28)
5.	If $\frac{\left\|\left\|\mathbf{R}_{u_i}^n\right\|\right\|_{L2}}{\left\|\left\|\mathbf{R}_{u_0}^n\right\|\right\|_{L2}} < \tau^*$, go to step 11
6.	Calculate $\Delta\mathbf{d}_i^n$ from (2.29)
7.	Update $\mathbf{d}_{i+1}^n = \mathbf{d}_i^n + \Delta\mathbf{d}_i^n$
8.	Calculate $\mathbf{p}_{i+1}^n$ from (2.31) using $\mathbf{d}_{i+1}^n$ from step 7
9.	$i \longleftarrow i + 1$
10.	Go to step 3
11.	End

* τ is the admissible error of the Newton-Raphson iteration

Undrained HF split

In this subsection the *undrained HF split* is introduced and is developed based upon an analogy to analogous splits used in poromechanics. As will be demonstrated, the drained HF split previously described lacks robustness and often fails to converge. It is therefore desirable to establish a basis for an improved set of nodal pressures to be used when solving the solid equations.

In the analysis of fluid flow in a deformable porous medium, the *undrained split* refers to an iterative coupling scheme in which the mechanical problem is solved first with the assumption that the fluid mass content in the porous matrix remains unchanged as the solid

matrix deforms. In other words, fluid is not allowed to flow in or out of each point in the porous matrix when the mechanics problem is solved–leading to an undrained condition. After solving the solid equation and updating the solid deformations, fluid pressure is updated through solving the fluid equation, given the updated solid deformations.

To develop the undrained HF split which will provide a more robust prediction of the nodal fluid pressures, assume that the fracture is replaced by an Analogous Porous Medium (APM) with a given Biot coefficient, b, and Biot Modulus, M, as illustrated in Figure 2.4.

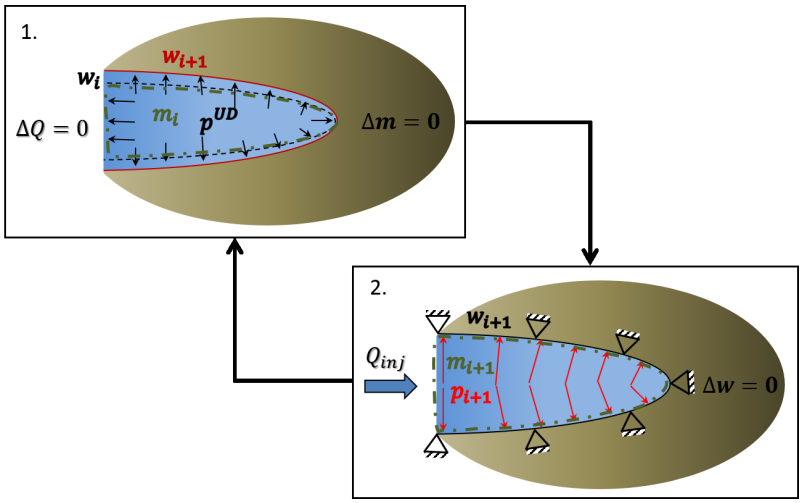

Figure 2.5: Schematic of the undrained HF split for a hydraulic fracture in an impermeable medium. Quantities shown in red are solved for in each step and quantities shown in black are frozen during that step.

Figure 2.5 illustrates the undrained HF iterative scheme for a hydraulic fracture.

Conservation of the fluid mass content in the APM relates the rate of change in the fluid mass content, ξ, at a point along the fracture to the rate of change in the fluid pressure

and the rate of change in the unit volume of the APM via

$$\dot{\xi} = b\dot{\varepsilon}_v^{(APM)} + \frac{1}{M}\dot{p} \quad (0 \leq b \leq 1) \tag{2.32}$$

in which $\varepsilon_v^{(APM)}$ is the volumetric strain in the APM. Enforcing the undrained condition, $\dot{\xi} = 0$, will lead to a relationship

$$b\dot{\varepsilon}_v^{(APM)} + \frac{1}{M}\dot{p} = 0 \tag{2.33}$$

The weak form of (2.33) is derived by multiplying (2.33) by the test function, $\delta p \in P_0$, and integrating over the fluid domain, Ω_f, as

$$\int_{\Omega_f} \delta p b\dot{\varepsilon}_v^{(APM)} d\Omega + \int_{\Omega_f} \delta p \frac{1}{M}\dot{p} d\Omega = 0 \tag{2.34}$$

To discretize (2.34) in space, the test function, δp, is taken to be of the same form as (3.23). Space discretization of (2.34) also requires an approximation for the volumetric strain in the APM. An intuitive definition for the strain in the APM is:

$$\boldsymbol{\varepsilon}^{(APM)} = \frac{[\![\mathbf{N}]\!]\Delta\mathbf{d}}{[\![\mathbf{N}]\!]\mathbf{d}} \tag{2.35}$$

While this may seem a natural choice, it causes significant numerical difficulties. Specifically, when fracture closure is considered or in the vicinity of the cohesive zone (tip) where fracture aperture is relatively small, (2.35) will result in an ill-conditioned coefficient matrix (due to division by zero or a very small value).

Let the deformation of the APM at each point along the fracture be taken as the crack opening displacement, i.e.,

$$\mathbf{u}^{(APM)} = [\![\mathbf{N}]\!]\mathbf{d} \tag{2.36}$$

So the strain and volumetric strain of the APM are

$$\boldsymbol{\varepsilon}^{(APM)} = [\![\mathbf{B}]\!]\mathbf{d} \tag{2.37}$$

$$\varepsilon_v^{(APM)} = \mathbf{m}\boldsymbol{\varepsilon}^{(APM)} = \mathbf{m}[\![\mathbf{B}]\!]\mathbf{d} \tag{2.38}$$

in which $\mathbf{m} = \{n_1^2 \;\; n_2^2 \;\; n_1 n_2\}$, for a two-dimensional problem, with n_i being the components of the unit normal vector, $\mathbf{n}_{\Gamma_c}$. The assumed definition for the strain of the APM, (2.37), is equivalent to the jump in strain across the fracture, which is always finite and well defined. The volumetric strain, ε_v^{APM}, is a one-dimensional measure of aperture strain in the direction of fracture opening. The component of strain in the tangential direction is neglected in this formulation as the tangential component of aperture does not cause any change in the volume of the APM.

The semi-discrete form of (2.34) after substituting (2.38) into (2.34) is written so

$$b\mathbf{S}_{pu}\dot{\mathbf{d}} + \frac{1}{M}\mathbf{S}_{pp}\dot{\mathbf{p}} = 0 \tag{2.39}$$

where

$$\mathbf{S}_{pu} = \int_{\Omega_f} \boldsymbol{\psi}^\top \mathbf{m}[\![\mathbf{B}]\!] d\Omega \tag{2.40a}$$

$$\mathbf{S}_{pp} = \int_{\Omega_f} \boldsymbol{\psi}^\top \boldsymbol{\psi} d\Omega \tag{2.40b}$$

By means of a differencing scheme, (2.39) is written in discrete form, as

$$b\mathbf{S}_{pu}\left(\mathbf{d}^n - \mathbf{d}^{n-1}\right) + \frac{1}{M}\mathbf{S}_{pp}\left(\mathbf{p}^{(UD)} - \mathbf{p}^{n-1}\right) = 0 \tag{2.41}$$

where $\mathbf{p}^{(UD)}$ is the vector of nodal *undrained* pressures in the APM.

Solving (2.41) for $\mathbf{p}^{(UD)}$ in the ith iteration at time $t = t_n$, the undrained pressures are

$$\mathbf{p}_i^{(UD)} = \mathbf{p}^{n-1} - bM\mathbf{S}_{pp}^{-1}\mathbf{S}_{pu}\left(\mathbf{d}_i^n - \mathbf{d}^{n-1}\right) \tag{2.42}$$

Equation (2.42) introduces a relationship between the pressure applied to the crack surfaces and the crack opening displacements for the purpose of updating the displacements. This equation can also be viewed as a predictor step for the nodal fluid pressures.

Substitution of (2.42) for $\mathbf{p^n}$ into the residual for the solid equation (3.28) yields

$$\mathbf{R}_{u_i}^n = \mathbf{K}_{uu}\mathbf{d}_i^n - \mathbf{K}_{up}^n\left(\mathbf{p}^{n-1} - bM\mathbf{S}_{pp}^{-1}\mathbf{S}_{pu}\left(\mathbf{d}_i^n - \mathbf{d}^{n-1}\right)\right) + \mathbf{F}_{coh_i}^n - \mathbf{F}_{\Gamma_t}^n = \mathbf{0} \tag{2.43}$$

Solution of (2.43) at time $t = t_n$ using a Newton-Raphson method yields a linear system for the i-th iteration increment of the nodal displacements

$$\left(\mathbf{K}_{uu}^{n^{(UD)}} + \mathbf{K}_{coh_i}^n\right)\Delta\mathbf{d}_i^n = -\mathbf{R}_{u_i}^n \tag{2.44}$$

in which $\mathbf{K}_{uu}^{n^{(UD)}} = \mathbf{K}_{uu}^n + bM\mathbf{K}_{up}^n\mathbf{S}_{pp}^{-1}\mathbf{S}_{pu}$ is the undrained stiffness matrix of the imperme-

able solid. The vector, $\mathbf{d}_{i+1}^{n}$, is then updated by (2.30). Once the displacement is updated, fluid pressure is determined by solving the set of fluid equations (2.31) using the updated displacement vector.

Table 2.3 summarizes the algorithm for performing the undrained HF split. The convergence criteria presented in Tables 2.1-2.3 are all based on the $L2$ norm of the residual of the coupled system, $\mathbf{R}_i = \{\mathbf{R}_u \ \mathbf{R}_p\}^\top$. However, since the sequential schemes each result in a linear fluid equation (i.e., $||\mathbf{R}_p||_{L2} = 0$), the convergence criterion in Tables 2 and 3 are given in terms of $\mathbf{R}_u$. It is worth mentioning that matrix, $\mathbf{S}_{pp}$, is formulated in the form of a mass matrix. Therefore, one can use a lumped representation of $\mathbf{S}_{pp}$ to simplify and accelerate computations. It is also noteworthy that the constants b and M may be replaced by a single constant $\alpha = bM$.

The undrained HF split proposed in this chapter can be formulated also as a local approach. The local approach will use the discrete form of the volumetric strain, (2.38), in (2.33) and approximates the time derivative using a backward Euler scheme, $\dot{\varepsilon}_v^n = (\varepsilon_v^n - \varepsilon_v^{n-1})/\Delta t$, to come up with an expression similar to (2.42) for the undrained pressure. The global version of the undrained scheme is made computationally efficient through the lumping of $\mathbf{S}_{pp}$.

2.4 Numerical Examples

In this section we provide numerical examples to demonstrate the capabilities of the undrained HF split in the simulation of hydraulic fractures in impermeable media. First,

Table 2.3: Undrained HF split algorithm

0.	Assign values of b and M
1.	Set $i = 0$ and initialize $\mathbf{d} = \mathbf{d}_i^n$ and $\mathbf{p} = \mathbf{p}_i^n$
2.	Construct $\mathbf{K}_{uu}^n$ and $\mathbf{K}_{up}^n$ from (3.26), $\mathbf{S}_{pu}$ and $\mathbf{S}_{pp}$ from (2.40) and $\mathbf{K}_{uu}^{n^{(UD)}} = \mathbf{K}_{uu}^n + bM\mathbf{K}_{up}^n\mathbf{S}_{pp}^{-1}\mathbf{S}_{pu}$
3.	Construct $\mathbf{K}_{coh_i}^n$ from (3.32a) and $\mathbf{K}_{pp_i}^n$ from (3.32c)
4.	Update $\mathbf{p}_i^{(UD)}$ from (2.42)
5.	Compute $\mathbf{R}_{u_i}^n$ from (2.43)
6.	If $\frac{\left\|\left\|\mathbf{R}_{u_i}^n\right\|\right\|_{L2}}{\left\|\left\|\mathbf{R}_{u_0}^n\right\|\right\|_{L2}} < \tau^*$, go to step 12
7.	Calculate $\Delta\mathbf{d}_i^n$ from (2.44)
8.	Update $\mathbf{d}_{i+1}^n = \mathbf{d}_i^n + \Delta\mathbf{d}_i^n$
9.	Calculate $\mathbf{p}_{i+1}^n$ from (2.31) using $\mathbf{d}_{i+1}^n$ from step 8
10.	$i \longleftarrow i + 1$
11.	Go to step 3
12.	End

* τ is the admissible error of the Newton-Raphson iteration

we simulate the self-similar propagation of a plane strain hydraulic fracture. The results of the undrained HF split for this problem are compared with the results of the KGD hydraulic fracture model. Subsequently, the application of both drained and undrained HF splits for simulating the propagation of hydraulic fractures from a pressurized wellbore under anisotropic *in situ* stress conditions is examined. The two algorithms are compared in terms of stability. Finally, the convergence of the undrained HF split is investigated through a comparison with the fully coupled model for the second numerical example.

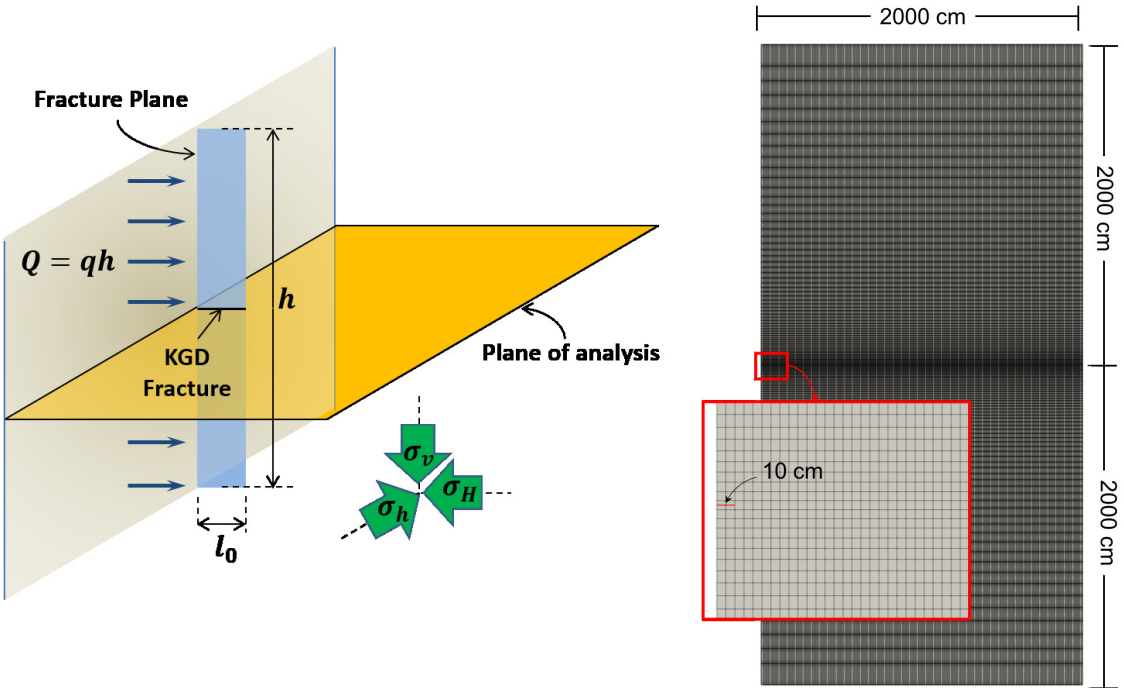

Figure 2.6: Propagation of a planar hydraulic fracture: schematic of the problem (left) and numerical mesh (right)

2.4.1 Propagation of a planar hydraulic fracture

The propagation of a hydraulic fracture initiated at the edge of a $40m \times 20m$ domain, as illustrated in Figure 2.6, is simulated using the undrained HF split algorithm. In a symmetric domain, the fracture tends to propagate planarly under plane strain conditions from a point injection at its inlet on the domain edge (see Figure 2.6). The domain is assumed to remain elastic with the fracture process zone modeled using a cohesive law. The solid has an elasticity modulus of $E = 16\ GPa$ and Poisson's ratio of $\nu = 0.2$. The fluid has a dynamic viscosity of $\mu = 10^{-3} Pa \cdot s$, and the fluid flow is assumed to be laminar. The Biot constants of the APM are chosen such that $bM = 0.05E$ in this example. We

choose a convergence tolerance of $\tau = 10^{-12}$ for the normalized $L2$ norm of the residual of the coupled system. We also assume that the *in situ* stress field and the initial fluid pressure inside the fracture are zero in this example.

The solid domain is discretized by means of bilinear quadrilateral elements using the structured mesh shown in Figure 2.6. The mesh size is constant in the x-direction and increases exponentially in the y-direction from the fracture plane. The effective size of the mesh is $h_e = 0.050\ m$, along the fracture, and $h_e = 0.26\ m$ at the top and bottom edges of the domain. The fracture starts to propagate from its initial length, $l_0 = 0.1m$, as a result of an injection at the rate of $Q_{inj} = 10^{-4}\frac{m^3}{s \cdot m}$ at the left edge of the domain. The solid domain is fixed in the x-direction on its left and right edges and in the y-direction on its top and bottom edges. A no-flow boundary condition is assumed at the tip boundary of the fluid domain, i.e., $q_{tip} = 0$.

The conservation equation (3.5) requires at least one essential boundary condition on the fluid pressure. Since the fluid flux at an essential boundary is a part of the solution of the fluid model, it is not directly controllable. So we introduce an additional global continuity constraint and iterate on the prescribed inlet pressure $\bar{p} = p_{inj}$ until the volume of the fluid in the fracture is equal to the total volume of fluid injected.

The global continuity constraint is given by

$$Q_{inj} = \int_{\Omega_f} \dot{w} d\Omega \tag{2.45}$$

The satisfaction of the global continuity constraint dictates the value of the fluid pressure at the fracture inlet, p_{inj}; therefore, the fluid pressure at the fracture inlet is a part

of the numerical solution. A tolerance of $\eta = 10^{-2}$ is chosen for the relative error in the satisfaction of the global continuity constraint in this example.

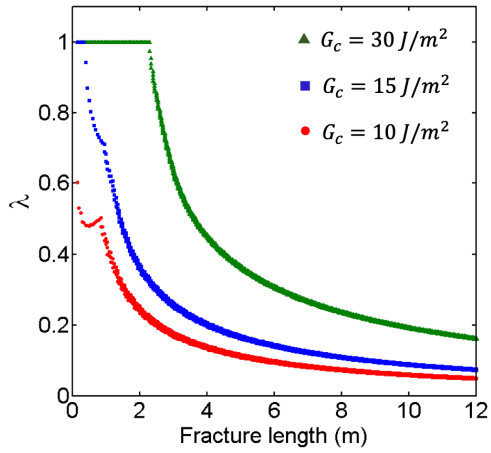

Figure 2.7: Illustration of the change in $\lambda = \frac{L_{coh}}{L_f}$ vs fracture length, L_f, for different values of G_c, simulated using the undrained HF split

A solution for the problem of a planar hydraulic fracture that propagates under plane strain condition, presented by Geertsma and De Klerk in [48], is known as the KGD hydraulic fracture model. The KGD solution, however, cannot be directly compared with the results of a cohesive hydraulic fracture model. The solution presented for fracture aperture and fluid pressure in [48] are independent of the fracture energy (or equivalently, fracture toughness), whereas the solution of a cohesive hydraulic fracture model strongly depends on the value of the fracture energy and the length of the cohesive zone. In other words, the KGD solution represents the propagation of a plane strain hydraulic fracture in a viscosity dominated regime, whereas the solution of a cohesive hydraulic fracture gets close to a viscosity dominated regime only when its cohesive zone vanishes (or when the fracture toughness tends to zero). The effect of the fracture energy on the global solution of

a cohesive fracture is significant when the fracture is relatively short and, hence, the ratio of the cohesive zone to the total length of the fracture is not negligible. For sufficiently long fractures, the effect of the damaged region ahead of the fracture tip, represented by the cohesive zone, can be assumed to remain limited to the local solution around the fracture tip. Therefore, the KGD and cohesive models are only comparable when the fracture propagates to such an extent that the cohesive zone is a negligible portion of the total fracture length, or when the fracture energy (fracture toughness) tends to zero. With these limitations in mind, a comparison of the KGD solution with that of the cohesive fracture model is presented as a means of qualitative validation and of studying the behaviour of the nonlinear HF model.

To investigate the effect of fracture energy (fracture toughness) on the solution, let us consider three different values of fracture energy, $G_c = 30\ J/m^2$, $G_c = 15\ J/m^2$, and $G_c = 10\ J/m^2$, respectively corresponding to the values of fracture toughness, $K = 0.71\ MPa\sqrt{m}$, $K = 0.50\ MPa\sqrt{m}$, and $K = 0.41\ MPa\sqrt{m}$ through Irwin's relationship, $G_c = K_{IC}^2(1-\nu^2)/E$, under plane strain conditions. Using the undrained HF split, Figure 2.7 illustrates the trend by which the ratio of the length of the cohesive zone to the actual length of the fracture, $\lambda = \frac{L_{coh}}{L_f}$, decreases as the fracture evolves. The figure shows that for the models with larger fracture energy, the cohesive zone initially covers the whole length of the fracture and, therefore, comparison of the results with the toughness-independent KGD solution is impractical. Even when the fracture propagates to a length of about $12m$, the ratio, λ, is about 0.2 for the model with $G_c = 30\ J/m^2$, and 0.08 for the one with $G_c = 15\ J/m^2$, and the effect of the cohesive zone on the global solution is still not negligible. For the model with $G_c = 10\ J/m^2$, the initial value of λ is 0.6, which

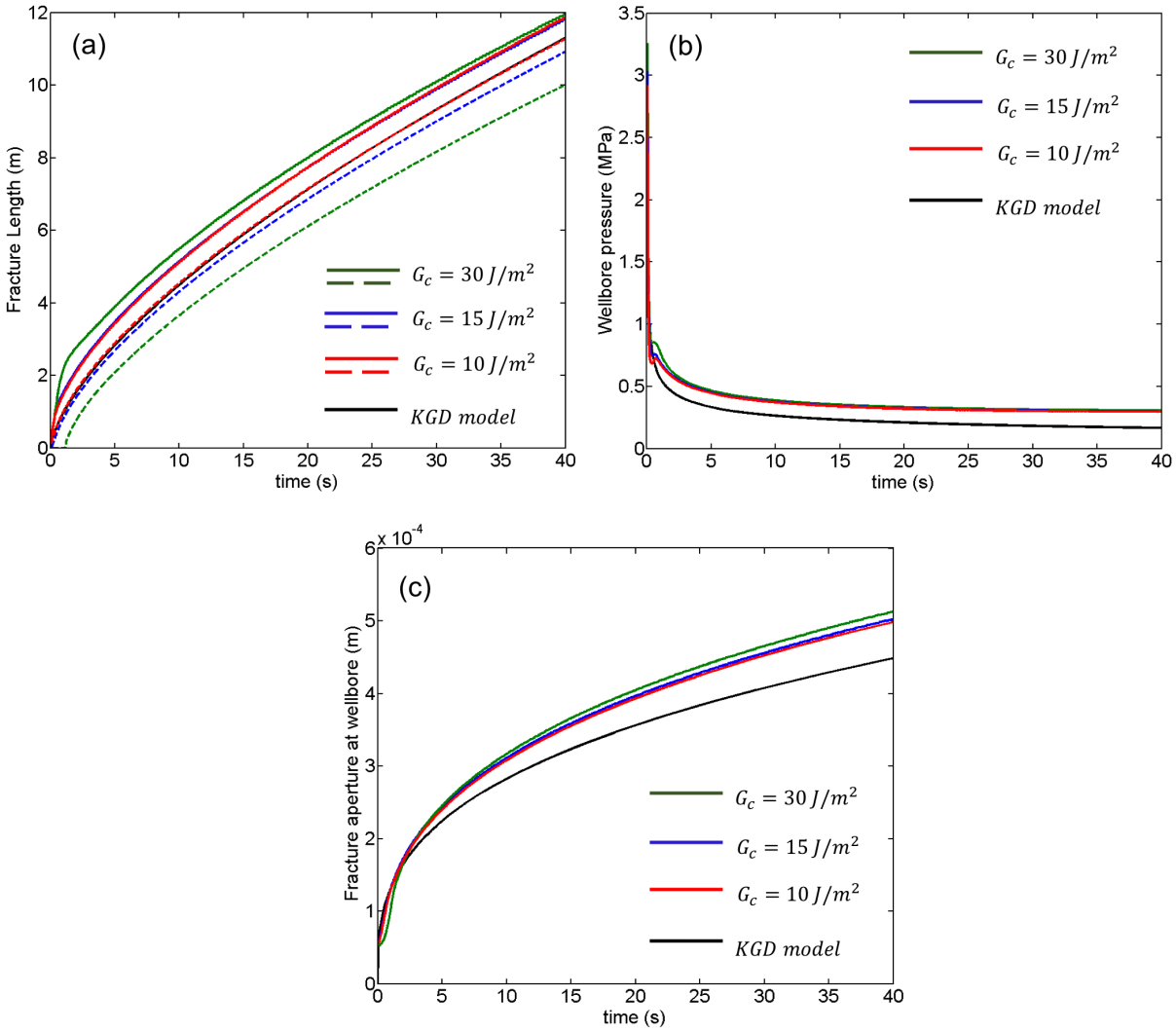

Figure 2.8: Illustrations of time variation of fracture length (a), wellbore pressure (b), and fracture aperture at the wellbore (c) for the new undrained HF split. Solid lines in (a) indicate the location of the mathematical tip and dashed lines indicate the location of the physical tip of the cohesive hydraulic fracture.

means that the cohesive zone does not cover the whole length of the fracture initially. A slight increase of λ is seen for this model between the fracture lengths of about 0.5 m and

1.0 m. This increase can be due to the slightly faster propagation of the mathematical tip in comparison with the physical tip of the fracture, which increases the numerator of the ratio more than its denominator. As the fracture evolves, λ continuously decreases to a value of about 0.05 at the length of 12 m.

It should be noted that the solution of the undrained HF split converges to the same solution as those of the fully coupled model. Therefore, in what follows, we present only the undrained HF split solutions in the graphs. It is also notable that the maximum deviations from the total injected volume after 40 seconds of injection are 0.18%, 0.32%, and 0.25% for the models with $G_c = 30\ J/m^2$, $G_c = 15\ J/m^2$, and $G_c = 10\ J/m^2$, respectively. Therefore, the global continuity constraint is well satisfied for all the three models in this example.

The time-variation of wellbore pressure, fracture aperture at the wellbore, and fracture length for different values of fracture energy are compared with those from the KGD model in Figure 2.8. All curves are smooth, and there is no evidence of spurious oscillations. Figure 2.8a shows the location of both mathematical and physical tips of the fracture. It is evident from the figure that the fracture tip of the KGD model lies between the physical and mathematical tips of the cohesive hydraulic fracture. As the fracture energy decreases, the cohesive zone vanishes and the physical tip of the cohesive model converges to the KGD solution for the location of the fracture tip. The cohesive fracture model yields a slightly higher injection pressure ($\approx 0.15\ MPa$) than the wellbore pressure estimated by the KGD model. The slight discrepancy between the results of a cohesive hydraulic fracture and the KGD model can be explained through the difference between the assumptions that each model makes for material behavior at the fracture tip. Cohesive tractions acting at the

tip region of a cohesive hydraulic fracture stiffen the fracture at the tip. This additional stiffness requires a slightly higher driving pressure at the fracture inlet to propagate the fracture. Higher wellbore pressure results in a slightly larger fracture aperture ($\approx 0.06\ mm$) at the wellbore as illustrated in Figure 2.8c. Similar discrepancies between the results of a cohesive plane strain hydraulic fracture and those of a non-cohesive hydraulic fracture has also been reported in [68]. It is noted that the discrepancies shown here are smaller.

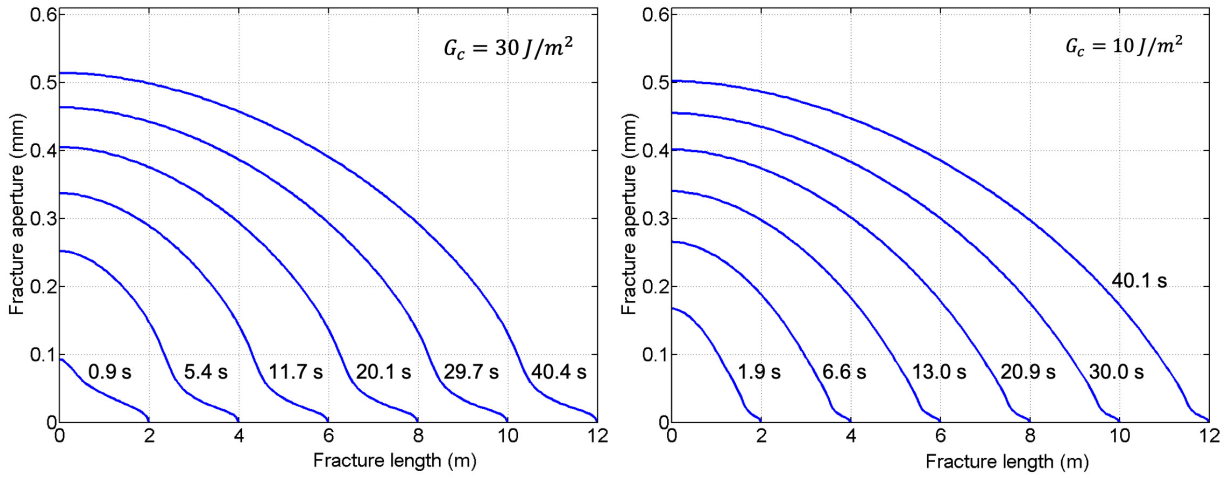

Figure 2.9: Profiles of cohesive HFs with $G_c = 30\ J/m^2$ (left) and $G_c = 10 J/m^2$ (right) at various fracture lengths, simulated using the new undrained HF split

The fracture profiles and distributions of fluid pressure along the fracture are respectively shown in Figures 2.9 and 2.10 for the models with $G_c = 30\ J/m^2$ and $G_c = 10\ J/m^2$. For higher values of fracture energy, fluid pressure maintains a distribution close to a uniform pressure (i.e., low pressure gradient) along the fracture. The pressure gradient increases near the fracture tip and pressure drops to a value close to zero within a small region behind the mathematical tip of the fracture. For the model with low fracture en-

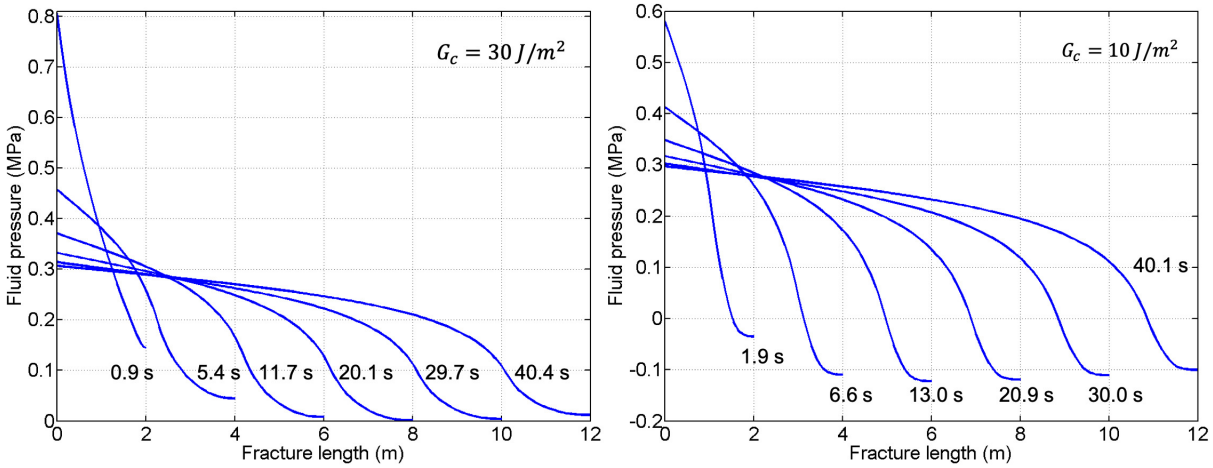

Figure 2.10: Distribution of fluid pressure along the fracture for cohesive HFs with $G_c = 30\ J/m^2$ (left) and $G_c = 10 J/m^2$ (right) at various fracture lengths, simulated using the new undrained HF split

ergy, the pressure distribution deviates from uniform (i.e., higher pressure gradient), and a small negative-pressure region develops in the cohesive zone behind the mathematical tip, as observed in asymptotic solutions of plane-strain HF models. Figure 2.10 also shows that the values of pressure at the tip are finite in both models and no pressure singularity is observed at the fracture tip in the solution of the cohesive hydraulic fracture model.This stems from the finite non-zero permeability used to model fluid flow in the cohesive zone and the no-flux boundary condition at the tip. The length of the region near the fracture tip in which fluid pressure drops steeply, and the value of pressure gradient in this region depend on the length of the cohesive zone of the fracture. Therefore, for the model with a lower fracture energy, the drop in the pressure near the fracture tip is sharper than that of the model with a higher fracture energy, as seen in Figure 2.10. Hence, one can assume that for an ultimate case in which the cohesive zone vanishes (i.e., $G_c \to 0$), pressure drops

with an infinite slope at the fracture tip, and fluid pressure becomes singular. The effect of the cohesive zone can also be seen on fracture profiles in Figure 2.9. For a given fracture length, the model with higher fracture energy generally yields a smaller aperture near the fracture tip and a larger aperture at the wellbore.

2.4.2 Propagation of hydraulic fractures from a wellbore

The propagation of pressurized fractures from a wellbore has been investigated by Mogilevskaya et al. [98]. The study has used a Complex Hypersingular Equation (CHSIE) to simulate a fracture propagating from a circular wellbore in a two-dimensional homogeneous domain. The model has been developed in the Linear Elastic Fracture Mechanics (LEFM) framework and considered two different cases 1) slow pressurization of fractures in which a uniform pressure distribution is assumed within the fractures and 2) fast pressurization of fractures in which tractions due to the fluid pressure are applied only at the fracture inlet. Hence, despite meaningful results in terms of fracture trajectories, the study has not considered real hydro-mechanical coupling in the simulation of pressurized fractures. A more complex model for the problem has been developed by Zhang et al. [154] in which a fully coupled scheme has been employed for the simulation of hydraulically induced fractures propagating from a wellbore. This model is also developed in the LEFM framework and uses lateral and frictional contact models to capture fracture closure and shearing deformations. The model has been applied to multiple fracture problems with various inclination angles.

In this section, the application of the undrained HF split for simulating the propagation

of a hydraulic fracture from a pressurized wellbore is investigated. A hydraulic fracture is assumed to initiate, from a pre-existing flaw, at the wall of a wellbore. The flaw may be due to the existence of micro-fractures in the rock or an intentional perforation for controlling the initiation of hydraulic fractures. The wellbore is drilled in the direction of the intermediate component of the *in situ* stress field, in an elastic and impermeable formation. The diameter of the wellbore is 12.7 cm (5 in). The impermeable rock is assumed to have an elastic modulus of $E = 16GPa$, Poisson's ratio of $\nu = 0.2$, tensile strength of $T = 0.5\ MPa$, and fracture energy of $G_c = 50\ J/m^2$ (or equivalently, a fracture toughness of $K_{IC} = 0.91\ MPa\sqrt{m}$).

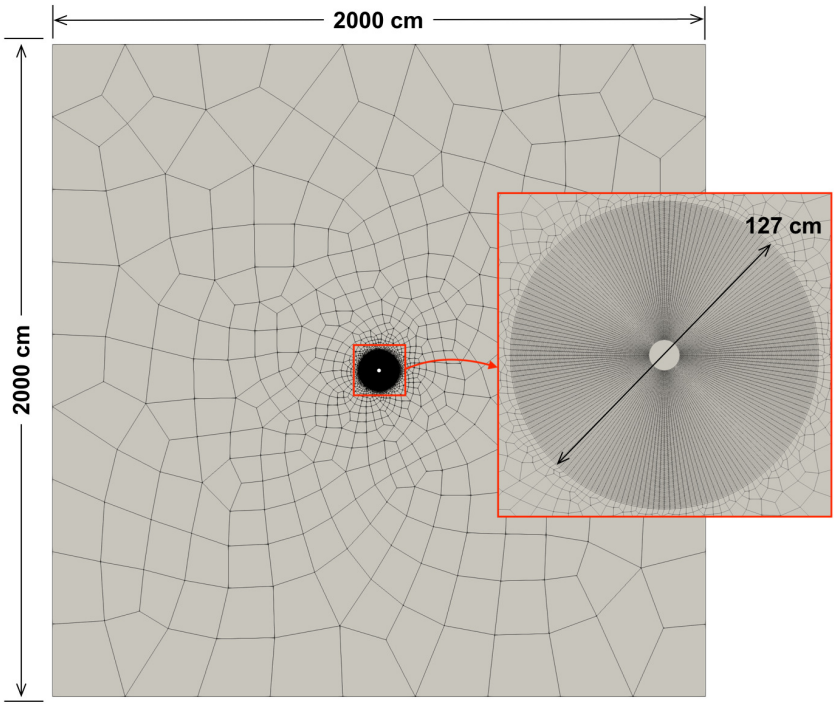

Figure 2.11: Numerical mesh of the wellbore problem

The propagation of hydraulic fractures from the wellbore under anisotropic *in situ*

stress condition is investigated. Fractures are assumed to initiate from a point on the wellbore wall at two initiation angles, $\theta = 38°$ and $\theta = 85°$. Each case is simulated under *in situ* stress differences of $\Delta\sigma = 5\ MPa$, $\Delta\sigma = 15\ MPa$, and $\Delta\sigma = 25\ MPa$, where $\Delta\sigma$ is the difference between the maximum (σ_H) and minimum (σ_h) *in situ* stresses acting perpendicular to the wellbore. The initial fluid pressure for the three stress differences are assumed to be $p_0 = 24.96\ MPa$, $p_0 = 34.88\ MPa$, and $p_0 = 44.81\ MPa$ respectively. The value of minimum horizontal stress is $\sigma_h = 20\ MPa$ in all cases.

The numerical mesh used for this example is illustrated in Figure 2.11. A structured mesh is used for a region with a radius of $5R_w$ from the center of the wellbore. The rest of the domain is discretized using an unstructured mesh. The structured section of the mesh has a minimum effective size of $h_e = 0.003\ m$, at the wellbore, and a maximum effective size of $h_e = 0.011\ m$, at $5R_w$. The average effective size of the mesh in the unstructured section varies from $h_e = 0.024\ m$ at $5R_w$ to $h_e = 1.621\ m$ at the outer boundaries of the domain. A constant time increment of $\Delta t = 0.02\ s$ is used for all analyses. The mesh size and time step increment are small enough to ensure the the results presented are converged. We also assume $bM = 0.08E$ for the APM in the undrained HF split. Fluid is assumed to be injected at a rate of $Q_{inj} = 10^{-4}\ \frac{m^3}{s \cdot m}$. The admissible tolerance of error is $\tau = 10^{-12}$ for the normalized $L2$ norm of the coupling residual, and $\eta = 10^{-2}$ for the satisfaction of the global continuity constraint.

The final trajectories of both the 38° and 85° fractures are illustrated in Figure 2.12 under different values of *in situ* stress difference. The fracture is expected to propagate without kinking under an isotropic stress state, i.e., $\Delta\sigma = 0$. Hence, the fracture plane for the isotropic stress condition is shown as a reference in this figure. As expected, the

fracture trajectories deviate from the reference path to align with the orientation of the minimum *in situ* stress as the stress state deviates from isotropic. An increase in the stress difference enforces a sharper kink in the fracture path and a faster alignment with the direction of the minimum *in situ* stress. Hence, the fracture path with the smallest $\Delta\sigma$ lies above all other trajectories, with the smallest deviation from the reference path. Results for the drained HF split are not show since they failed to converge early on in the analysis. Results for the fully coupled model are not shown, as they are indistinguishable from those of the undrained split.

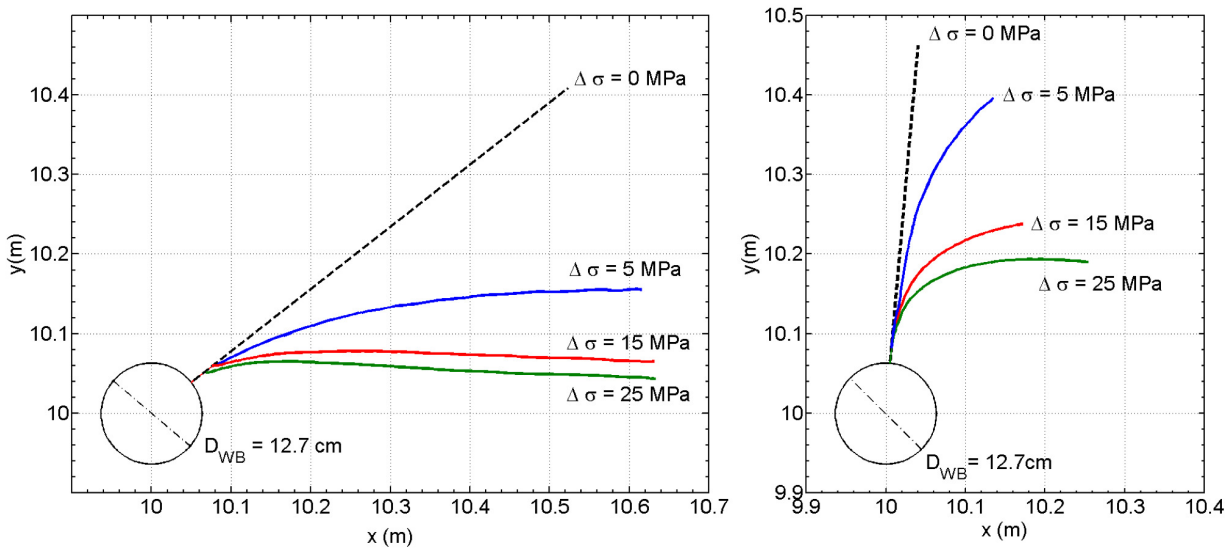

Figure 2.12: Simulated fracture trajectories, using the undrained HF split, of fractures initiated from a wellbore at angles 38° (left) and 85° (right) from the maximum *in situ* stress under anisotropic stress conditions

Figure 2.13 depicts the wellbore pressure of the 38° fracture under *in situ* stress difference $\Delta\sigma = 25\ MPa$ for both undrained and drained HF splits. For an analysis with constant time increments, $\Delta t = 0.02\ s$, the undrained HF split yields a relatively smooth

pressure curve, which initially rises to a peak value and then gradually decreases to a minimum asymptotic value, i.e., the local value of *in situ* stress in the direction perpendicular to the fracture. The drained HF split, however, exhibits a numerical instability after the peak pressure is reached. Amplified oscillations in the injection pressure appear prior to a complete failure to converge. The oscillatory pressure results in similar oscillations in the wellbore fracture aperture, as seen in Figure 2.13. It is clear from this example the the new undrained HF split proposed here is more robust to the drained HF split ($P \rightarrow W$ scheme) previously used in HF models. In the scale of Figure 2.13 for fracture aperture and wellbore pressure, the fully coupled solution is indistinguishable from the undrained HF split solution and so not shown.

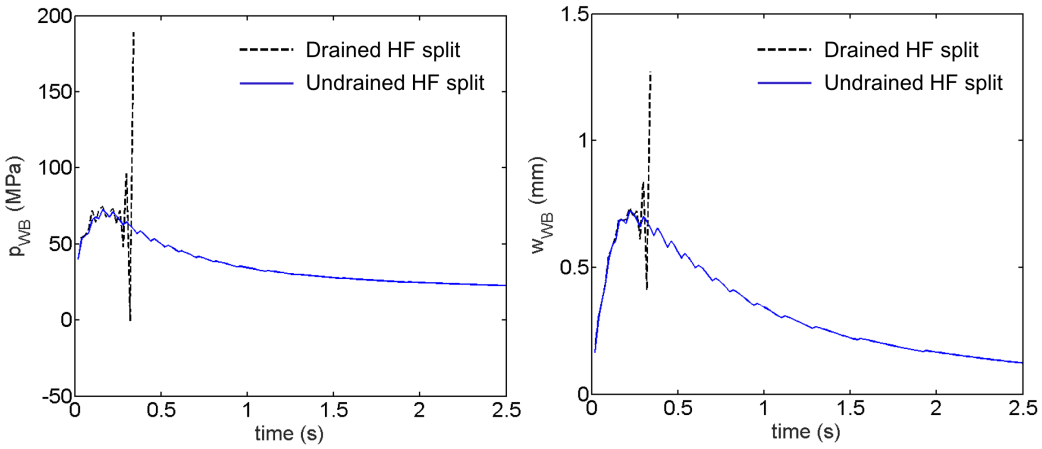

Figure 2.13: Fluid pressure and fracture aperture at the wellbore for traditional drained and new undrained HF splits using constant time increments, $\Delta t = 0.02\ s$. The drained HF split is interrupted as the global continuity condition has not been met after 100 iterations.

Figures 2.14 and 2.15 depict the change in the local stress field due to the propagation of the 38° and 85° fractures from the pressurized wellbore. The stress contours highlight three regions of stress concentrations. As expected there are stress concentrations at both

the wellbore and the fracture tip. There is also a third stress concentration in σ_x and σ_y mid-way along the fracture path which is caused by a combination of the in-situ stresses, the small radius of curvature of the fracture path, and the fluid pressure applied normal to the fracture surface. It is interesting to note that the drained HF split breaks down near the point in the simulation where the radius of curvature in the fracture path becomes small.

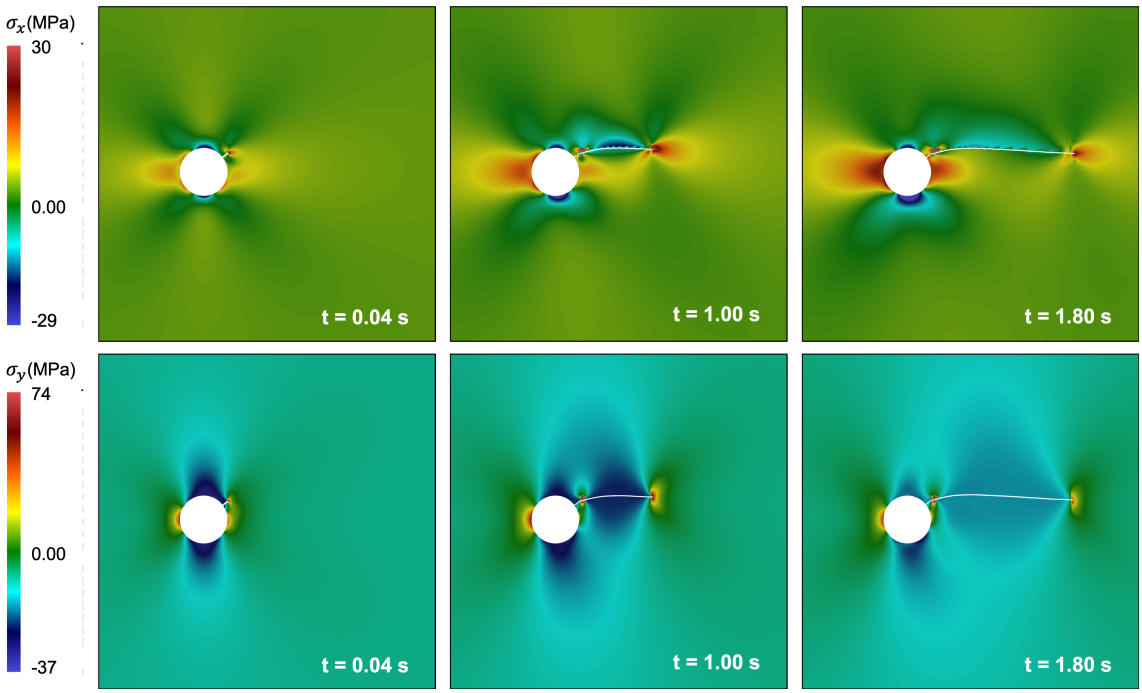

Figure 2.14: Contours of stress, σ_x (top) and σ_y (bottom), around the wellbore, simulated using the new undrained HF split, for propagation of a hydraulic fracture initiated at an angle 38° from σ_{max} under anisotropic stress conditions with $\Delta\sigma = 25\ MPa$

Figure 2.16 shows the normalized $L2$ norm of the residual, $\bar{r}$, for the fully coupled and undrained HF models at various times. Convergence curves are shown for models with $\Delta\sigma = 25\ MPa$. As seen in the figure, at the initial time steps ($t = 0.04\ s$), the

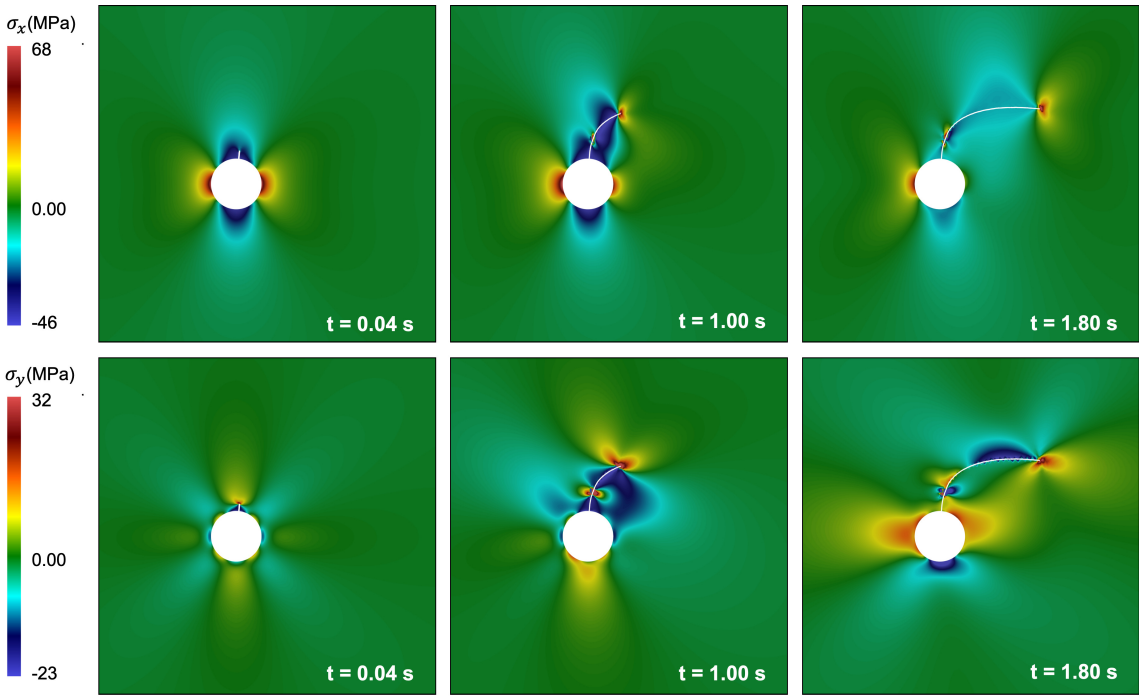

Figure 2.15: Contours of stress, σ_x (top) and σ_y (bottom), around the wellbore, simulated using the new undrained HF split, for propagation of a hydraulic fracture initiated at an angle 85° from σ_{max} under anisotropic stress conditions with $\Delta\sigma = 25\ MPa$

two algorithms converge almost similarly with the undrained HF split converging slightly faster than the fully coupled model. As time passes, the fully coupled model shows better convergence than its undrained counterpart, as would be expected. Convergence graphs resemble bilinear curves in the semi-logarithmic space with an initially flatter segment followed by a sharper drop of the residual norm. Convergence behavior is almost similar for both the fully coupled and undrained HF algorithms in the initial segment of the convergence curves. However, the fully coupled algorithm converges faster in the second segment. Generally, the fully coupled model converges faster than the undrained HF split. The maximum number of iterations during these simulations was 11 for the fully coupled

model and 17 for the undrained HF split. The convergence curves are smooth for both algorithms and no evidence of oscillations are detected.

To compare the computational cost of the two schemes, the CPU time required for one iteration of the fully coupled and undrained HF schemes are measured. The average CPU time for one iteration is $t_{CPU}^{iter} = 0.587\ s$ for the fully coupled and $t_{CPU}^{iter} = 0.604\ s$ for the undrained HF scheme. The comparison of the CPU times indicates that the relative cost per iteration for the two schemes are comparable. Therefore, the total computational cost depends on the number of iterations that each of the two schemes require in order to achieve convergence. Generally, the undrained HF split is slightly costlier than the fully coupled scheme as it requires more iterations to converge.

The convergence/robustness of the drained HF split with a smaller time increment, $\Delta t = 0.001\ s$ (20 times smaller) was also investigated. The spurious oscillations persist and do not attenuate when the time increment is decreased. Therefore, one is unlikely to achieve a stable solution for the problem by employing the drained HF split with sufficiently small time increments. The results presented here are consistent with those presented by Gordeliy and Peirce [52] in which they characterized the $P \rightarrow W$ scheme (i.e., the drained HF split) as being problematic. The lack of robustness of the drained HF split was foreshadowed by Kim et al. [71], who demonstrated the unconditional instability of the drained split in poromechanics.

Hydraulic fracturing is a particular case of fluid-solid interaction. In fluid-solid interaction problems, numerical oscillations (instability) in the solution are often observed when equal-order approximations are used for both fluid pressure and solid displacements (LBB

condition [77, 10, 42, 13]). In this study, however, we did not detect any oscillatory behaviour in the solution of neither the fully coupled model nor the undrained HF splits, even when using similar orders of approximation for the displacement of the solid (bilinear) and the fluid pressure (linear). This was a surprising outcome, as it would be expected that oscillation free results would required different orders of approximation.

Only the drained HF split exhibits oscillations of the fluid pressure field, similar to those observed due to a violation of the LBB condition. Since these oscillations do not exist in the fully coupled nor undrained solutions, we attribute these oscillations to deficiencies in the drained split scheme rather than solely phenomena from the LBB conditions.

2.5 Conclusions

In this chapter a new sequential coupling scheme, the undrained HF split, for the simulation of hydraulic fractures (HF) in impermeable media was presented and compared to the simple $P \rightarrow W$ scheme and a fully coupled scheme. The new splitting scheme (undrained HF split) was developed using an analogy to the undrained split developed in poromechanics. It was also found that the $P \rightarrow W$ scheme used in HF simulation is analogous to the drained split for poromechanics (known to be unstable), leading to it being labeled the drained HF split.

The undrained HF split was implemented in the context of the extended finite element method; however, it can be applied more generally. The implementation was first qualitatively verified by a comparison with the KGD solution. It was observed that the fracture

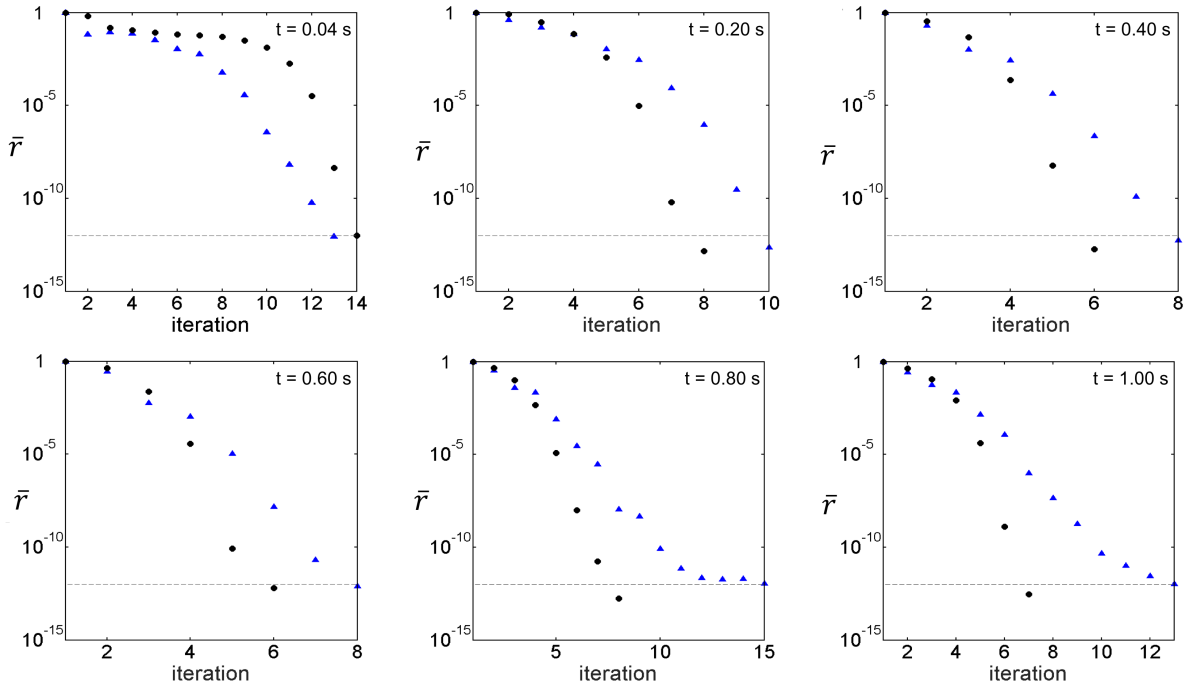

Figure 2.16: Comparison of convergence curves of the fully coupled model (black circles) and the undrained HF split (blue triangles) for 1 s of simulation with $\Delta\sigma = 25\ MPa$ (Dashed lines indicate the admissible tolerance of error, $\tau = 10^{-12}$)

tip in the KGD model is between the physical and mathematical tips of the cohesive HF models and that the physical tip tends to that of the KGD model as the fracture energy tends to zero, as expected. Next, it was demonstrated that the undrained HF split can successfully model the non-planar trajectories of hydraulic fractures initiated from a well-bore under various in-situ stress state. The trajectories are shown to be mainly affected by the orientation of the initial fracture and the intensity of stress anisotropy. The fractures propagates in a way to orient themselves perpendicular to the minimal principal stress, as expected. Material properties such as fracture toughness and fluid viscosity where found to affect the distribution of fracture aperture and fluid pressure, but have minor effects on

the fracture trajectories.

In these applications the results from the new undrained HF split are stable, converge with few iterations, and converge to the same solution as the full-coupled scheme. The undrained HF split was generally found to converge slower than the fully coupled model. The undrained HF split results show no evidence of oscillations. In contrast, the drained HF split (the $P \rightarrow W$ scheme), the most commonly reported iterative scheme in the literature, is shown to be unstable and fails to converge even when very small time step sizes are used. It was not possible to successfully simulate the propagation of HFs from a wellbore using the drained HF split.

Chapter 3

Sequential Enforcement of Hydro-Mechanical Coupling: Fixed Stress and Fixed Strain HF Splits

3.1 Introduction

This chapter focuses on the derivation and implementation of a new iterative coupling strategy that, at each iteration, solves the fluid flow subproblem first. A robust iterative algorithm for automatic fluid partitioning in the simulation of multiple fracture domains is also presented in this chapter.

In the poromechanics context, the splits that solve the fluid subproblem first are the fixed stress and fixed strain splits. While the fixed stress split is one of most robust iterative schemes in poromechanics [71, 92, 91], the fixed strain split is known to be only conditionally stable and non-convergent with a fixed number of iterations (i.e., the number of iterations required for convergence grows with time without an upper limit) [71, 91]. Very few research works have used the fixed strain split for the simulation of fluid flow in deformable porous media [17, 151].

In the simulation of hydraulic fractures, the so called $W \rightarrow P$ scheme is analogous to the fixed strain split in poromechanics. The $W \rightarrow P$ algorithm first solves the fluid equation under the assumption of a fixed fracture aperture. Next, the solid displacement and fracture aperture are updated by solving the solid equilibrium equation, assuming that the fluid pressure is fixed. Gordeliy and Pierce have shown that $W \rightarrow P$ scheme is the least accurate scheme in the simulation of hydraulic fractures. The available iterative coupling schemes in the context of hydraulic fracture modeling are generally known to lack robustness [52]. Therefore, developing an alternative iterative algorithm for the simulation of hydraulic fractures, based on the fixed stress split in poromechanics is desirable.

The fixed stress split is a robust iterative algorithm that solves the fluid subprob-

lem under the assumption that the volumetric stress in the porous matrix is fixed. This assumption suggests that the porous matrix may deform when the fluid subproblem is solved; however, the deformation is constrained to yield a fixed volumetric stress in the solid matrix. Kim et al. have shown that the fixed stress split, in porous media analysis, is unconditionally stable. They have also shown that the split is convergent with a fixed number of iterations [71]. Convergence rates are calculated for the first time by Mikelic et al. [92]. The fixed stress split has been used in many research works for the analysis of deformable porous media [7, 8, 151].

In this chapter, we introduce, for the first time, an efficient sequential coupling algorithm based on the analogy of the fixed stress split for simulating HF propagation. The algorithm is named the *fixed stress HF split*. For the purpose of deriving the fixed stress split formulation, the fracture is assumed to be replaced by an Analogous Porous Medium (APM) and the fixed stress HF split is derived using the poromechanics analogy.

The new fixed stress HF split is implemented in a two-dimensional model for the simulation of HFs in an impermeable elastic medium. The model uses the extended finite element method (XFEM) to simulate cohesive hydraulic fracture propagation and the standard finite element method (FEM) is used to simulate transient fluid flow within the fractures.

We also present an iterative automatic flow partitioning algorithm for splitting flow between fractures when flow rate controlled hydraulic fracturing is simulated. The algorithm is developed based on the satisfaction of the global mass conservation for the wellbore and the fractures connected to it.

In what follows, we first present the mathematical formulation of the fully coupled

hydro-mechanical problem. Next, the numerical discretization of the solid and fluid space domains are discussed followed by a brief discussion of the time domain discretization, and the discrete form of the hydro-mechanically coupled system of equations. Solution strategies for solving the coupled system are explained in section 3.3, and the fixed stress split is derived in section 3.3.2. The automatic partitioning algorithm is introduced in section 3.4. Finally, the efficiency of the fixed stress HF split is demonstrated through numerical examples comparing the solution of the proposed split with those of the fully coupled and conventional fixed strain HF splits ($W \rightarrow P$). We conclude the chapter by a discussion and summary.

3.2 Mathematical model

This section provides the mathematical formulation of the hydro-mechanical coupling problem, and the numerical discretization of the time and space domains. The discrete form of the coupled hydro-mechanical problem is derived at the end of this chapter. The HF model consists of a deformable body containing a number of fractures. The fractures are fluid filled. Additional fluid is injected directly into the fractures, causing them to open and propagate. This model is realized using the following mathematical model.

3.2.1 Governing equations

Consider the solid domain, Ω_s, illustrated in Figure 4.1. The solid domain boundary, Γ, is comprised of three mutually exclusive sets, Γ_u, Γ_t, and Γ_c, such that $\Gamma = \Gamma_u \cup \Gamma_t \cup \Gamma_c$

and $\Gamma_u \cap (\Gamma_t \cup \Gamma_c) = \varnothing$, where Γ_u, Γ_t, and Γ_c denote the displacement boundary, traction boundary, and fracture boundary of the domain, respectively. The fracture boundary is also decomposed into its positive and negative faces, Γ_c^+ and Γ_c^-, such that $\Gamma_c = \Gamma_c^+ \cup \Gamma_c^-$ [95].

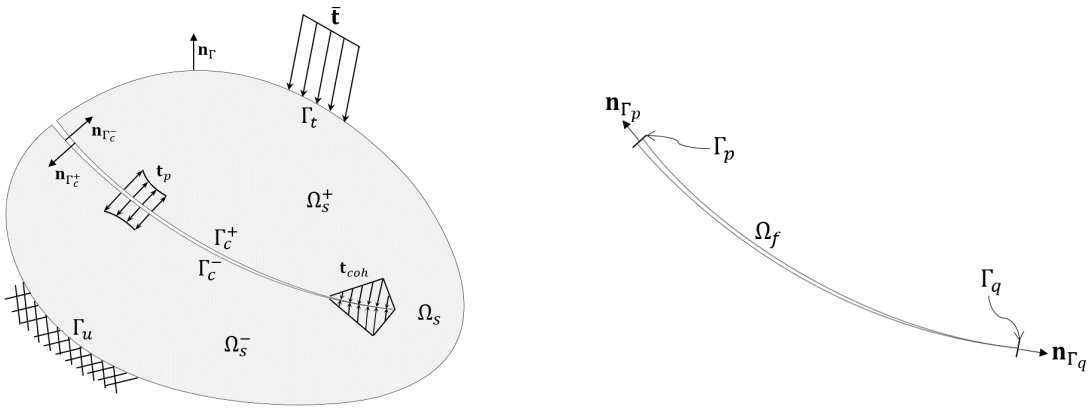

Figure 3.1: Domains of the problem: solid domain (left) and fluid domain (right)

The solid domain is initially in equilibrium under the *in situ* stress field, $\boldsymbol{\sigma_0}$, and is assumed to remain elastic under the applied stresses during the analysis. For a quasi-static problem, the static equilibrium of the system is defined by neglecting the inertia terms from the conservation of momentum equation:

$$\boldsymbol{\nabla} \cdot \boldsymbol{\sigma} + \rho_s \mathbf{b} = \mathbf{0} \tag{3.1}$$

where $\boldsymbol{\sigma}$ is the Cauchy stress tensor, ρ_s is the solid mass density, $\mathbf{b}$ is the vector of body force per unit mass density, and $\boldsymbol{\nabla}$ denotes the gradient operator, in which x and y are the cartesian coordinates in two dimensions. The conservation of angular momentum enforces

the symmetry of the Cauchy stress tensor, i.e., $\boldsymbol{\sigma} = \boldsymbol{\sigma}^\top$. With the assumption of linear elasticity and infinitesimal strains, the constitutive equation of the solid under initial *in situ* stress field, $\boldsymbol{\sigma_0}$ is defined by Hooke's law:

$$\boldsymbol{\sigma} - \boldsymbol{\sigma}_0 = \mathbb{C} : \boldsymbol{\varepsilon} \tag{3.2}$$

where $\mathbb{C}$ is the fourth order elasticity tensor, and $\boldsymbol{\varepsilon}$ is the linear symmetric strain tensor defined by

$$\boldsymbol{\varepsilon} = \frac{1}{2}\left(\boldsymbol{\nabla}\mathbf{u} + \boldsymbol{\nabla}\mathbf{u}^\top\right) \tag{3.3}$$

in which $\mathbf{u}$ is the solid displacement vector. We employ a cohesive fracture model to represent the damaged/plastic region ahead of the fracture tip. In this study, we use a quasi-linear traction-separation law similar to the model presented in [49]. The quasi-linear traction-separation law defines the magnitude of cohesive traction, t^{coh}, as a function of the fracture aperture, w, through

$$t^{coh}(w) = \begin{cases} f_u \dfrac{w}{w_w} & \text{if } w \leq w_w \\ f_u \dfrac{w_c - w}{w_c - w_w} & \text{if } w_w < w \leq w_c \\ 0 & \text{if } w_c < w \end{cases} \tag{3.4}$$

where f_u is the tensile strength of the solid, w_c is the critical aperture, and w_w is known as the weakening aperture, which is the value of aperture corresponding to the maximum value of cohesive traction.

When the solid domain is impermeable, the solid-fluid interaction solely occurs at the fracture surfaces. Hence the fluid domain, Ω_f, is defined by the mid-surface between fractures of the solid domain as illustrated in Figure 4.1. For a quasi-static problem, flow of a viscous fluid within the fractures is governed by the conservation of fluid mass:

$$\frac{\partial w}{\partial t} + \frac{\partial}{\partial s} q = f \tag{3.5}$$

in which w is the fracture aperture, q is the fluid flux, f is the sink/source term, t is the time variable, and s denotes the local fracture coordinate measured from its inlet boundary. The amount of fluid leaking off from the fracture into the solid domain is negligible for an impermeable solid domain. Therefore, the leak-off terms in (3.5) are neglected.

Assuming that fluid flow remains laminar within the fractures and that the fracture faces remain parallel (both are only simplifying assumptions), the relation between flow, q, and pressure, p, along hydraulically driven fractures is given by the flow law:

$$q = -k(w) \frac{\partial}{\partial s} p \tag{3.6}$$

where $k(w)$ is the hydraulic conductivity of the fracture. A discussion on the use of the cubic law in determining $k(w)$ in a cohesive hydraulic fracture model will be presented in section 3.2.2.

A prescribed displacement, $\bar{\mathbf{u}}$, is enforced on the displacement boundary, Γ_u, of the solid domain. The domain is subjected to an external traction, $\bar{\mathbf{t}}$, on its traction boundary, Γ_t. On the fracture boundary, Γ_c, the solid domain is also subjected to tractions due to

fluid pressure and cohesive forces acting perpendicular to the fracture faces. Hence, the set of boundary conditions for the solid equation are taken to be

$$\begin{aligned}
\mathbf{u} &= \bar{\mathbf{u}} \quad \text{on } \Gamma_u \\
\boldsymbol{\sigma} \cdot \mathbf{n}_{\Gamma_t} &= \bar{\mathbf{t}} \quad \text{on } \Gamma_t \\
\boldsymbol{\sigma} \cdot \mathbf{n}_{\Gamma_c^+} &= -\left(p\mathbf{I} + \boldsymbol{\sigma}_0\right) \cdot \mathbf{n}_{\Gamma_c^+} + t^{coh}\mathbf{I} \cdot \mathbf{n}_{\Gamma_c^+} \quad \text{on } \Gamma_c^+ \\
\boldsymbol{\sigma} \cdot \mathbf{n}_{\Gamma_c^-} &= -\left(p\mathbf{I} + \boldsymbol{\sigma}_0\right) \cdot \mathbf{n}_{\Gamma_c^-} + t^{coh}\mathbf{I} \cdot \mathbf{n}_{\Gamma_c^-} \quad \text{on } \Gamma_c^-
\end{aligned} \tag{3.7}$$

where $\mathbf{I}$ is the second order identity tensor, $\mathbf{n}_{\Gamma_t}$ denotes the outward-facing unit normal vector on the traction boundary, and $\mathbf{n}_{\Gamma_c^+}$ and $\mathbf{n}_{\Gamma_c^-}$ are the outward-facing unit normal vectors on the positive and negative faces of the fracture boundary respectively. It should be noted that it's the difference between the fluid pressure and the *in situ* stresses that causes any fracture opening after the initial equilibrium state. This difference is accounted for in (3.7) by superimposing the effect of the fluid pressure and the *in situ* stress field on the fracture boundary/surfaces.

The assumption of an impermeable solid requires that fluid leak-off at any point along the fracture, including the fracture tip, be zero. Therefore, application of the no-flow boundary condition at the fracture tip is necessary. At the inlet boundary, an in-flow rate equal to the prescribed injection rate, Q_{inj}, is prescribed. However, for a given fracture aperture, the conservation equation (3.5) is an elliptic PDE with respect to the fluid pressure, p. Therefore, it is not solvable without an essential boundary condition. To address the solvability issue of (3.5) while accounting for the prescribed injection rate at the inlet and the fracture tip, an additional constraint, the global continuity constraint, is

introduced to augment the problem. The global continuity constraint for an impermeable medium with no fluid leak-off is expressed as [35]

$$Q_{inj} = \int_{\Omega_f} \dot{w} d\Omega \tag{3.8}$$

with $\dot{w}$ denoting the time-derivative of the aperture. Hence, the set of fluid boundary conditions is defined as

$$\begin{aligned} -k\left(w\right)\frac{\partial}{\partial s}p \cdot n_{\Gamma_q} = 0 \quad \text{at} \quad s = L_f \\ p = \bar{p} \quad \text{at} \quad s = 0 \quad \text{subject to:} \quad Q_{inj} = \int_{\Omega_f} \dot{w} d\Omega \end{aligned} \tag{3.9}$$

in which L_f is the fracture length, $\bar{p}$ is fluid pressure at the fracture inlet which is also an unknown of the problem, and $n_{\Gamma_q} = 1$ at the flux boundary (i.e., tip) of the fracture.

The mass conservation equation (3.5) also requires an initial condition on the fracture aperture (or equivalently on the solid displacement). Since the solid domain is initially in an equilibrium state under the *in situ* stress field, one can assume the initial displacement field, $\mathbf{u}_0$, as the reference displacement and express any displacement in the solid domain as an increment to $\mathbf{u}_0$. For the purpose of simplicity, and without loss of generality, we set the initial reference displacement to zero. Therefore, an initial condition for (3.5) can be

$$w_0 = w\left(t = 0\right) = 0 \tag{3.10}$$

This assumption is completely consistent with the solid constitutive equation (4.2), which yields a zero strain when $\boldsymbol{\sigma} = \boldsymbol{\sigma}_0$.

Neglecting the body force term in (3.1), the weak form of the solid governing equation is derived by substituting the stress tensor, $\boldsymbol{\sigma}$, from (4.2) into the equilibrium equation (3.1), multiplying the resultant governing equation by the test function, $\delta\mathbf{u} \in U_0$, and integrating over the solid domain, Ω_s:

$$\begin{aligned}&\int_{\Omega_s} \boldsymbol{\nabla}\delta\mathbf{u} \colon \mathbb{C} \colon \boldsymbol{\varepsilon} d\Omega + \int_{\Omega_s} \boldsymbol{\nabla}\delta\mathbf{u} \colon \boldsymbol{\sigma}_0 d\Omega - \int_{\Gamma_t} \delta\mathbf{u} \cdot \bar{\mathbf{t}} d\Gamma - \int_{\Gamma_t} \delta\mathbf{u} \cdot \boldsymbol{\sigma}_0 \cdot \mathbf{n}_{\Gamma_T} d\Gamma + \\ &\int_{\Gamma_c} [\![\delta\mathbf{u}]\!] \cdot t^{coh}\mathbf{I} \cdot \mathbf{n}_{\Gamma_c} d\Gamma - \int_{\Gamma_c} [\![\delta\mathbf{u}]\!] \cdot (p\mathbf{I} + \boldsymbol{\sigma}_0) \cdot \mathbf{n}_{\Gamma_c} d\Gamma + \int_{\Gamma_c} [\![\delta\mathbf{u}]\!] \cdot \boldsymbol{\sigma} \cdot \mathbf{n}_{\Gamma_c} d\Gamma = \mathbf{0}\end{aligned} \tag{3.11}$$

where $U_0 = \{\delta\mathbf{u} \,|\, \delta\mathbf{u} \in H^1 \times H^1,\ \delta\mathbf{u} = 0 \text{ on } \Gamma_u,\ \delta\mathbf{u} \text{ is discontinuous on } \Gamma_c\}$ is the set of admissible displacement test functions with H^1 being the space of functions whose derivatives are square integrable. The jump in the displacement test functions on the fracture boundary is denoted by $[\![\delta\mathbf{u}]\!] = \left(\delta\mathbf{u}\,|_{\Gamma_c^+} - \delta\mathbf{u}\,|_{\Gamma_c^-}\right)$, and $\mathbf{n}_{\Gamma_c} = \mathbf{n}_{\Gamma_c^-} = -\mathbf{n}_{\Gamma_c^+}$. The weak form of the initial equilibrium of the system suggests that the terms containing $\boldsymbol{\sigma}_0$ in (3.11) should add up to zero, i.e.,

$$\int_{\Omega_s} \boldsymbol{\nabla}\delta\mathbf{u} \colon \boldsymbol{\sigma}_0 d\Omega - \int_{\Gamma_t} \delta\mathbf{u} \cdot \boldsymbol{\sigma}_0 \cdot \mathbf{n}_{\Gamma_T} d\Gamma + \int_{\Gamma_c} [\![\delta\mathbf{u}]\!] \cdot \boldsymbol{\sigma} \cdot \mathbf{n}_{\Gamma_c} d\Gamma = \mathbf{0} \tag{3.12}$$

Hence, the weak form (3.11) is reduced to

$$\int_{\Omega_s} \boldsymbol{\nabla}\delta\mathbf{u} \colon \mathbb{C} \colon \boldsymbol{\varepsilon} d\Omega - \int_{\Gamma_t} \delta\mathbf{u} \cdot \bar{\mathbf{t}} d\Gamma + \int_{\Gamma_c} [\![\delta\mathbf{u}]\!] \cdot t^{coh}\mathbf{I} \cdot \mathbf{n}_{\Gamma_c} d\Gamma - \int_{\Gamma_c} [\![\delta\mathbf{u}]\!] \cdot (p\mathbf{I} + \boldsymbol{\sigma}_0) \cdot \mathbf{n}_{\Gamma_c} d\Gamma = \mathbf{0} \tag{3.13}$$

If we also neglect the sink/source term in (3.5), the weak form of the fluid governing equation is constructed by substituting fluid flux, q, from (3.6) into the conservation equa-

tion (3.5), multiplying the resultant equation by the test function, $\delta p \in P_0$, and integrating over the fluid domain, Ω_f:

$$\int_{\Omega_f} \delta p \frac{\partial w}{\partial t} d\Omega + \int_{\Omega_f} \frac{\partial}{\partial s} \delta p k(w) \frac{\partial}{\partial s} p d\Omega + \int_{\Gamma_q} \delta p \bar{q} d\Omega = 0 \tag{3.14}$$

where the set of admissible pressure test functions is defined as $P_0 = \{\delta p \,|\, \delta p \in H^1,\ \delta p = 0 \text{ on } \Gamma_p\}$

Hence, the coupled problem to be solved is to determine $\mathbf{u} \in U$ and $p \in P$ such that, $\forall \delta \mathbf{u} \in U_0$ and $\delta p \in P_0$,

$$\begin{cases} \displaystyle\int_{\Omega_s} \boldsymbol{\nabla} \delta \mathbf{u} \colon \mathbb{C} \colon \boldsymbol{\varepsilon} d\Omega - \int_{\Gamma_t} \delta \mathbf{u} \cdot \bar{\mathbf{t}} d\Gamma + \int_{\Gamma_c} [\![\delta \mathbf{u}]\!] \cdot t^{coh} \mathbf{I} \cdot \mathbf{n}_{\Gamma_c} d\Gamma - \int_{\Gamma_c} [\![\delta \mathbf{u}]\!] \cdot (p\mathbf{I} + \boldsymbol{\sigma}_0) \cdot \mathbf{n}_{\Gamma_c} d\Gamma = \mathbf{0} \\ \displaystyle\int_{\Omega_f} \delta p \frac{\partial w}{\partial t} d\Omega + \int_{\Omega_f} \frac{\partial}{\partial s} \delta p k(w) \frac{\partial}{\partial s} p d\Omega + \int_{\Gamma_q} \delta p \bar{q} d\Omega = 0 \end{cases} \tag{3.15}$$

where

$$U = \left\{ \mathbf{u} \,|\, \mathbf{u} \in H^1 \times H^1,\ \mathbf{u} = \bar{\mathbf{u}} \text{ on } \Gamma_u,\ \mathbf{u} \text{ is discontinuous on } \Gamma_c \right\}$$

and

$$P = \left\{ p \,|\, p \in H^1,\ p = \bar{p} \text{ on } \Gamma_p \right\}$$

are the sets of admissible displacement and pressure trial functions respectively. The sets of admissible test functions for solid displacement and fluid pressure are defined respectively as

$$U_0 = \left\{ \delta \mathbf{u} \,|\, \delta \mathbf{u} \in H^1 \times H^1,\ \delta \mathbf{u} = \mathbf{0} \text{ on } \Gamma_u,\ \delta \mathbf{u} \text{ is discontinuous on } \Gamma_c \right\}$$

and

$$P_0 = \left\{ \delta p \,|\, \delta p \in H^1,\ \delta p = 0 \text{ on } \Gamma_p \right\}$$

3.2.2 Modified cubic law: elimination of the unphysical singular tip pressure

The cohesive fracture model removes the unphysical singular stresses at the fracture tip; however, a pressure singularity still exists at the tip of a cohesive hydraulic fracture. The reason for such a singularity in the fluid pressure is the dependence of the fracture conductivity, $k(w)$, on the fracture aperture, which, in a cohesive fracture model, vanishes smoothly in the vicinity of the fracture tip.

Consider the cubic law (3.6) as the fluid constitutive model. In the vicinity of the fracture tip, $s \to L_f$, the cubic law suggests that flux, q, must vanish, with cube of the aperture ($q \propto w^3$). Hence, unphysical singular fluid pressures can exist at the tip of a hydraulic fracture even with a cohesive fracture model.

In order to treat the fluid pressure singularity, we use an approach similar to the cohesive fracture model by enforcing a slightly modified version of the fluid constitutive model in the cohesive zone of the fracture, where smooth fracture closure becomes problematic for the fluid model.

A simple treatment for the singular pressure in a cohesive hydraulic fracture model is to modify the fluid constitutive law in a way that the fracture hydraulic conductivity, $k(w)$, tends to a very small value, k_c, instead of zero in the vicinity of the fracture tip, i.e, $\lim_{s \to L_f} k(w) = k_c > 0$. With this assumption, applying a zero flux boundary condition,

$q = 0$, leads to the enforcement of $\frac{\partial}{\partial s}p = 0$ at the tip, and hence prevents pressure singularity at the fracture tip.

The minimum fracture conductivity, k_c, is physically interpreted as the conductivity of the damaged region ahead of the fracture tip. The near-tip damaged region develops micro fractures that remain open, under the applied stresses, due to the dilation of the damaged zone. Such dilation is caused by the interaction of asperities along the micro fractures under a combination of shearing and compressional deformations. Hence, if we assume that the damaged zone is locally lumped to a region along the fracture ahead of its physical tip, i.e., cohesive zone, it is reasonable to also assume that the enhanced permeability, due to the dilation of micro fractures in the damaged zone, is lumped along the same region in the form of a minimum fracture hydraulic conductivity. Similar assumptions have been made in some other research work for simulating hydraulic fracture closure [154].

The minimum hydraulic conductivity can equivalently be represented by a minimum fracture aperture using the cubic law:

$$k_c = \frac{w_c^3}{12\mu} \tag{3.16}$$

where w_c is the minimum hydraulic aperture. To account for the minimum hydraulic conductivity, the cubic law is modified as

$$k(w) = \begin{cases} \dfrac{w^3}{12\mu} & \text{if } w > w_c \\ \dfrac{w_c^3}{12\mu} = k_c & \text{if } w \leq w_c \end{cases} \tag{3.17}$$

The modified cubic law is applied along the cohesive zone of the fracture; hence, we simply assume that the minimum hydraulic aperture is equal to the critical aperture of the cohesive traction-separation law (3.4).

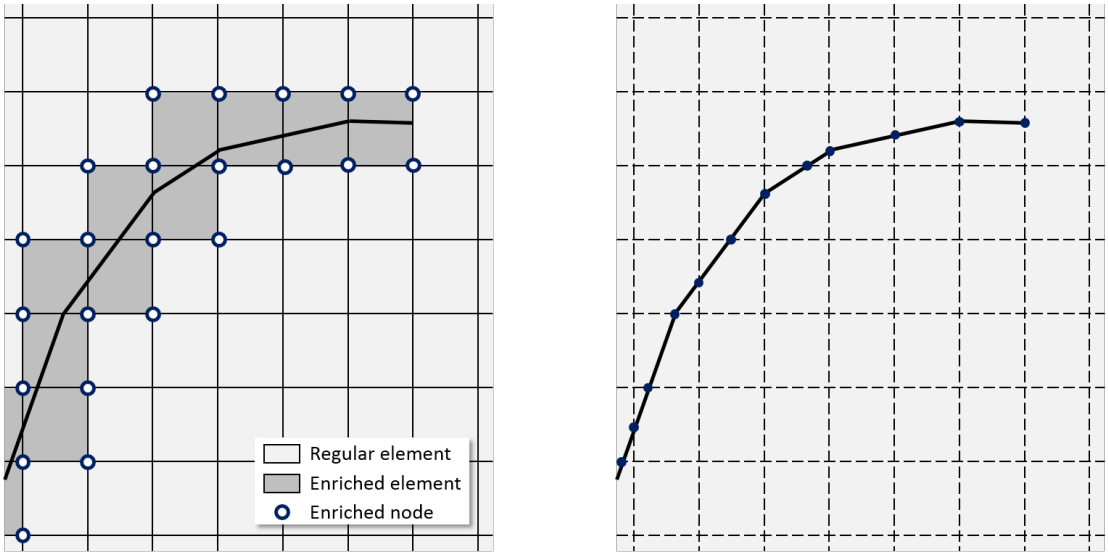

Figure 3.2: Discretization of solid (left) and fluid (right) domains

3.2.3 Discretization

A numerical mesh of quadrilateral elements, as illustrated in Figure 4.3, is used for the discretization of the solid domain, Ω_s. The fracture boundary, Γ_c, is discretized at its intersection with the solid mesh with the fracture tip always located on a solid element edge.

An enriched approximation, with only the Heaviside enrichment functions, is used for the discontinuous solid displacement field. To avoid the use of blending elements, we

employed a shifted enrichment approach [14]. The XFEM approximation, $\mathbf{u}_h$, of the displacement field at point $\mathbf{x} \in \Omega_s$ and time t is defined as

$$\begin{aligned}\mathbf{u}_h(\mathbf{x},t) &= \sum_I N_I(\mathbf{x}) d_I^u(t) + \sum_J N_J(\mathbf{x}) \left[H_c(\mathbf{x}) - H_c(\mathbf{x}_J)\right] d_J^a(t) \\ &\equiv \mathbf{N}^u(\mathbf{x})\mathbf{d}^u(t) + \mathbf{N}^a(\mathbf{x})\mathbf{d}^a(t) \equiv \mathbf{N}(\mathbf{x})\mathbf{d}(t)\end{aligned} \tag{3.18}$$

where I and J are, respectively, the set of all nodes and the set of enriched nodes of the solid mesh. The standard finite element shape functions are denoted by $N_I(\mathbf{x})$, and the terms $d_I^u(t)$ and $d_J^u(t)$ refer to the standard and enriched degrees of freedom, respectively. The discontinuous enrichment function, $H_c(\mathbf{x})$, is defined so

$$H_c(\mathbf{x}) = \begin{cases} -\frac{1}{2} & \text{if } \mathbf{x} \in \Omega_s^- \\ \\ \frac{1}{2} & \text{if } \mathbf{x} \in \Omega_s^+ \end{cases} \tag{3.19}$$

in which Ω_s^+ and Ω_s^- denote the set of points belonging to the solid domain, Ω_s, that are located, respectively, on the positive and negative sides of the fracture (see Figure 4.1).

The standard and enriched degrees of freedom can be compiled into matrices denoted by $\mathbf{d}^u(t)$ and $\mathbf{d}^a(t)$ respectively. Similarly, the standard and enriched shape function matrices are denoted respectively as $\mathbf{N}^u(\mathbf{x})$, and $\mathbf{N}^a(\mathbf{x})$. Finally, combining the standard and enriched matrices of the same type into a single matrix, the total N-matrix and degree-of-freedom vector of the solid are defined as $\mathbf{N}(\mathbf{x}) = \{\mathbf{N}^u(\mathbf{x}) \;\; \mathbf{N}^a(\mathbf{x})\}$ and $\mathbf{d}(t) = \{\mathbf{d}^u(t) \;\; \mathbf{d}^a(t)\}^\top$ respectively.

Considering the spatial derivatives of $\mathbf{u}_h$, the approximated strain in Voigt form is

$$\begin{aligned}\boldsymbol{\varepsilon}_h(\mathbf{x},t) &= \sum_I \boldsymbol{\nabla}^s N_I(\mathbf{x}) d_I^u(t) + \sum_J \boldsymbol{\nabla}^s N_J(\mathbf{x}) \left[H_c(\mathbf{x}) - H_c(\mathbf{x}_J)\right] d_J^a(t) \\ &\equiv \mathbf{B}^u(\mathbf{x})\mathbf{d}^u(t) + \mathbf{B}^a(\mathbf{x})\mathbf{d}^a(t) \equiv \mathbf{B}(\mathbf{x})\mathbf{d}(t)\end{aligned} \tag{3.20}$$

where $\mathbf{B}^u(\mathbf{x})$ and $\mathbf{B}^a(\mathbf{x})$ respectively contain the derivatives of $\mathbf{N}^u(\mathbf{x})$ and $\mathbf{N}^a(\mathbf{x})$. Hence, the total B-matrix of the solid is defined as $\mathbf{B}(\mathbf{x}) = \{\mathbf{B}^u(\mathbf{x}) \;\; \mathbf{B}^a(\mathbf{x})\}$. Moreover, $\boldsymbol{\nabla}^s$ denotes the symmetric gradient operator.

The jump in the displacement across the fracture, $[\![\mathbf{u}]\!] = \mathbf{u}\,|_{\Gamma_c^+} - \mathbf{u}\,|_{\Gamma_c^-}$, can be approximated by substituting $\mathbf{u}_h$ from (3.18) as

$$[\![\mathbf{u}]\!]_h \equiv [\![\mathbf{u}_h]\!] = \mathbf{u}_h\,|_{\Gamma_c^+} - \mathbf{u}_h\,|_{\Gamma_c^-} = \left(\mathbf{N}\,|_{\Gamma_c^+} - \mathbf{N}\,|_{\Gamma_c^-}\right)\mathbf{d} = [\![\mathbf{N}]\!]\mathbf{d} \tag{3.21}$$

Fracture aperture, w, is the normal component of the jump, $[\![\mathbf{u}]\!]$, with respect to the fracture and, hence, is approximated by

$$w_h = [\![\mathbf{u}_h]\!] \cdot \mathbf{n}_{\Gamma_c} = \mathbf{n}_{\Gamma_c}^\top [\![\mathbf{N}]\!]\mathbf{d} \tag{3.22}$$

The fluid domain is discretized at its intersection with the solid mesh, as illustrated in Figure 4.3. Using a standard linear finite element approximation for the pressure field, the approximated fluid pressure, p_h, at point $s \in \Omega_f$ and time t is defined as

$$p_h(s,t) = \sum_L \psi_L(s) p_L(t) \equiv \boldsymbol{\psi}(s)\mathbf{p}(t) \tag{3.23}$$

where L is the set of all nodes of the fluid mesh, $\psi_L(s)$ are the finite element approximation functions, and $p_L(t)$ are the nodal values of fluid pressure, i.e., fluid degrees of freedom. The approximation functions and the degrees of freedom are denoted in matrix form by $\boldsymbol{\psi}(s)$ and $\mathbf{p(t)}$, respectively. The spatial derivative of $p_h(s,t)$ is approximated by

$$\frac{\partial}{\partial s}p_h(s,t) = \sum_L \boldsymbol{\nabla}\psi_L(s)p_L(t) \equiv \boldsymbol{\nabla}\boldsymbol{\psi}(s)\mathbf{p}(t) \tag{3.24}$$

in which $\boldsymbol{\nabla}\boldsymbol{\psi}(s)$ is the matrix containing the spatial derivatives of the pressure approximation functions, $\boldsymbol{\nabla}\psi_L(s)$.

Substituting (3.18)-(3.24) into (3.15), the coupled system is presented in its semi-discrete form as

$$\begin{bmatrix} \mathbf{R}_u \\ \\ \mathbf{R}_p \end{bmatrix} = \begin{bmatrix} \mathbf{K}_{uu}\mathbf{d} - \mathbf{K}_{up}\mathbf{p} + \mathbf{F}_{coh} - \mathbf{F}_{\Gamma_t} - \mathbf{F}_{\Gamma_{c0}} \\ \\ \mathbf{K}_{up}^{\top}\dot{\mathbf{d}} + \mathbf{F}_q - \mathbf{F}_{\Gamma_q} \end{bmatrix} = \mathbf{0} \tag{3.25}$$

in which

$$\mathbf{K}_{uu} = \int_{\Omega_s} \mathbf{B}^{\top}\mathbf{C}\mathbf{B}d\Omega \tag{3.26a}$$

$$\mathbf{K}_{up} = \int_{\Gamma_c} [\![\mathbf{N}]\!]^{\top}\mathbf{n}_{\Gamma_c}\boldsymbol{\psi}d\Gamma \tag{3.26b}$$

$$\mathbf{F}_{coh} = \int_{\Gamma_c} [\![\mathbf{N}]\!]^{\top} t^{coh}(w)\,\mathbf{n}_{\Gamma_c}d\Gamma \tag{3.26c}$$

$$\mathbf{F}_q = \int_{\Omega_f} \boldsymbol{\nabla}\boldsymbol{\psi}^{\top} k(w)\frac{\partial}{\partial s}pd\Gamma \tag{3.26d}$$

$$\mathbf{F}_{\Gamma_q} = \int_{\Gamma_q} \boldsymbol{\psi}^{\top}\bar{q}d\Gamma \tag{3.26e}$$

$$\mathbf{F}_{\Gamma_t} = \int_{\Gamma_t} \mathbf{N}^\top \bar{\mathbf{t}} d\Gamma \tag{3.26f}$$

$$\mathbf{F}_{\Gamma_{c0}} = \int_{\Gamma_c} [\![\mathbf{N}]\!]^\top \bar{\mathbf{t}}_{c0} d\Gamma \tag{3.26g}$$

The time derivative of $\mathbf{d}$ is denoted by $\dot{\mathbf{d}}$, and $\mathbf{C}$ is the matrix representation of the fourth order elasticity tensor, $\mathbb{C}$. Moreover, $\bar{\mathbf{t}}_{c0} = \boldsymbol{\sigma}_0 \cdot \mathbf{n}_{\Gamma_c}$ is the traction acting on the fracture boundary due to the *in situ* stress field. Note that similar approximations are used for test and trial functions in the derivation of (3.25).

We use unevenly distributed time increments, $\Delta t_n = t_n - t_{n-1}$, for the time domain discretization, where t_n represents the nth discrete time step. Using a Backward Euler scheme at time at time $t = t_n$, the time derivative of the solid degree-of-freedom matrix is approximated by

$$\dot{\mathbf{d}}^n \equiv \dot{\mathbf{d}}(t = t_n) = \frac{1}{\Delta t_n}(\mathbf{d}^n - \mathbf{d}^{n-1}) \tag{3.27}$$

where $\mathbf{d}^n = \mathbf{d}\,(t = t_n)$.

Substitution of (3.27) into (3.25) yields the discrete form of the coupled system at time $t = t_n$:

$$\begin{bmatrix} \mathbf{R}_u^n \\ \\ \mathbf{R}_p^n \end{bmatrix} = \begin{bmatrix} \mathbf{K}_{uu}^n \mathbf{d}^n - \mathbf{K}_{up}^n \mathbf{p}^n + \mathbf{F}_{coh}^n - \mathbf{F}_{\Gamma_t}^n - \mathbf{F}_{\Gamma_{c0}}^n \\ \\ \frac{1}{\Delta t_n} \mathbf{K}_{up}^{n^\top} (\mathbf{d}^n - \mathbf{d}^{n-1}) + \mathbf{F}_q^n - \mathbf{F}_{\Gamma_q}^n \end{bmatrix} = \mathbf{0} \tag{3.28}$$

In the next section, we discuss in detail the solution strategies for numerically solving the coupled system of ODEs (3.28).

3.3 Solution strategies

In this section, we explain the coupling strategies for solving the coupled system (3.28). First, a monolithic, also known as fully coupled, strategy based on the Newton-Raphson iterative algorithm is presented. The solution of the fully coupled approach is used as a reference solution in this chapter. Subsequently, the poromechanics analogy is used to introduce two sequential algorithms for the simulation of hydraulic fractures in impermeable media.

3.3.1 Fully coupled solution

The fully coupled approach is known to have the highest convergence rates and minimum stability issues compared to its staggered counterparts and, therefore, is the most robust approach [159, 71]. In this approach, the nonlinear coupled system (3.28) is linearized, using the Newton-Raphson or alike iterative algorithm, and solved implicitly without being staggered into individual subproblems.

Let the residual vector of the coupled problem in the ith iteration at time $t = t_n$ be $\mathbf{R}_i^n(\mathbf{X}) = \{\mathbf{R}_u(\mathbf{X}) \quad \mathbf{R}_p(\mathbf{X})\}_i^n$ and the total degree of freedom vector of the coupled system at the same iteration be $\mathbf{X}_i^n = \{\mathbf{d} \quad \mathbf{p}\}_i^n$. The objective is to find $\mathbf{X}_{i+1}^n$ such that

$$\mathbf{R}_{i+1}^n\left(\mathbf{X}_{i+1}^n\right) = \mathbf{0} \tag{3.29}$$

Substituting $\mathbf{R}_{i+1}^n$ with a first-order approximation from its Taylor expansion, the linearized

coupled system becomes

$$\mathbf{R}_{i+1}^{n} \approx \mathbf{J}_{i}^{n} \Delta \mathbf{X}_{i}^{n} + \mathbf{R}_{i}^{n} = \mathbf{0} \tag{3.30}$$

where $\Delta \mathbf{X}_{i}^{n} = \mathbf{X}_{i+1}^{n} - \mathbf{X}_{i}^{n}$, and the Jacobian of the coupled system in the ith iteration at time $t = t_n$ is

$$\mathbf{J}_{i}^{n} = \frac{\partial \mathbf{R}_{i}^{n}}{\partial \mathbf{X}_{i}^{n}} = \begin{bmatrix} \dfrac{\partial \mathbf{R}_u}{\partial \mathbf{d}} & \dfrac{\partial \mathbf{R}_u}{\partial \mathbf{p}} \\ \dfrac{\partial \mathbf{R}_p}{\partial \mathbf{d}} & \dfrac{\partial \mathbf{R}_p}{\partial \mathbf{p}} \end{bmatrix}_{i}^{n} = \begin{bmatrix} \mathbf{K}_{uu} + \mathbf{K}_{coh} & -\mathbf{K}_{up} \\ \frac{1}{\Delta t}\mathbf{K}_{up}^{\top} + \mathbf{K}_{pu} & \mathbf{K}_{pp} \end{bmatrix}_{i}^{n} \tag{3.31}$$

in which

$$\mathbf{K}_{coh}^{n} = \frac{\partial \mathbf{F}_{coh}^{n}}{\partial \mathbf{d}^{n}} = \int_{\Gamma_c} [\![\mathbf{N}]\!]^{\top} \mathbf{n}_{\Gamma_c} \frac{\partial t^{coh}}{\partial w^{n}} \mathbf{n}_{\Gamma_c}^{\top} [\![\mathbf{N}]\!] d\Gamma \tag{3.32a}$$

$$\mathbf{K}_{pu}^{n} = \frac{\partial \mathbf{F}_{q}^{n}}{\partial \mathbf{d}^{n}} = \int_{\Gamma_c} \boldsymbol{\nabla} \boldsymbol{\psi}^{\top} \frac{\partial}{\partial s} p^{n} \frac{\partial k}{\partial w^{n}} \mathbf{n}_{\Gamma_c}^{\top} [\![\mathbf{N}]\!] d\Gamma \tag{3.32b}$$

$$\mathbf{K}_{pp}^{n} = \frac{\partial \mathbf{F}_{q}^{n}}{\partial \mathbf{p}^{n}} = \int_{\Gamma_c} \boldsymbol{\nabla} \boldsymbol{\psi}^{\top} k\left(w^{n}\right) \boldsymbol{\nabla} \boldsymbol{\psi} d\Gamma \tag{3.32c}$$

The increment of the primary variables is then calculated by $\Delta \mathbf{X}_{i}^{n} = -\left(\mathbf{J}_{i}^{n}\right)^{-1} \mathbf{R}_{i}^{n}$, and the primary variables are updated by $\mathbf{X}_{i+1}^{n} = \mathbf{X}_{i}^{n} + \Delta \mathbf{X}_{i}^{n}$. Iterations continue until the residual, $\mathbf{R}_{i+1}^{n}$, gets sufficiently close to zero, i.e., $\left|\left|\mathbf{R}_{i+1}^{n}\right|\right|_{L2} < \tau$, where $\left|\left|\mathbf{R}_{i+1}^{n}\right|\right|_{L2}$ is the $L2$ norm of the residual and τ is the admissible tolerance of error.

3.3.2 Sequential solutions

In what follows, a poromechanics analogy is used to develop sequential coupling algorithms in which the fluid subproblem is solved first. The presented sequential algorithms are derived based on the fixed strain and fixed stress splits in poromechanics analysis.

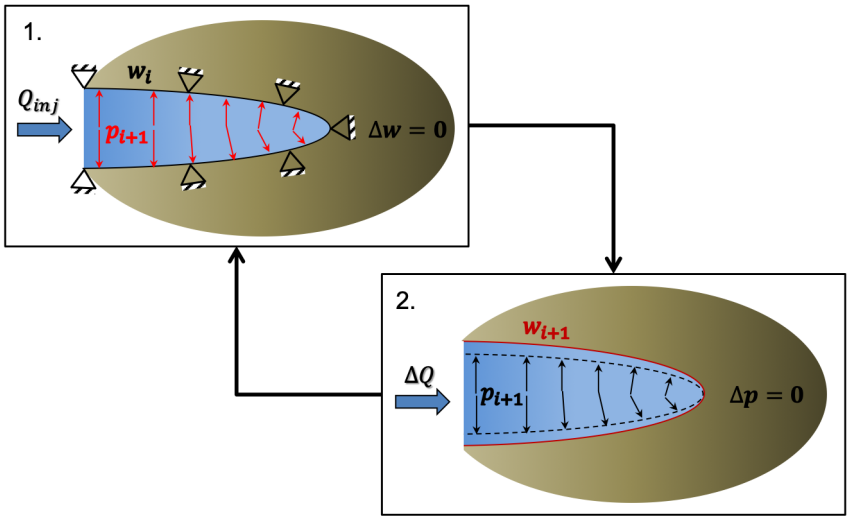

Figure 3.3: Schematic of the fixed strain HF split for a hydraulic fracture in an impermeable medium. Quantities shown in red are solved for in each step and quantities shown in black are frozen during that step

Fixed Strain HF split

The fixed strain sequential approach in the poromechanics analysis is the analogous to the $W \rightarrow P$ split in the hydraulic fracture simulations. The fixed strain approach assumes that the volumetric strain, ε_v, in the porous matrix is fixed when the fluid equation is solved. In other words, the volume of the porous matrix remains unchanged during the solution

of the fluid subproblem. Similarly, one can assume that in a hydraulic fracture simulation, using the fixed strain HF split, the fluid subproblem is solved by fixing the volume of the fracture. This assumption is equivalent to assuming a fixed fracture aperture in the conservation of mass equation, (3.5). The fixed strain HF split is schematically shown in Figure 3.3.

Let i be the iteration counter at time $t = t_n$. The solution of the fluid equation for iteration $i+1$ is computed directly from the second discrete equation in (3.28) as

$$\mathbf{p}_{i+1}^{n} = \mathbf{K}_{pp}^{-1} \left\{ \mathbf{F}_{\Gamma_q}^{n} - \frac{1}{\Delta t_n} \mathbf{K}_{up}^{n^{\top}} \left(\mathbf{d}_{i}^{n} - \mathbf{d}^{n-1} \right) \right\} \tag{3.33}$$

in which, $\mathbf{F}_{q_i}^{n} = \mathbf{K}_{\mathbf{pp}}^{\mathbf{n}} \mathbf{p}_{\mathbf{i}}^{\mathbf{n}}$ is substituted from (3.32)c. In the next step, solid displacement is updated by

$$\mathbf{d}_{i+1}^{n} = \mathbf{d}_{i}^{n} + \left(\mathbf{K}_{uu}^{n} + \mathbf{K}_{coh_i}^{n} \right)^{-1} \mathbf{R}_{u_i}^{n} \tag{3.34}$$

after substituting the solution of the fluid subproblem in (3.28). Table 3.1 summarizes the algorithm for performing the fixed strain HF split.

Fixed Stress HF split

The fixed strain HF split, discussed in section 3.3.2 has been shown to lack robustness and fails to converge in many cases [52].

In the context of poromechanics analysis, the fixed stress split is one of the most robust splits. The fixed stress split is an iterative process in which the volumetric stress in

Table 3.1: Fixed strain HF split algorithm

1.	Set $i = 0$ and initialize $\mathbf{d} = \mathbf{d}_i^n$
2.	Construct $\mathbf{K}_{uu}^n$ from (3.26a) and $\mathbf{K}_{up}^n$ from (3.26b)
3.	Construct $\mathbf{K}_{coh_i}^n$ from (3.32a) and $\mathbf{K}_{pp_i}^n$ from (3.32c)
4.	Calculate $\mathbf{p}_{i+1}^n$ from (3.33)
5.	Compute $\mathbf{R}_{u_i}^n$ from (3.28)
6.	If $\frac{\left\|\left\|\mathbf{R}_{u_i}^n\right\|\right\|_{L2}}{\left\|\left\|\mathbf{R}_{u_0}^n\right\|\right\|_{L2}} < \tau^*$, go to step 10
7.	Update $\mathbf{d}_{i+1}^n$ from (3.34)
8.	$i \longleftarrow i + 1$
9.	Go to step 3
10.	End

* τ is the admissible error of the Newton-Raphson iteration

the porous matrix is assumed to remain unchanged when the fluid subproblem is solved. In other words, the porous matrix is allowed to change volume under the applied pressure; however, the matrix deforms such that its volumetric stress does not change. The application of the fixed stress split to hydraulic fracture simulations may initially be counterintuitive. In this section, we use an analogy to the deformable porous media to introduce a robust sequential algorithm, referred to as the fixed stress HF split, for the simulation of hydraulic fractures in impermeable media.

Let's assume that the fluid domain in the fracture is replaced by an Analogous Porous Medium (APM) as illustrated in Figure 3.4. The APM has a Biot coefficient, b, and Biot modulus, M. A schematic of the fixed stress HF split is shown in Figure 3.5.

Table 3.2: Fixed stress HF split algorithm

0.	Assign values of β
1.	Set $i = 0$ and initialize $\mathbf{d} = \mathbf{d}_i^n$ and $\mathbf{p} = \mathbf{p}_i^n$
2.	Construct $\mathbf{K}_{uu}^n$ and $\mathbf{K}_{up}^n$ from (3.26) and $\mathbf{S}_{pp}$ from (3.43)
3.	Construct $\mathbf{K}_{coh_i}^n$ from (3.32a) and $\mathbf{K}_{pp_i}^{n(SS)}$ from (3.45)
4.	Construct $\mathbf{R}_i^n = \left\{\mathbf{R}_u^n \ \mathbf{R}_p^n\right\}_i^\top$ by computing $\mathbf{R}_{p_i}^n$ from (3.42) and $\mathbf{R}_{u_i}^n$ from (3.28)
5.	if $\frac{\|\|\mathbf{R}_i^n\|\|_{L2}}{\|\|\mathbf{R}_0^n\|\|_{L2}} < \tau^*$, go to step 8
4.	Update $\mathbf{p}_{i+1}^n$ from (3.46)
5.	Update $\mathbf{d}_{i+1}^n$ from (3.34)
6.	$i \longleftarrow i + 1$
7.	Go to step 3
8.	End

* τ is the admissible error of the Newton-Raphson iteration

The rate of the total stress in the APM, $\dot{\sigma}^{(APM)}$, is given by the Biot equation in terms of the effective stress rate , $\sigma'^{(APM)}$, and rate of change of fluid pressure, $\dot{p}$, as:

$$\dot{\sigma}^{(APM)} = \dot{\sigma}'^{(APM)} - b\dot{p} \tag{3.35}$$

Decomposing the total and effective stress tensors in terms of their volumetric and deviatoric components, the total volumetric stress in the APM, $\sigma^{(APM)_v}$, is given by

$$\dot{\sigma}_v^{(APM)} = \dot{\sigma}_v'^{(APM)} - b\dot{p} = K_w \dot{\varepsilon}_v^{(APM)} - b\dot{p} \tag{3.36}$$

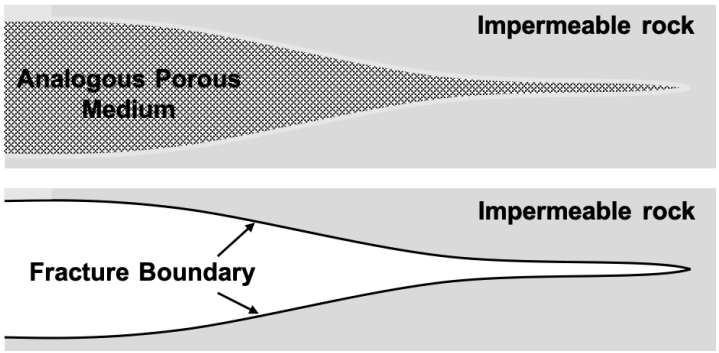

Figure 3.4: Schematic of the hydraulic fracture (bottom) and its Analogous Porous Medium (top)

where $\sigma_v'^{(APM)}$ is the effective volumetric stress of the APM, $\varepsilon_v^{(APM)}$ is the volumetric strain of the APM, and K_w is the APM bulk modulus. The fixed stress HF split requires that the volumetric stress in the APM, $\sigma_v^{(APM)}$, remain unchanged while the conservation of mass is solved for the fluid pressure , i.e., $\sigma_v^{(APM)} = 0$. Substituting this condition in (3.36), the volumetric strain rate can be written in terms of the rate of change in pressure as:

$$\dot{\varepsilon}_v^{(APM)} = \frac{b}{K_w}\dot{p} \tag{3.37}$$

Moreover, the rate of change in the fluid mass content of the APM, $\dot{\xi}$, is given by

$$\dot{\xi} = b\dot{\varepsilon}_v^{(APM)} + \frac{1}{M}\dot{p} \tag{3.38}$$

The change in the fluid mass content of the fracture and that of the APM has to be the same; therefore, for a unit width of the fracture perpendicular to the plane of analysis,

the following equality has to be satisfied:

$$\frac{\partial w}{\partial t} = \dot{\xi} = b\dot{\varepsilon}_v^{(APM)} + \frac{1}{M}\dot{p} \tag{3.39}$$

Substituting (3.37) into (3.39), the rate of change in the fluid mass content of the fracture is rewritten as

$$\frac{\partial w}{\partial t} = \beta\dot{p} \quad \text{with} \quad \beta = \frac{b^2}{K_w} + \frac{1}{M} \tag{3.40}$$

where β is the APM coefficient for the fixed stress HF split, which accounts for both fluid compressibility and fracture compliance.

Substituting (3.40) into the weak form of fluid mass conservation equation leads to the weak form of the fluid equation under fixed stress condition takes the form

$$\beta \int_{\Omega_f} \delta p \frac{\partial p}{\partial t} d\Omega + \int_{\Omega_f} \frac{\partial}{\partial s}\delta p k(w) \frac{\partial}{\partial s} p d\Omega + \int_{\Gamma_q} \delta p \bar{q} d\Omega = 0 \tag{3.41}$$

Using a backward Euler differentiation scheme, the discrete form of (3.41) for iteration i at time $t = t_n$ is written as

$$\mathbf{R}_{p_i}^n = \frac{\beta}{\Delta t_n}\mathbf{S}_{pp}^n \left(\mathbf{p}_i^n - \mathbf{p}^{n-1}\right) + \mathbf{F}_{q_i}^n - \mathbf{F}_{\Gamma_q}^n = \mathbf{0} \tag{3.42}$$

where

$$\mathbf{S}_{pp}^{n} = \int_{\Omega_f} \boldsymbol{\psi}^{\top} \boldsymbol{\psi} d\Omega \tag{3.43}$$

Contrary to (3.33), the fixed stress condition, (3.37), makes the fluid equation nonlinear in p, hence an iterative scheme, such as Newton-Raphson, is required for the solution of (3.42). The Jacobian of the Newton-Raphson scheme for the fluid subproblem at iteration i of time $t = t_n$ is derived as:

$$\frac{\partial \mathbf{R}_{p_i}^{n}}{\partial \mathbf{p}_{i}^{n}} = \frac{\beta}{\Delta t_n} \mathbf{S}_{pp}^{n} + \frac{\partial \mathbf{F}_{q_i}^{n}}{\partial \mathbf{p}_{i}^{n}} \tag{3.44}$$

where

$$\begin{aligned} \frac{\partial \mathbf{F}_{q_i}^{n}}{\partial \mathbf{p}_{i}^{n}} &= \int_{\Omega_f} \boldsymbol{\nabla} \boldsymbol{\psi}^{\top} \frac{\partial p_i^n}{\partial s} \frac{\partial k\left(w\right)}{\partial \mathbf{p}_{i}^{n}} d\Omega + \int_{\Omega_f} \boldsymbol{\nabla} \boldsymbol{\psi}^{\top} k\left(w\right) \frac{\partial}{\partial \mathbf{p}_{i}^{n}} \left(\frac{\partial p_i^n}{\partial s} \right) d\Omega \\ &= \beta \int_{\Omega_f} \boldsymbol{\nabla} \boldsymbol{\psi}^{\top} \frac{\partial}{\partial s} p_i^n \frac{\partial k\left(w\right)}{\partial w} \boldsymbol{\psi} d\Omega + \int_{\Omega_f} \boldsymbol{\nabla} \boldsymbol{\psi}^{\top} k\left(w\right) \boldsymbol{\nabla} \boldsymbol{\psi} d\Omega = \mathbf{K}_{pp_i}^{n^{(SS)}} \end{aligned} \tag{3.45}$$

with $\mathbf{K}_{pp_i}^{n^{(SS)}}$ denoting the fixed stress fluid tangent stiffness matrix, and $\dfrac{\partial w}{\partial p} = \beta$ being inferred from (3.40). The solution of the fluid subproblem is updated by

$$\mathbf{p}_{i+1}^{n} = \mathbf{p}_{i}^{n} + \left(\frac{\beta}{\Delta t_n} \mathbf{S}_{pp}^{n} + \mathbf{K}_{pp_i}^{n^{(SS)}} \right)^{-1} \mathbf{R}_{p_i}^{n} \tag{3.46}$$

Once fluid pressure is calculated, solid displacement is updated by (3.34). The algorithm for performing the fixed stress HF split is presented in Tabel 3.2.

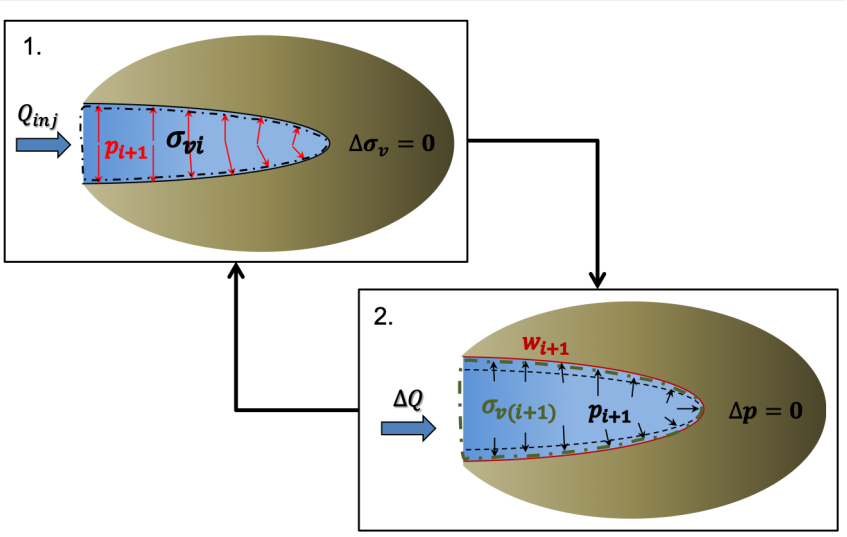

Figure 3.5: Schematic of the fixed stress HF split for a hydraulic fracture in an impermeable medium. Quantities shown in red are solved for in each step and quantities shown in black are frozen during that step

3.4 Automatic Fluid Partitioning using Global Conservation of Mass

In this section, we discuss an iterative algorithm, based on the global conservation of mass, for the automatic partitioning of wellbore fluid between fractures connected to the wellbore. The algorithm can be used for multiple-wellbore problems as well.

The boundary conditions, (3.7) and (3.9), were incorporated into the weak forms of the governing equations. However, the global continuity constraint is yet to be enforced. In what follows, we present an iterative algorithm that implicitly satisfies the global continuity constraint, instead of enforcing it explicitly to the hydro-mechanically coupled system of equation.

The mass conservation equation (3.5) with the flow law (3.6) is a partial differential equation of the elliptic type with respect to fluid pressure, p. Therefore, for a given fracture aperture, w, at least one essential boundary condition for fluid pressure is required to make (3.5) solvable. On the Dirichlet boundary, the fluid flow is a part of the solution of the fluid model and cannot be controlled externally. In other words, one cannot guarantee that the amount of fluid flowing into or out of the fracture from the the Dirichlet boundary satisfies (3.8). To ensure mass conservation, a global continuity constraint needs to be enforced in the coupled system of equations [35]. The global continuity constraint for a problem with constant inlet and leak-off flow rates can be introduced as

$$\left(Q_{inj} - Q_{leak-off}\right) t = \int_{\Omega_f} w d\Omega \tag{3.47}$$

where Q_{inj} and $Q_{leak-off}$ are the injection and leak-off flow rates respectively. When the inlet flow and/or the leak-off flow are not constant, (3.47) can be written in the incremental form as

$$\left(Q^n_{inj} - Q^n_{leak-off}\right) \Delta t_n = \int_{\Omega_f} \left(w^n - w^{n-1}\right) d\Omega \tag{3.48}$$

which can be modified as

$$\left(Q^n_{inj} - Q^n_{leak-off}\right) = \int_{\Omega_f} \dot{w}^n d\Omega \tag{3.49}$$

where the superscript, n, denotes the nth discrete time step. The leak-off flow rate is

calculated by summing up the leak-off flux, q_l, along the fracture, i.e.,

$$Q^n_{leak-off} = \int_{\Omega_f} q^n_l \, d\Omega \tag{3.50}$$

To enforce the global continuity constraint to the discrete form of the hydro-mechanically coupled system (3.28), Khoei et al. [68] suggested employing an external loop that adjusts the inlet pressure in accordance with the required change in the fracture volume at each time step. The study used the analytical solution presented by Geertsma and de Klerk [48] to introduce a power-law ratio that relates the inlet pressure to the instantaneous change in the fracture volume (i.e., the instantaneous injection rate). The injection pressure was, therefore, adjusted according to the required correction to the injection rate in order to satisfy the global continuity constraint. The proposed approach was shown to converge quickly for the self-similar plane strain hydraulic fracture problem [68]; however, tests of this algorithm for smaller values of fracture toughness (e.g., $K_{Ic} = 0.5\ MPa\sqrt{m}$) did not converge. Therefore, a new algorithm has been developed which is more robust.

The idea of enforcing the global continuity constraint through an external loop is still used. A simple adjustable linear algorithm, instead of the power-law ratio presented in [68] is used, that can be applied to a variety of hydraulic fracture problems. In all problems solved reasonable convergence rates are obtained.

When no-flow boundary condition is enforced at the fracture tip, i.e., $q_{tip} = 0$, the boundary condition at the inlet has to be a prescribed pressure, i.e., $p_{inlet} = \bar{p}$. To ensure that the volume of the fracture under the imposed inlet pressure can accommodate the injected fluid volume, we assume that the required increment in the injection pressure, $\Delta\bar{p}$,

in the kth iteration at time $t = t_n$ is related to the required change in the inlet flow rate, ΔQ, through a linear relation

$$\Delta \bar{p}_k^n = -\lambda_k^n \Delta Q_k^n \tag{3.51}$$

where $\Delta Q_k^n = Q_k^n - Q_{inj}^n$ and $\Delta \bar{p}_k^n = \bar{p}_{k+1}^n - \bar{p}_k^n$. The coefficient λ_k^n is a positive coefficient with unit $\left[\frac{Pa \cdot s}{m^2}\right]$, and the negative sign denotes that pressure decreases if the flow rate at the inlet is greater than the required injection rate and increases when Q_k^n is less than Q_{inj}^n. In order to come up with an estimate for the coefficient λ_k^n, one can approximate λ_k^n by the slope of the tangent line to the $p - Q$ curve at time $t = t_n$ as

$$-\frac{\Delta \bar{p}_k^n}{\Delta Q_k^n} = \lambda_k^n \approx \frac{\partial \bar{p}_k^n}{\partial Q_k^n} \tag{3.52}$$

Let us neglect the leak-off term and assume that an expression similar to the one introduced in [48], defines the inlet pressure, $\bar{p}$, as a function of the instantaneous flow rate, Q, in the kth iteration at time $t = t_n$. Hence,

$$\bar{p}_k^n = \sigma_{min} + 0.96 \left(\frac{2G^3\mu}{(1-\nu)^3}\right)^{\frac{1}{4}} (Q_k^n)^{\frac{1}{4}} (L^n)^{-\frac{1}{2}} \tag{3.53}$$

With this assumption, the coefficient λ_k^n is approximated by

$$\lambda_k^n \approx \frac{\partial \bar{p}_k^n}{\partial Q_k^n} = \frac{\partial}{\partial Q_k^n} \left(0.96 \left(\frac{2G^3\mu}{(1-\nu)^3}\right)^{\frac{1}{4}} (Q_k^n)^{\frac{1}{4}} (L_n)^{-\frac{1}{2}}\right) = 0.24 \left(\frac{2G^3\mu}{(1-\nu)^3}\right)^{\frac{1}{4}} (Q_k^n)^{-\frac{3}{4}} (L^n)^{-\frac{1}{2}} \tag{3.54}$$

where G is the shear modulus of the solid, ν is its Poisson's ratio, μ is the dynamic viscosity of the fluid, and L_n denotes the length of the fracture at time $t = t_n$.

Alternatively, one can keep the coefficient λ constant at each time step, without updating it in each iteration, by substituting the target value of flow rate, $Q^n = Q^n_{inj}$. In this case, the coefficient, λ^n, is approximated by

$$\lambda^n \approx 0.24 \left(\frac{2G^3\mu}{(1-\nu)^3} \right)^{\frac{1}{4}} \left(Q^n_{inj}\right)^{-\frac{3}{4}} \left(L^n\right)^{-\frac{1}{2}} \tag{3.55}$$

It is evident from (3.55) that the coefficient, λ^n, at each time step is only a function of the fracture length, L^n, and the injection rate, Q^n_{inj}. Once the initial value of λ is calculated, one can reduce the value of λ at each time step to maintain the convergence rate, using

$$\lambda^{n+1} = \lambda^n \left(\frac{Q^{n+1}_{inj}}{Q^n_{inj}} \right)^{-\frac{3}{4}} \left(\frac{L^{n+1}}{L^n} \right)^{-\frac{1}{2}} \tag{3.56}$$

Substituting λ into (3.51), the inlet pressure is updated by

$$\bar{p}^n_{k+1} = \bar{p}^n_k + \Delta\bar{p}^n_k \tag{3.57}$$

The iterations are continued until the inlet pressure and deformations satisfies the global continuity constraint, (3.49) within a satisfactory tolerance of error.

When fluid leak-off is not negligible, the KGD solution with leak-off can be used in (3.53) to approximate the appropriate correction to the inlet pressure at each iteration. It should be noted that (3.53) only provides the initial predictor of the inlet pressure in the iterative process. When a better estimate of the relation between the inlet pressure and the injection rate is available, one can substitute (3.53) by the available relation and accelerate

the convergence of the iterative process. As will be seen, the inlet pressure update is robust even with multiple cracks propagating in complex ways are simulated.

The fixed stress HF split discussed in section 3.3.2 converts the fluid equation to a parabolic PDE with respect to the fluid pressure, p. Therefore, solution of the fluid sub-problem under the fixed stress condition does not require an essential boundary condition. Therefore, enforcing the global continuity constraint through the iterative process discussed in this section seems unnecessary when using the fixed stress HF split. While this argument is true for simulating only one hydraulic fracture, a problem with multiple hydraulic fracture connected to a wellbore cannot be directly solved without an algorithm that partitions the injected flow rate between the fractures.

3.4.1 Fluid Partitioning Algorithm

The iterative algorithm introduced in this section can effectively serve as an automatic partitioning algorithm for the simulation of multiple hydraulic fractures.

Let n_f be the number of fractures connected to the wellbore. The global continuity constraint, (3.49), can be generalized for a domain with n_f fractures as

$$Q^n_{inj} = \sum_j^{n_f} \int_{\Omega^j_f} \dot{w}^n d\Omega + \sum_j^{n_f} \int_{\Omega^j_f} q^n_l d\Omega \tag{3.58}$$

where Ω^j_f denotes the fluid domain of the jth hydraulic fracture. Equation (3.53) describes the relationship between the wellbore pressure and injection rate for one hydraulic fracture propagating under plane strain conditions. In order to come up with an initial

prediction for λ^n in the multi-fracture problem, we use a weighted average length, $\bar{L}^n$, of all fractures in (3.54)-(3.56), with the weights being the ratio of the current length of each fracture to its initial length:

$$\bar{L}^n = \frac{\sum_{j}^{n_f} w_j L_j^n}{\sum_{j}^{n_f} w_j} \tag{3.59}$$

where $w_j = \frac{L_j^n}{L_j^0}$ is the weight of the jth fracture. The coefficient, λ^n is updated at each time steps using the average length obtained form (3.59) in (3.57).

3.5 Numerical Examples

In this section, the application of the proposed fixed stress HF split for simulating hydraulic fracture propagation in impermeable media is demonstrated through several numerical examples. The propagation of hydraulic fractures from a wellbore with multiple initial fractures is simulated. The simulations are carried out using the fully coupled model and the new fixed stress HF split. First, we consider the simulation of three hydraulic fractures oriented at different angles from a wellbore. The results of the fixed stress HF split are compared against those of the fully coupled model, taken as the reference solution in this example. The convergence of the fixed stress split is investigated through a comparison with the fully coupled model. Next, we use the fixed stress HF split to model a wellbore with four initial fractures. The efficiency of the automatic partitioning algorithm in partitioning

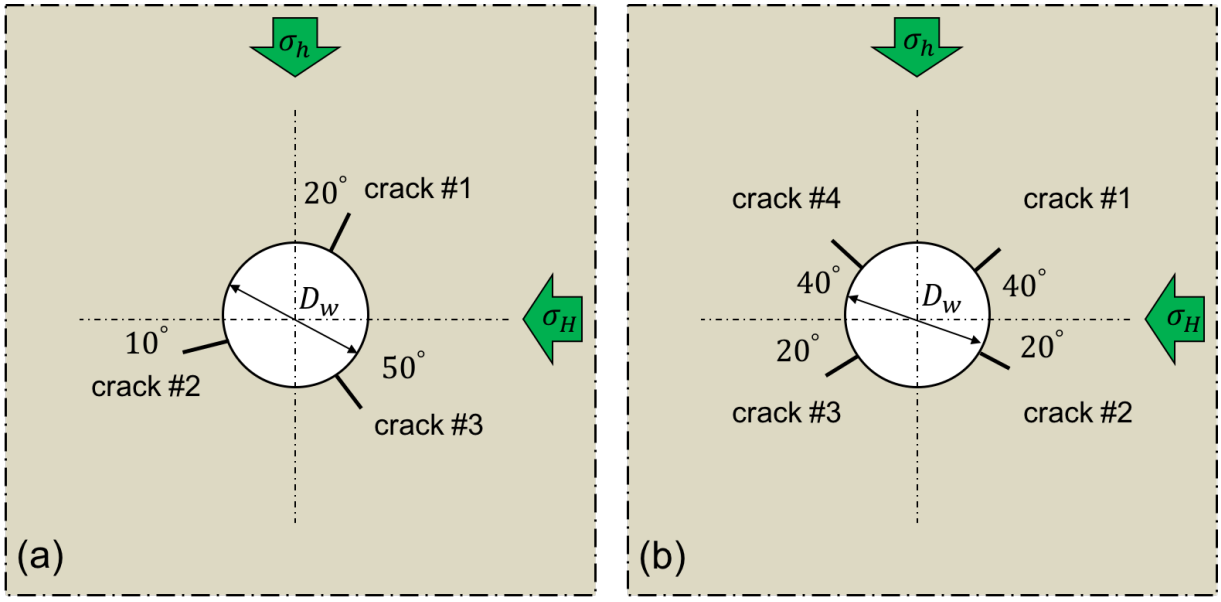

Figure 3.6: Orientation of initial fractures from the wellbore: (a) three fractures and (b) four fractures

flow between the fractures is also demonstrated for both of the examples.

3.5.1 Simulation of a Wellbore with Three Hydraulic Fractures

Consider a wellbore with the diameter of $2R_w = D_w = 24.4\ cm$ ($\approx 9\ in$) drilled in the direction of the intermediate principal *in situ* stress. The initial fractures at the wellbore wall have a length of 4 cm and orientations shown in Figure 3.6a. The formation is assumed to be impermeable with the elastic modulus of $E = 16\ GPa$, Poisson's ratio of $\nu = 0.2$, tensile strength of $T = 0.5MPa$, and fracture energy of $G_c = 90J/m^2$ (fracture toughness of $K_{IC} = 1.22\ MPa\sqrt{m}$). The components of principal *in situ* stress perpendicular to the wellbore are assumed to be $\boldsymbol{\sigma}_H = 20MPa$ and $\boldsymbol{\sigma}_h = 15MPa$. The initial fluid pressure in

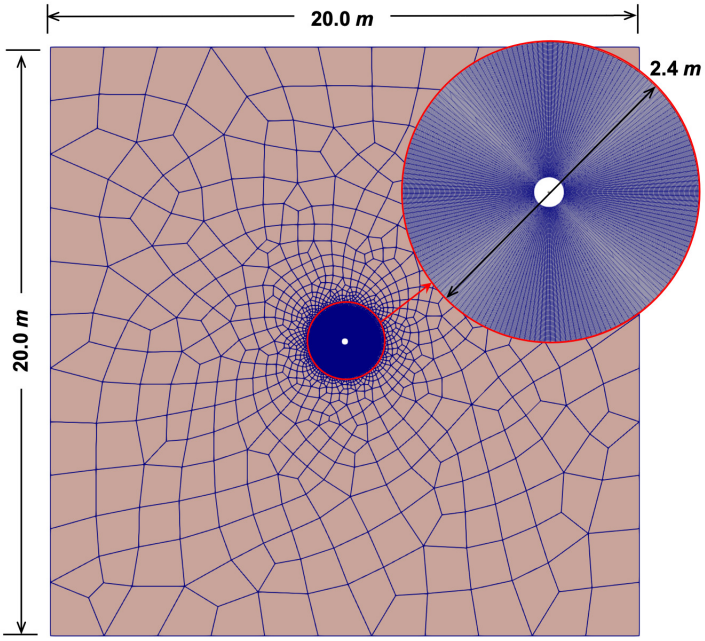

Figure 3.7: The numerical mesh for a 20 $m \times 20$ m domain with a $D_w = 24.4$ cm wellbore

the wellbore is $p_0 = 15.1$ MPa.

A 20 $m \times 20$ m domain is simulated. Figure 3.7 illustrates the numerical mesh of the problem. The domain is divided into two regions. The region from the wellbore wall to a radius of $10R_w$ is discretized with a radially structured mesh of four-node quadrilateral elements. The rest of the domain is discretized using an unstructured mesh of similar type. The minimum and maximum effective element size of the structured mesh are, respectively, $h_e = 0.013$ m and $h_e = 0.042$ m. The unstructured section of the mesh has an average effective element size of $h_e = 0.046$ m at $10R_w$ and $h_e = 1.49$ m at the external boundary. The time domain is discretized by means of constant time increments, $\Delta t = 0.02$ s. The mesh size and the time increment are sufficiently small to ensure the convergence of the presented results. Fluid is injected at the wellbore at a rate of $Q_{inj} = 10^{-4}$ $m^3/s \cdot m$. The

tolerance of normalized error is chosen to be $\tau = 10^{-12}$ for the coupling and $\eta = 10^{-2}$ for the partitioning algorithms. The value of β is chosen to be $4 \times 10^{-10}\ Pa^{-1}$, equal to the compressibility of water, for the fixed stress HF split in this example. The penalty stiffness for enforcing interface contact on the fracture interfaces is set to $k_n = \dfrac{f_u}{w_w} = 0.1\ GPa$.

Figure 3.8 illustrates fracture trajectory and contours of stress, σ_{xx} and σ_{yy}, around the wellbore, estimated by the fixed stress HF split. The predicted trajectories by the fully coupled model and the fixed stress HF split are almost identical. The predicted trajectory is smooth, indicating that the solution is converged using the mesh of Figure 3.7. As expected, only the fracture with the minimum inclination from the direction of the maximum *in situ* stress (crack #2) propagates. The fracture trajectory smoothly aligns with the direction of maximum *in situ* stress.

At the initial time, $t = 0.0\ s$, the wellbore and fractures are in a static equilibrium state under the *in situ* stress field and the initial wellbore pressure. Regions around the wellbore with high compressive stress concentrations are evident. The stress concentration is smaller in the direction of the maximum *in situ* stress; hence, the initial compressive stress acting normal to crack #2 is less than the compressive stress acting normal to the other two cracks. Upon pressurization, the compressive stress concentration at all three fracture tips weakens. Tensile stress develops at the fracture tips, as pressure increases. The tensile stress concentration at the tip of crack #2 reaches the tensile strength of the formation and the fracture propagates. Crack #2 propagates to align itself with the maximum *in situ* stress.

Figure 3.8 shows that a region of tensile stress develops at the wellbore wall, oppo-

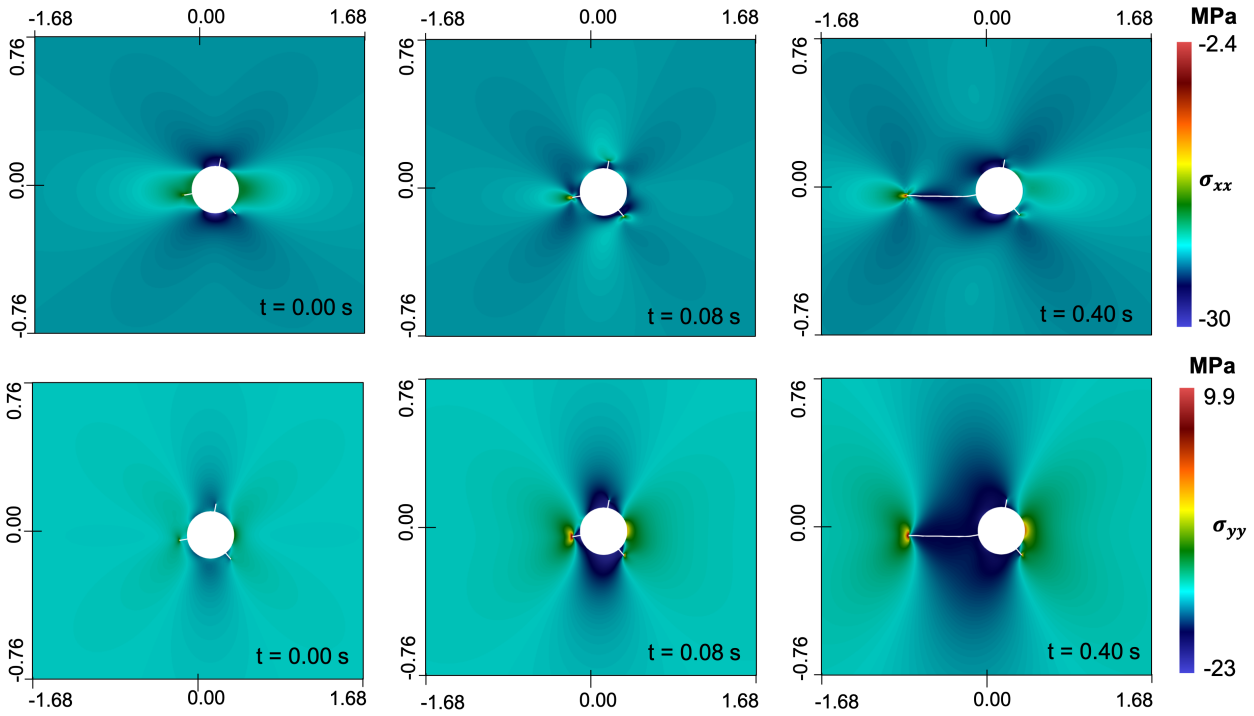

Figure 3.8: Fracture trajectory and contours of stress, σ_{xx} (top) and σ_{yy} (bottom), around the wellbore

site crack #2, when the wellbore pressure reaches the breakdown pressure of crack #2. This tensile stress concentration indicates that, in reality, another fracture initiates at the wellbore at this point.

The wellbore pressure estimated by both the fully coupled and fixed stress HF models are plotted in Figure 3.9. Wellbore pressure monotonically increases from its initial value to a peak pressure equal to the breakdown pressure of crack #2. The pressure then starts to decline as the fracture propagates. Since the breakdown pressure of cracks #1 and #3 are greater than that of crack #2, the other two fractures will not propagate after crack #2 starts growing. When crack #2 temporarily stops propagating (at about $t = 0.2s$,

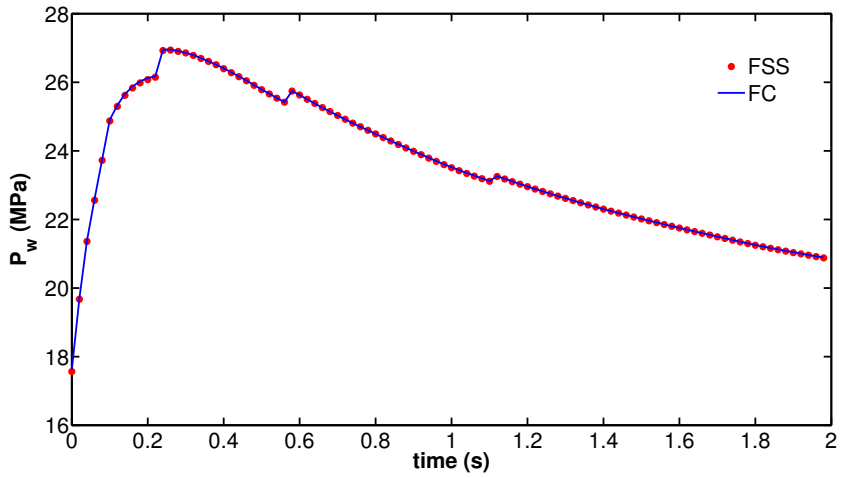

Figure 3.9: Change of wellbore pressure over time estimated by the fully coupled (FC) and the fixed stress HF split (FSS) using constant time increments, $\Delta t = 0.02\ s$

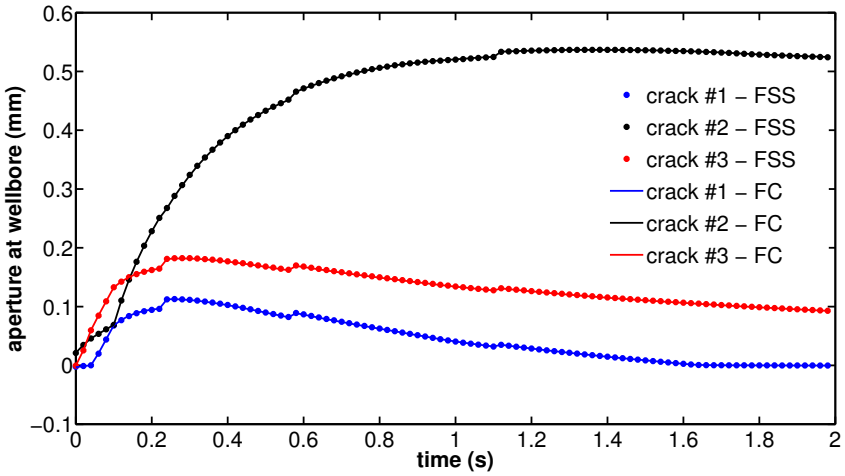

Figure 3.10: Change of fracture aperture at wellbore over time estimated by the fully coupled (FC) and the fixed stress HF split (FSS) using constant time increments, $\Delta t = 0.02\ s$

$t = 0.6s$, and $t = 1.2s$), pressure builds up again in the wellbore. The small jumps observed in the pressure curves in Figure 3.9 indicate this pressure build-up. The pressure

builds for a short while until crack #2 starts to propagate again. The required pressure for propagating crack #2 gets smaller as the fracture grows, hence the pressure curve declines smoothly over time. No evidence of numerical instability (oscillations) is observed in the pressure curves.

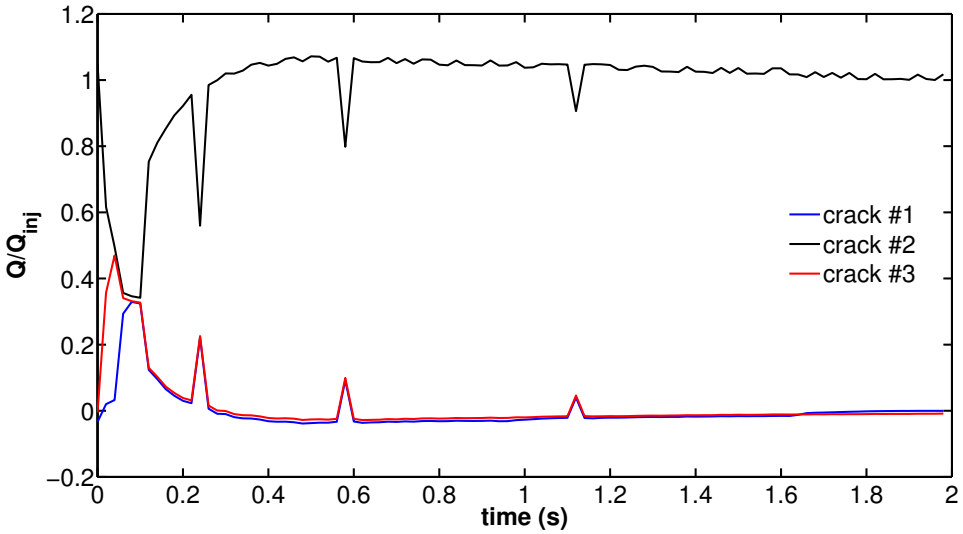

Figure 3.11: Partitioning of the injected fluid, $Q_{inj} = 10^{-4} m^3/s \cdot m$

Fracture aperture at the wellbore for all three fractures are illustrated in Figure 3.10. The figure shows that the aperture of crack #2 increases over time. The wellbore apertures of cracks #1 and #3 increase until the time at which crack #2 starts propagation, and decrease thereafter. Small jumps in the aperture of cracks #1 and #3 are observed and corresponds to the short periods during which crack #2 is not propagating and the wellbore pressure increases suddenly. No spurious oscillation, indicating a numerical instability, is also seen in aperture curves. Figures 3.9 and 3.10 demonstrate convergence of the Fixed stress HF split results to the results of the fully-coupled model.

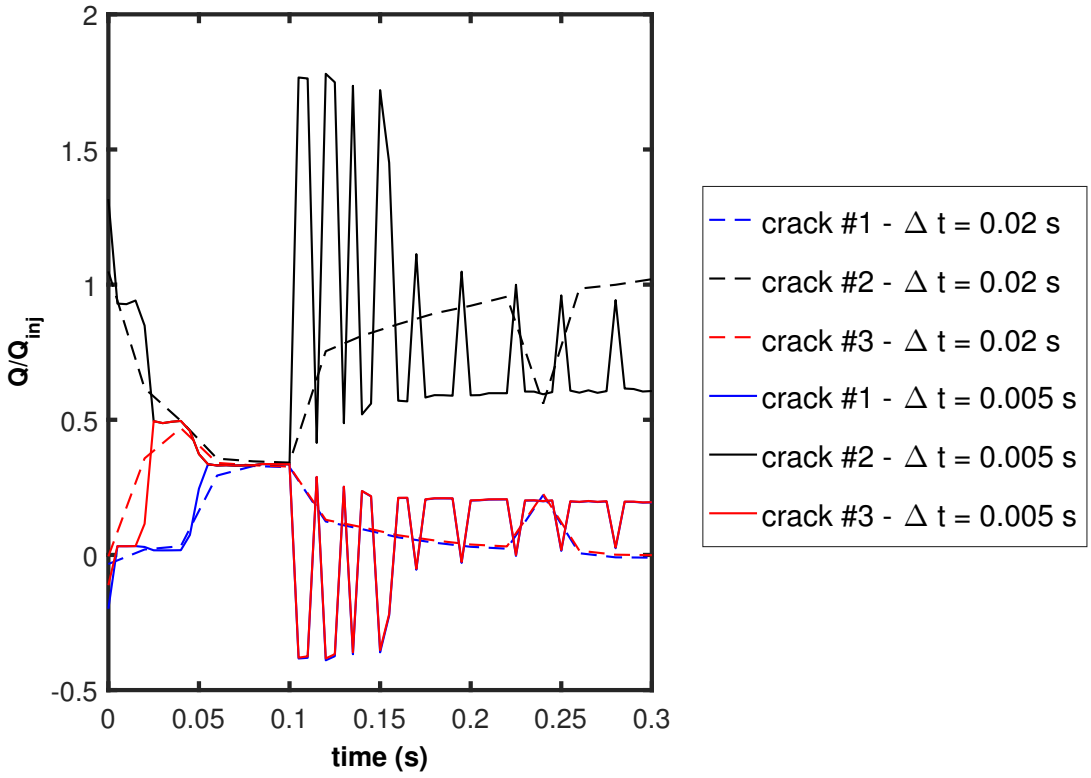

Figure 3.12: Comparison of flow partitioning for $\Delta t = 0.02s$ and $\Delta t = 0.005s$ with $Q_{inj} = 10^{-4} m^3/s \cdot m$

To demonstrate the flow efficiency of the partitioning algorithm, the normalized partitioned flow rates are plotted over time in Figure 3.11. Flow rates are normalized to the total injection rate, Q_{inj}. Crack #2 initially gets most of the injected flow due to its orientation with respect to the *in situ* stress field. When pressure goes up and the compressive stress concentration at the wellbore weakens, the other two fractures receive a comparable portion of the injected fluid. Eventually, as crack #2 evolves, the flow rate in cracks #1

and #3 decreases to a very small portion of the total injection rate and crack #2 takes most of the injected fluid. The small jumps due to fracture propagation are also seen in flow rate curves. When crack #2 stops propagation, more fluid is directed to the other two crack. Figure 3.11 shows that the fluid lost by crack #2 is gained by the other two cracks. When pressure builds up, crack #2 recovers the required propagation flow rate and propagates again.

Figure 3.12 depicts the results of the flow partitioning algorithm for two different time discretizations. The model with smaller time increments ($\Delta t = 0.005\ s$) shows multiple stages of fracture propagation and stoppage, whereas the model with larger time increments can only capture the propagation stages.

While there seems to be a physical basis for the jumps in flow rates into each crack and the resulting crack paths appear reasonable, it was not possible for this problem to demonstrate strong convergence with decreasing time increments, due to computational cost. Therefore, future research should aim to demonstrate convergence to a greater degree and to further verify the stability of the fluid partitioning algorithm.

3.5.2 Simulation of a Wellbore with Four Hydraulic Fractures

A wellbore with four initial hydraulic fractures as depicted in Figure 3.6b is simulated using the fixed stress HF split. All mechanical and numerical parameters are identical to the three fracture problem presented in Section 3.5.1.

HF trajectories and contours of stress, σ_{xx} and σ_{yy}, for this example are illustrated in Figure 3.13. Due to the symmetry of the problem, cracks #2 and #3 propagate simultane-

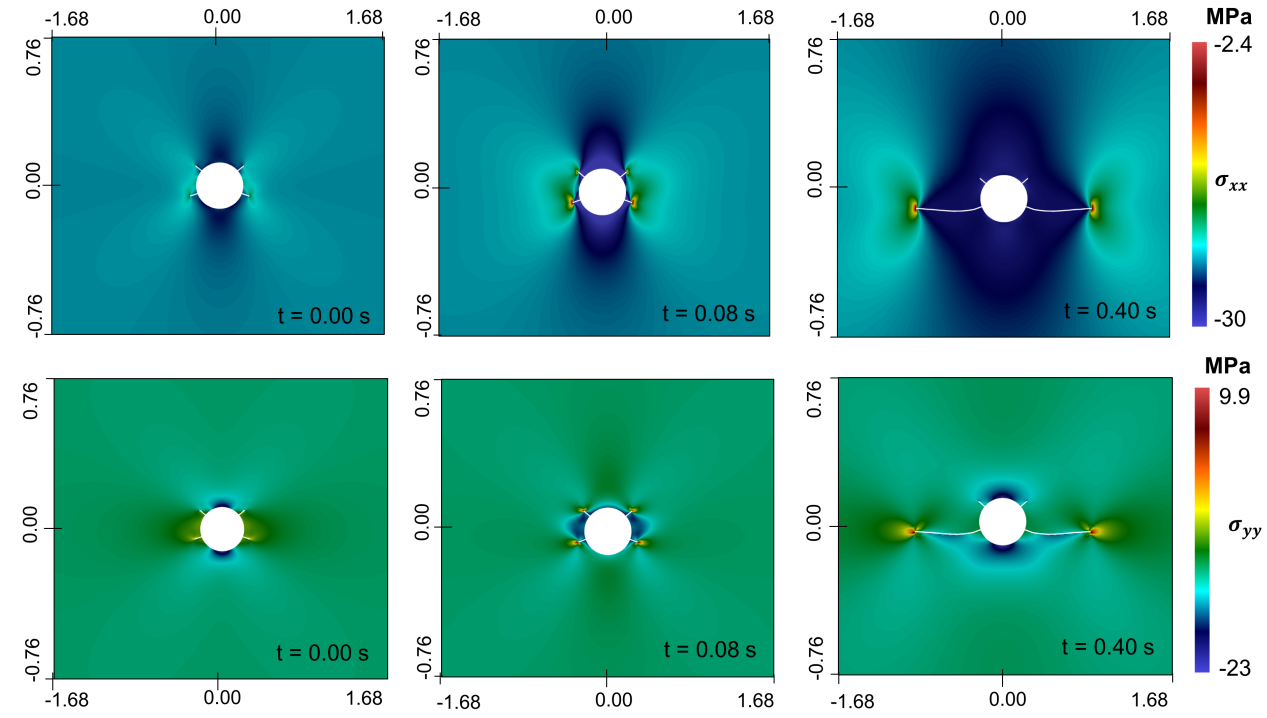

Figure 3.13: Contours of stress, σ_{xx} (top) and σ_{yy} (bottom), around the wellbore

ously when the tensile stress at their tip reaches the tensile strength of the solid. No region with tensile stress concentration is seen around the wellbore in this simulation. Instead, high compressive stress regions are evident near the wellbore where hydraulic fractures are located close to each other.

Figures 3.14 and 3.15, respectively illustrate the change of wellbore pressure and fracture aperture at the wellbore over time. Due to the symmetry of the problem, only apertures of crack #1 and #2 are plotted in Figure 3.15. The trends are similar to those observed in Section 3.5.1, and are as expected.

For the purpose of comparison, the results obtained from a simulation using the fixed

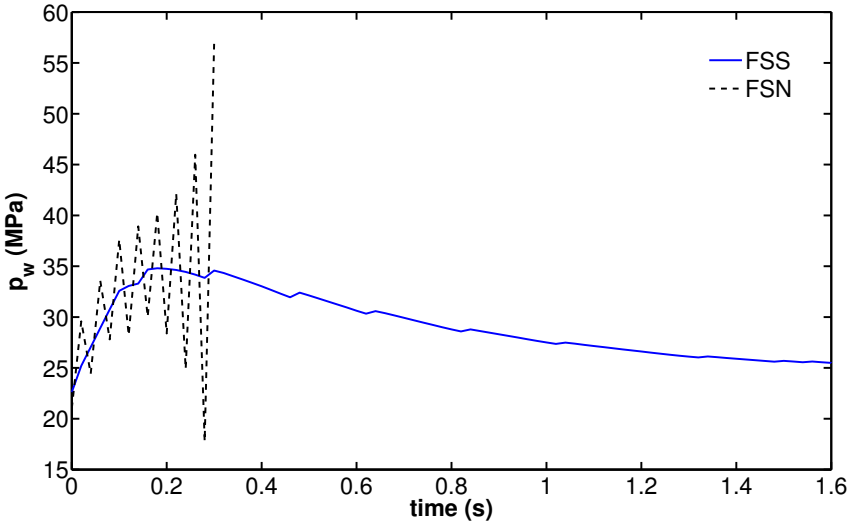

Figure 3.14: Change of wellbore pressure over time estimated by the fixed stress HF split (FSS) and the fixed strain HF split (FSN) using constant time increments, $\Delta t = 0.02\ s$. The fixed strain HF split is interrupted as the global continuity condition has not been met after 100 iterations.

strain HF split are also depicted in Figures 3.14 and 3.15. The fixed strain split exhibits a numerical instability (oscillations) in estimating the fluid pressure and fracture aperture and fails to complete the simulations. Both fracture aperture and fracture pressure results obtained by the fixed strain HF algorithm are oscillatory, but the oscillations are more intense in the estimation of wellbore pressure. The fixed stress HF split, however, is stable and, as shown in Section 3.5.1, converge to the results of the fully coupled model.

Figure 3.16 illustrated the partitioning of fluid between the four fractures. The two propagating fractures, cracks #2 and #3 take most of the fluid injected to the wellbore. The figure demonstrates the efficiency of the automatic partitioning algorithm in this application.

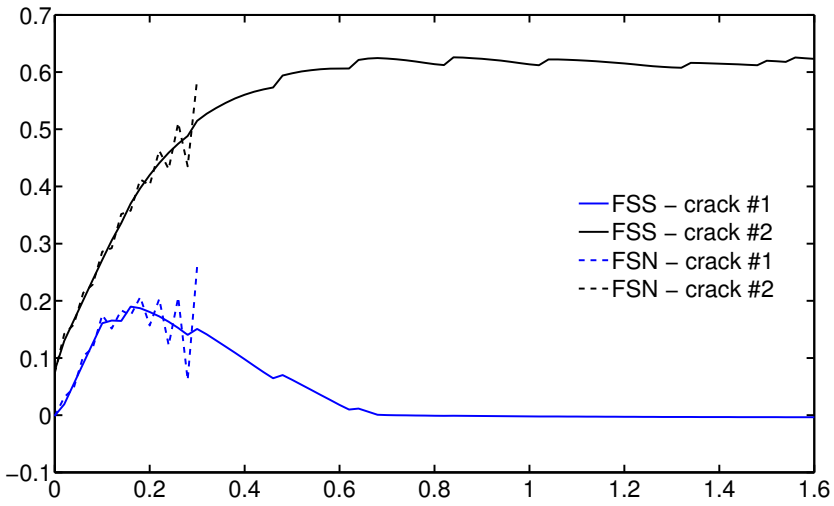

Figure 3.15: Change of wellbore pressure over time estimated by the fixed stress HF split (FSS) and the fixed strain HF split (FSN) using constant time increments, $\Delta t = 0.02\ s$. The fixed strain HF split is interrupted as the global continuity condition has not been met after 100 iterations.

3.6 Conclusions

In this chapter, a new iterative coupling algorithm was developed for the simulation of hydraulic fractures in impermeable media. The new algorithm was derived based on the analogy of the fixed stress split in poromehcanics, and was compared with the fully coupled model. The $W \rightarrow P$ scheme used in HF simulation was found to be analogous to the fixed strain algorithm in poromechanics (known to be conditionally stable) and, therefore, named the fixed strain HF split in this research.

The fixed stress HF split was developed in the extended finite element framework. The algorithm was used to simulate the propagation of multiple hydraulic fractures from a wellbore. It was demonstrated that the fixed stress HF split can successfully model

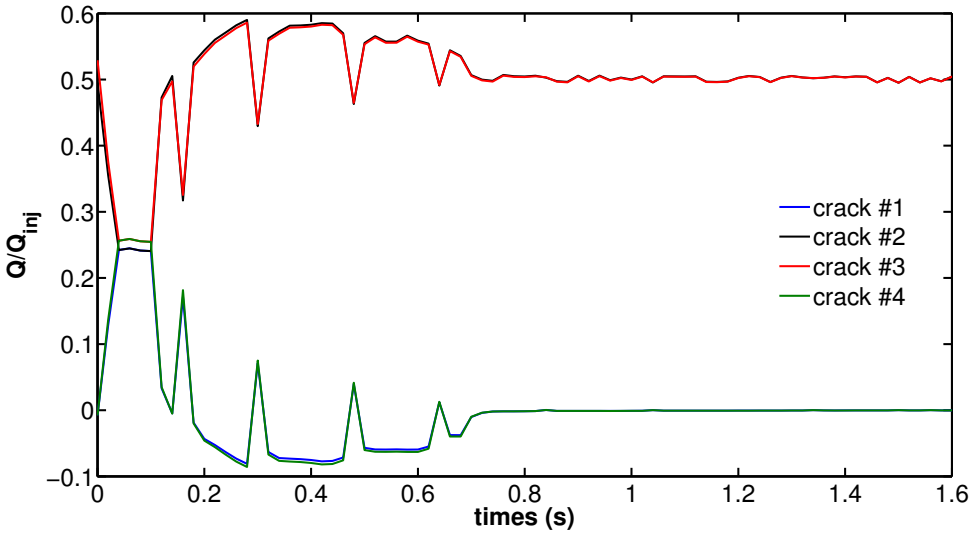

Figure 3.16: Partitioning of the injected fluid, $Q_{inj} = 2 \times 10^{-4} m^3/s \cdot m$

nonplanar hydraulic fracture trajectories. The numerical examples also demonstrated that the solution of the fixed stress HF split converges to the solution of the fully coupled model. The new algorithm also successfully captured the declining wellbore pressure and fracture aperture curves. The fixed strain HF split ($W \rightarrow P$) was shown to exhibit numerical instability and, therefore failed to successfully complete the simulations.

An iterative automatic fluid partitioning algorithm was also presented in this chapter. The algorithm was developed based on the enforcement of the global conservation of mass, and was shown, through numerical examples, to work efficiently with the fully coupled model and the fixed stress HF split.

Chapter 4

Dynamic Hydraulic Stimulation of a Wellbore

4.1 Introduction

Large amplitude and high rate fluid pressure pulses have been shown to be an effective means of stimulating a wellbore [132]. Application of this technology has been particularly effective in increasing production rates of heavy oil wells by enhancing the permeability of the formation around the wellbore [132, 144]. While hydraulic fracture (HF) simulation has become a well-developed topic, especially since the large scale deployment of hydraulic fracturing from horizontal wells [78, 68, 57, 120, 50]; the vast majority of the simulators developed have assumed quasi-static conditions for the rock mass. The assumption of a quasi-static rock mass is well-suited for traditional hydraulic fracturing operations; however, this assumption is not valid for stimulation by high-rate pressure pulsing [132]. A wellbore may be dynamically stimulated by other high-rate processes, such as impact, explosion, combustion, etc., in which loads are applied rapidly. High-rate loading can trigger fracture patterns which are different from the normal patterns observed in regular hydraulic fracturing [62, 144]. In a normal hydraulic fracturing process, fractures tend to propagate in the direction of maximum local stress. In most cases only one set of dominant fractures can overcome the stress barrier and propagate away from the wellbore. This effect limits the permeability enhancement that can be achieved from hydraulic fracture propagation. Dynamic stimulation can stimulate the propagation of fractures oriented in multiple directions from the wellbore [144].

Dynamic stimulation, if not properly controlled, can result in a damaged wellbore, decreased permeability, or the creation of a stress cage around the wellbore and, therefore, negatively affect production [144]. The stimulation technology used in practice for dynamic

wellbore stimulation control the dynamic loading through restricting the peak pressure applied to the wellbore (i.e., the amplitude of the pulse) and the rate by which kinetic energy is transferred to the system (i.e., the period of the pulse) [144].

In the context of computer simulation, efforts in modeling hydraulically induced fractures has been mainly limited to quasi-static models. The quasi-static hydraulic fracture simulation have been performed with various numerical methods including the finite element method [120, 149, 19, 123, 124], the boundary element method [128, 147, 81, 51, 143, 155, 153, 116, 24], the extended finite element method [52, 53, 54, 78, 68, 40, 101, 100, 99, 119, 88, 61], and phase-field method [93, 90, 89, 83, 145, 121]. Other models have been performed which considered hydraulic fracture simulation using non-local damage/plasticity [94, 125, 126], interaction of hydraulic fractures with the natural fracture network [68, 50, 44], and fracture branching [122, 84, 41]. Analytical and semi-analytical HF models have been exclusively focused on quasi-static analysis [48, 38, 46, 45]

There are relatively few major contributions on the dynamic simulation of hydraulically induced fractures presented in the literature. White et al. [144] studied dynamic initiation and propagation of fractures due to the combustion and explosion loading using a discrete fracture network (DFN) model. Dynamic simulation of hydraulic fractures in porous media was first presented in an article by Khoei et al. [67]. They presented an XFEM model for the dynamic propagation of cohesive hydraulic fractures in a saturated porous medium under constant injection rates, in which dynamics effects were limited to only the start up effect of fluid injection and did not evaluate the effect of high rate pulsing. Cao et al. [18] investigated the propagation patterns in lab-scale specimens loaded mechanically and hydraulically, in which wave reflections cause the non-steady propagation of a single edge

crack in a saturated porous medium. He and Duan [62] investigated the dynamic stress perturbation induced by hydraulic fracturing and provided a comparison with quasi-static stress change under plane strain conditions, in which they demonstrated that the stress perturbation from inertia effects can exceed that of a static model. It is worth mentioning that all the aforementioned studies have accounted for inertial effects only in the mechanical subproblem, but have neglected inertial effect in the fluid.

The analysis of the dynamics of porous medium, in which the inertial effect of both the fluid and the matrix are considered, share many similarities with dynamic simulation of hydraulic fracturing. The notable theories are the traditional extension of Biot's theory and the more thermodynamically rigorous theory by Spanos [32]. The application of the more rigorous theory of Spanos has been limited, due in part to its complexity; examples include [132, 118]. The application of dynamic porous media models based on the simple extension of Biot's theory are mainly limited to the simulation of acoustic wave emissions in porous media (e.g.[75, 74]); however, such models do not simulate fluid flow inside the fractures nor fracture propagation in porous media.

Dynamic stimulation using pressure pulsing results in multiple loading and unloading stages during which hydraulic fractures undergo cycles of opening, closing, and propagation. Based upon the stimulation frequency and the mechanical characteristics of the formation (e.g., permeability and stiffness), the response of the fracture to the applied stimulation will vary. The response determined by the dynamic compliance of the formation, the fluid viscosity, and leak-off rate, and fracture propagation. Dynamic HF models are quite different than quasi-static models. In quasi-static models, the work done by the fluid pressure is stored as internal energy or dissipated by the creation of new frac-

ture surfaces or dissipated by viscous damping mechanisms [35]. From quasi-static HF models the concepts of toughness dominated, viscous dominated, and leak-off dominated fracture propagation have been developed [35]. In a dynamic model, the work done by the fluid pressure is transformed into internal energy, but also kinetic energy; energy is still dissipated by fracture propagation and viscous damping, but energy is also transported away from the process zone by wave propagation. The conversion of kinetic energy into internal energy as waves propagate induces a complex time dependence into the competition between toughness dominated, viscous dominated, and leak-off dominated fracture propagation mechanisms.

The purpose of this chapter is to investigate the response of a hydraulic fractures to dynamic stimulation by cyclic pulsing in the context of a plane strain model of a pressurized wellbore and a bi-wing fracture. The propagation of pressure and inertia driven fractures from a wellbore and the behavior of the induced fractures are also investigated. Finally, the unique wave emission patterns corresponding to different stages of wellbore and fracture response are discussed. The mathematical model used in this study takes into account the inertial effects in the solid subproblem but neglects the inertial terms in the transient viscous fluid flow model. A one-dimensional leak-off model is implemented to account for fluid leak-off from fractures into the formation. We use a fully coupled hydro-elastodynamic solver and employ the extended finite element method to simulate fracture propagation in the solid. The standard finite element method is employed to model the transient viscous flow within fractures. A cohesive zone model, with non-recoverable damage, is used to simulate quasi-brittle fracture propagation, and a linear contact model is used to capture fracture closure.

The mathematical formulation for the simulation of fracture growth from a perforated wellbore is discussed in Section 4.2. This section includes a description of the governing equations of the solid rock mass and fracture fluid, as well as the spatial and temporal discretization and implicit solution strategy for the coupled system. Numerical results for the dynamic stimulation of a wellbore using pressure pulses are provided in Section 4.3. The results show the effect of the permeability and porosity of the formation on the resulting fracture geometry during propagation and the closure mechanisms observed after the pressure pulse ends. Major wave emission patterns generated during the stimulation of the wellbore and fractures are discussed.

4.2 Mathematical Formulation

In this section, the mathematical formulation for the coupled hydro-elastodynamic problem is explained. Subsequently, the numerical approach and the discrete form of the mathematical model are discussed. Lastly, the strategy for solving the coupled problem is presented.

4.2.1 Equation of Motion

The solid domain of the problem, $\Omega_s \in \mathbb{R}^2$, is shown in Figure 4.1(a). The solid domain is bounded by its boundary, $\Gamma_s = \Gamma_t \cup \Gamma_c \cup \Gamma_u$, in which Γ_t is the Neumann boundary where external traction is prescribed, Γ_c is the internal fracture boundary where the traction due to fluid pressure is applied, and Γ_u is the Dirichlet boundary where displacement or its temporal derivatives (velocity or acceleration) are prescribed. The sets of boundaries Γ_t,

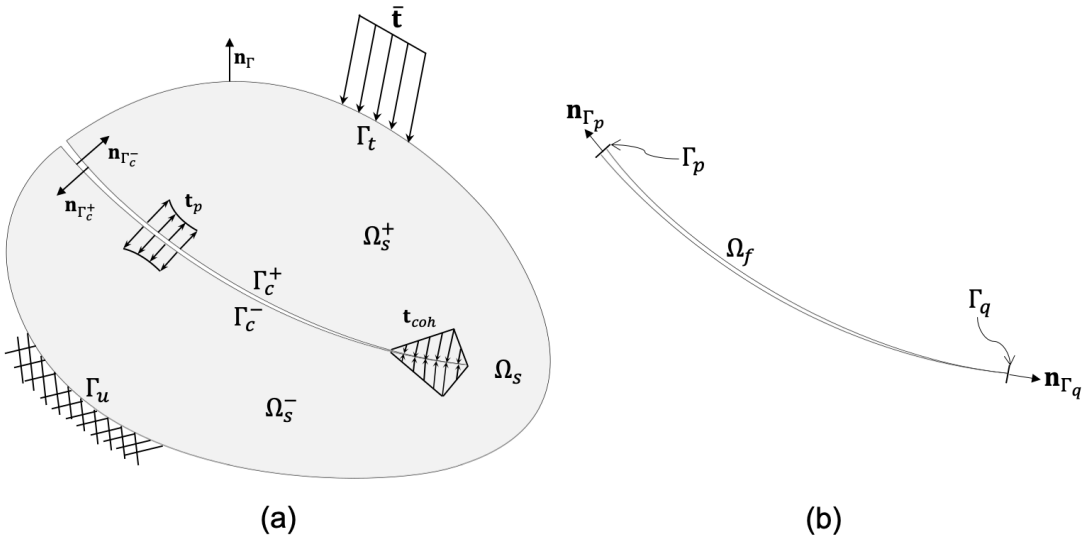

Figure 4.1: Schematic of the domains of the problem: (a) solid domain and (b) fluid domain

Γ_c, and Γ_u must be chosen such that $(\Gamma_t \cup \Gamma_c) \cap \Gamma_u = \varnothing$.

The mechanical response of the solid domain at point $\mathbf{x} \in \Omega_s$ and time $t > 0$ is governed by conservation of linear momentum, which in the absence of body forces, reads

$$\rho_s \ddot{\mathbf{u}}(\mathbf{x}, t) = \boldsymbol{\nabla} \cdot \boldsymbol{\sigma}(\mathbf{x}, t) \tag{4.1}$$

in which ρ_s is the mass density of the solid, $\ddot{\mathbf{u}}$ is the second temporal derivative of the solid displacements vector $\mathbf{u}$, $\boldsymbol{\sigma}$ is the Cauchy stress tensor.

The stress in the solid domain is related to the strain in the domain, $\boldsymbol{\varepsilon}$, through

$$\boldsymbol{\sigma} - \boldsymbol{\sigma}_0 = \mathbb{C} : \boldsymbol{\varepsilon} \tag{4.2}$$

where $\mathbb{C}$ is the fourth order elasticity tensor and $\boldsymbol{\sigma}_0$ is the initial state of stress in the

domain (i.e., *in situ* stress field).

A schematic of the traction separation law for the fracture contact-cohesive law is illustrated in Figure 4.2. Using a cohesive fracture model similar to the one used in Chapter 2 [49] and a lateral contact model, the interface traction-separation law for point $\mathbf{x} \in \Gamma_c$ located on the fracture boundary of the solid domain is given by

$$t^{cr}(w, w_{his}) = \begin{cases} \frac{1}{w_w} f_u w & w < 0 \\ \frac{(1-D)}{w_w} f_u w & 0 < w \leq w_w \\ \frac{(1-D)}{w_w - w_c} f_u \left(w - w_c\right) & w_w < w_{his} < w < w_c \\ \frac{(1-D)(1-w_c)}{w_{his}(w_w - w_c)} f_u w & w_w < w < w_{his} < w_c \\ 0 & w_c < w \end{cases} \tag{4.3}$$

Here, $w = w(\mathbf{x}, t)$ is the fracture aperture at point $\mathbf{x}$ and time t, the weakening aperture of the cohesive model is represented by w_w, and $w_c = 2G_c/f_u$ is the critical aperture of the cohesive model with G_c being the fracture energy of the solid. The maximum aperture experienced in the history of point $\mathbf{x}$ is denoted by $w_{his} = w_{his}(\mathbf{x})$, and D is the non-recoverable damage flag defined as

$$D = \begin{cases} 0 & w_{his} \leq w_c \\ 1 & w_{his} > w_c \end{cases} \tag{4.4}$$

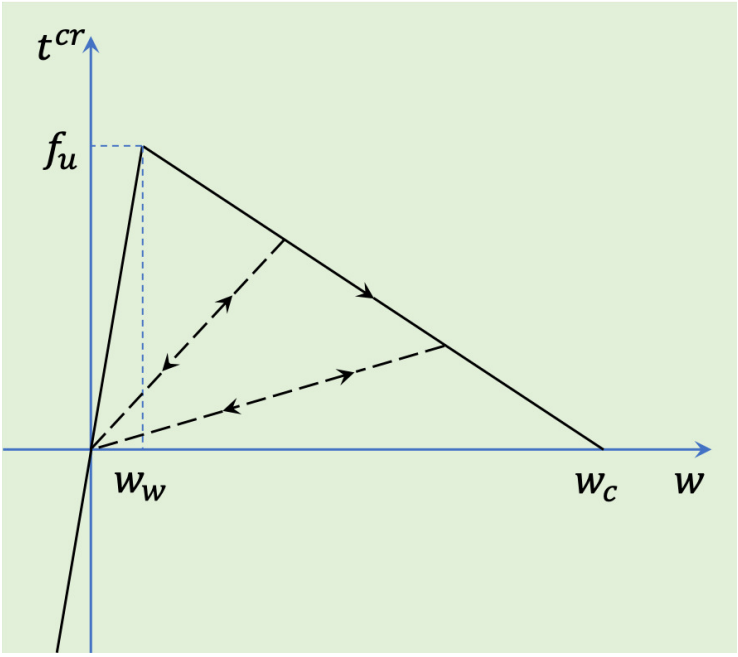

Figure 4.2: Schematic of the traction separation law on the fracture boundary

The boundary conditions on the solid model are

$$\begin{aligned} \mathbf{u} &= \bar{\mathbf{u}} \quad \text{on } \Gamma_u \\ \boldsymbol{\sigma} \cdot \mathbf{n}_{\Gamma_t} &= \bar{\mathbf{t}} \quad \text{on } \Gamma_t \\ \boldsymbol{\sigma} \cdot \mathbf{n}_{\Gamma_c} &= (t^{cr}\mathbf{I} - p\mathbf{I} - \boldsymbol{\sigma}_0) \cdot \mathbf{n}_{\Gamma_c} \quad \text{on } \Gamma_c \end{aligned} \tag{4.5}$$

in which $\mathbf{n}_{\Gamma_t}$ and $\mathbf{n}_{\Gamma_c}$ denote the unit outward normal vector to the traction boundary, Γ_t, and the fracture boundary, Γ_c, respectively.

4.2.2 Continuity Equation

The fluid domain of the problem, $\Omega_f \in \mathbb{R}$, is illustrated in Figure 4.1(b). The domain, Ω_f, is bounded by Dirichlet boundary, Γ_p, on which fluid pressure is prescribed, and Neumann boundary, Γ_q, over which fluid mass flux is prescribed.

Fluid flow within the fractures is governed by conservation of mass. Assuming an incompressible flow of a Newtonian fluid within the fractures, conservation of mass at point $s \in \Omega_f$ and time $t > 0$ is

$$\frac{\partial w(s,t)}{\partial t} + \frac{\partial}{\partial s} q(s,t) + v_l(s,t) = 0 \tag{4.6}$$

in which w is the fracture aperture, q is the fluid volume flux along the fracture, and v_l is the velocity by which fluid leaks off from the fracture into the formation in the direction normal to the fracture.

Neglecting the fluid inertial effects and using the cubic law to define the volume flux, q, the conservation of mass equation for point $s \in \Omega_f$ of the fluid domain at time $t > t_0$ takes the form

$$\frac{\partial w(s,t)}{\partial t} - \frac{\partial}{\partial s}\left[\frac{w^3}{12\mu}\frac{\partial}{\partial s} p(s,t)\right] + \frac{2\bar{c}_l}{\sqrt{t - t_0(s)}}\left[p(s,t) - p_\infty\right] = 0 \tag{4.7}$$

in which μ is the dynamic viscosity of the fluid, $\bar{c}_l$ is the leak-off coefficient, t_0 denotes the time at which leak-off from point s starts (taken as the time of fracture initiation at point s), and p_∞ is the original (far field) formation pressure.

The leak-off coefficient, $\bar{c}_l$ is defined as [64]

$$\bar{c}_l = \sqrt{\frac{k\phi c_t}{\mu\pi}} \tag{4.8}$$

in which k is the permeability of the formation, ϕ is the formation porosity, and c_t is the bulk compressibility of the porous formation calculated from the compressibility of the solid matrix, c_s, and the compressibility of the fluid, c_f, as $c_t = c_s + c_f$.

Carter leak-off model assumes that fluid leak-off from each point, $s \in \Omega_f$, along the fracture is one-dimensional and that the leak-off velocity vector is perpendicular to the fracture. The leak-off formulation is derived also under the assumption of uniform pressure distribution along the fracture [64]. Generally, the validity of the linear leak-off model is known to be a function of the ratio of the fracture propagation rate to the rate of fluid leak-off from the fracture. The model provides a good estimate of the fluid leak-off when the rate of hydraulic fracture propagation is considerably larger than the rate by which fluid leaks off from the fracture [140]. Therefore, when hydraulic fractures are propagating under low rates (i.e., quasi-static propagation), the linear leak-off model yields a reasonable estimate of the fluid leak-off only in low permeability formations, in which diffusion rates are small. Carter leak-off model was shown to underestimate the leak-off rate in moderate to high permeability formations under quasi-static propagation conditions [127, 76]. When hydraulic fracture propagation rates are high (i.e., dynamic propagation), the range of validity of the linear leak-off model can be further extended to higher permeability formations with higher leak-off rates. In the present study, dynamic wellbore stimulation generates rapidly propagating fractures; therefore, Carter leak-off model can still be considered valid over a wide range of formation permeability.

When the ratio of propagation to leak-off rates is low (Carter leak-off is not valid), other models such as radial [139] and pseudo-radial [76] leak-off models are employed. Two-dimensional leak-off models that can be applied to both early and late time leak-off are also available in the literature [55, 127, 140].

Using only one leak-off term, as used in (4.7), is a simple way of incorporating fluid leak-off in the continuity equation. While similar single-term leak-off has been used in many researches [2, 64, 140], a more robust way to account for leak-off in the continuity equation is in the form of a convolution integral. The leak-off term, then, is an integral over time of a time-dependent kernel similar to the leak-off term in (4.7). The convolution integral form, however, requires the storage of fracture pressure time history, and therefore, may not be the most effective and practical application of the leak-off model.

Finally, the boundary conditions of the fluid model are given by

$$\begin{aligned} p &= \bar{p} \quad \text{on } \Gamma_p \\ q &= \bar{q} = -\left(\frac{w^3}{12\mu}\frac{\partial}{\partial s}p\right) n_q(s) \quad \text{on } \Gamma_q \end{aligned} \tag{4.9}$$

in which $n_q(s=0) = -1$ and $n_q(s=L_f) = 1$ and L_f is the fracture length.

4.2.3 Numerical Model and Solution Strategy

We use an XFEM framework to develop the numerical model for the fractured solid, and a standard FEM framework for the fluid numerical model. The FEM/XFEM formulations

use the weak form of the governing equations to come up with the discrete equations for the hydro-elastodynamic problem discussed above.

Weak Form of the Governing Equations

The weak forms of the governing equations, (4.1) and (4.7) are:

$$\begin{aligned}&\int_{\Omega_s} \delta\mathbf{u}\cdot\rho_s\ddot{\mathbf{u}}d\Omega + \int_{\Omega_s} \boldsymbol{\nabla}\delta\mathbf{u}\colon\mathbb{C}\colon\boldsymbol{\varepsilon}d\Omega - \int_{\Gamma_t}\delta\mathbf{u}\cdot\bar{\mathbf{t}}d\Gamma \\ &+\int_{\Gamma_c}[\![\delta\mathbf{u}]\!]\cdot(t^{cr}\mathbf{I}-p\mathbf{I}-\boldsymbol{\sigma}_0)\cdot\mathbf{n}_{\Gamma_c}d\Gamma = \mathbf{0}\end{aligned} \tag{4.10}$$

$$\begin{aligned}&\int_{\Omega_f}\delta p\frac{\partial w}{\partial t}d\Omega - \int_{\Omega_f}\frac{\partial}{\partial s}\delta p\left(\frac{w^3}{12\mu}\right)\frac{\partial}{\partial s}pd\Omega + \int_{\Gamma_q}\delta p\bar{q}d\Omega \\ &+\int_{\Omega_f}\delta p\frac{2\bar{c}_l}{\sqrt{t-t_0}}\left(p-p_\infty\right)d\Omega = 0\end{aligned} \tag{4.11}$$

in which $\delta\mathbf{u}\in U_0$ and $\delta p\in P_0$ are respectively the displacement and pressure test functions. The sets U_0 and P_0 denote the spaces of admissible displacement and pressure test functions, respectively. For more details the XFEM discretization and dynamic fracture simulation with XFEM, the reader is referred to [158].

Space and Time Domain Discretizations

Solid displacement, $\mathbf{u}(\mathbf{x},t)$ and fluid pressure $p(s,t)$ are respectively approximated as

$$\begin{aligned}\mathbf{u}_h(\mathbf{x},t) &= \sum_{\forall I\in S^u} N_I(\mathbf{x}) d_I^u(t) \\ &\quad + \sum_{\forall J\in S^a} N_J(\mathbf{x})\left[H_c(\mathbf{x}) - H_c(\mathbf{x}_J)\right] d_J^a(t) \equiv \mathbf{N}(\mathbf{x})\mathbf{d}(t) \\ p_h(s,t) &= \sum_{\forall I\in S^p} \psi_I(s) p_I(t) \equiv \boldsymbol{\psi}(s)\mathbf{p}(t)\end{aligned} \tag{4.12}$$

in which N_I and ψ_I are respectively the shape functions for solid displacement and fluid pressure, d_I^u and p_I are the standard degrees of freedom for displacement and pressure, d_a^u represents the enriched degrees of freedom for solid displacement, and H_c denotes the discontinuous enrichment function. Moreover, the set of all nodes of the solid mesh, the set of all nodes of the fluid mesh and the set of enriched nodes of the solid mesh are denoted by S^u, S^a, and S^p respectively (see Figure 4.3). In the matrix form, matrices $\mathbf{N}(\mathbf{x})$ and $\boldsymbol{\psi}(s)$ are respectively the shape function matrices of displacement and pressure approximations. The degrees of freedom matrices of displacement and pressure are respectively denoted by $\mathbf{d}(t)$ and $\mathbf{p}(t)$.

Using a similar approximation, the displacement jump across the fracture is approximated by

$$[\![\mathbf{u}_h(\mathbf{x},t)]\!] = [\![\mathbf{N}(\mathbf{x})]\!]\mathbf{d}(t) \tag{4.13}$$

Fracture aperture is defined as the normal component of the jump with respect to the

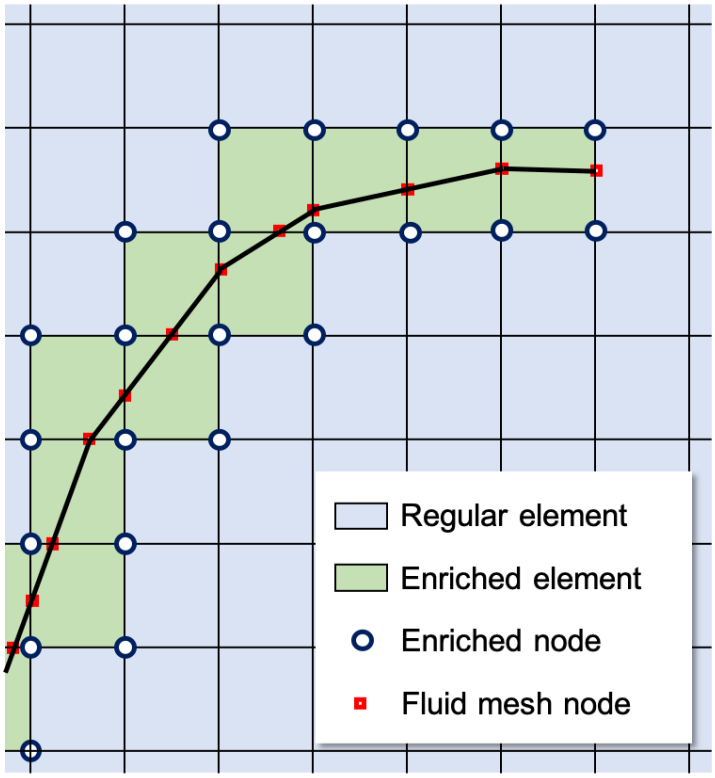

Figure 4.3: Schematic of different node sets in the numerical mesh

fracture and is approximated as $w_h(\mathbf{x},t) = \mathbf{n}_{\Gamma_c}^\top [\![\mathbf{N}(\mathbf{x})]\!] \mathbf{d}(t)$.

The first and second temporal derivatives of displacement at time $t = t_n$ are approximated as

$$\begin{aligned} \dot{\mathbf{d}}^n &= \dot{\mathbf{d}}(t = t_n) = \frac{1}{\Delta t_n}\left(\mathbf{d}^n - \mathbf{d}^{n-1}\right) \\ \ddot{\mathbf{d}}^n &= \ddot{\mathbf{d}}(t = t_n) = \frac{1}{\Delta t_n}\left(\dot{\mathbf{d}}^n - \dot{\mathbf{d}}^{n-1}\right) \end{aligned} \tag{4.14}$$

where Δt_n is the time increment.

Coupled Problem

Substituting the approximations, (4.12) and (4.13), into the governing equations, (4.1) and (4.7), the fully coupled hydro-elastodynamic problem is described by the following nonlinear system of equations:

$$\begin{aligned} \mathbf{R}_u(\mathbf{u},\mathbf{p}) &= \int_{\Omega_s} \mathbf{N}^\top \rho_s \mathbf{N} d\Omega \ddot{\mathbf{d}} + \int_{\Omega_s} \mathbf{B}^\top \mathbf{C}\mathbf{B} d\Omega \mathbf{d} - \int_{\Gamma_t} \mathbf{N}^\top \bar{\mathbf{t}} d\Gamma \\ &\quad + \int_{\Gamma_c} [\![\mathbf{N}]\!]^\top \left(t^{cr}\mathbf{n}_{\Gamma_c} - p\mathbf{n}_{\Gamma_c} - \mathbf{t}_0^c\right) d\Gamma \\ \mathbf{R}_p(\mathbf{u},\mathbf{p}) &= \int_{\Omega_f} \boldsymbol{\psi}^\top \mathbf{n}_{\Gamma_c}^\top [\![\mathbf{N}]\!] d\Omega \dot{\mathbf{d}} - \int_{\Omega_f} \boldsymbol{\nabla}\boldsymbol{\psi}^\top \left(\frac{w^3}{12\mu}\right) \boldsymbol{\nabla}\boldsymbol{\psi} d\Omega \mathbf{p} \\ &\quad + \int_{\Omega_f} \boldsymbol{\psi}^\top \frac{2\bar{c}_l}{\sqrt{t - t_0}} \left(p - p_\infty\right) d\Omega + \boldsymbol{\psi}|_{\Gamma_q} \bar{q} \end{aligned} \tag{4.15}$$

where $\mathbf{B}$ and $\boldsymbol{\nabla}\boldsymbol{\psi}$ are the matrices of space derivatives of displacement and pressure shape functions respectively, $\mathbf{C}$ is the matrix representation of the fourth order elasticity tensor, and $\mathbf{t}_0^c = \boldsymbol{\sigma}_0 \cdot \mathbf{n}_{\Gamma_c}$.

The Newton-Raphson iterative scheme is used to solve the nonlinear system (4.15), after substituting (4.14) into (4.15).

Let the vector of total unknowns of the coupled system at iteration i of time $t = t_n$ and its increment be denoted respectively by $\mathbf{X}_i^n = \{\mathbf{d}_i^n, \mathbf{p}_i^n\}^\top$ and $\Delta\mathbf{X}_i^n = \{\Delta\mathbf{d}_i^n, \Delta\mathbf{p}_i^n\}^\top$. Let also the residual of the coupled system be $\mathbf{R}_i^n = \left\{\mathbf{R}_{u_i}^n, \mathbf{R}_{p_i}^n\right\}^\top$. The solution of (4.15) at iteration $i+1$ of time $t = t_n$ is calculated by $\mathbf{X}_{i+1}^n = \mathbf{X}_i^n + \Delta\mathbf{X}_i^n$ where $\Delta\mathbf{X}_i^n$ is the solution of the linearized system

$$\mathbf{J}_i^n \Delta\mathbf{X}_i^n + \mathbf{R}_i^n = \mathbf{0} \tag{4.16}$$

The terms of the Jacobian matrix, $\mathbf{J}_i^n$, are defined as

$$\begin{aligned}
\mathbf{J}_{uu} =& \frac{1}{\Delta t^2}\int_{\Omega_s} \mathbf{N}^\top \rho_s \mathbf{N} d\Omega + \int_{\Omega_s} \mathbf{B}^\top \mathbf{C}\mathbf{B} d\Omega \\
&+ \int_{\Gamma_c} [\![\mathbf{N}]\!]^\top \mathbf{n}_{\Gamma_c} \frac{\partial t^{cr}}{\partial w} \mathbf{n}_{\Gamma_c}^\top [\![\mathbf{N}]\!] d\Gamma \\
\mathbf{J}_{up} =& -\int_{\Gamma_c} [\![\mathbf{N}]\!]^\top \mathbf{n}_{\Gamma_c} \boldsymbol{\psi} d\Gamma \\
\mathbf{J}_{pu} =& \frac{1}{\Delta t}\int_{\Gamma_c} \boldsymbol{\psi}^\top \mathbf{n}_{\Gamma_c}^\top [\![\mathbf{N}]\!] d\Gamma - \int_{\Omega_f} \boldsymbol{\nabla}\boldsymbol{\psi}^\top \frac{\partial}{\partial s} p \left(\frac{w^2}{4\mu}\right) \mathbf{n}_{\Gamma_c}^\top [\![\mathbf{N}]\!] d\Omega \\
\mathbf{J}_{pp} =& -\int_{\Omega_f} \boldsymbol{\nabla}\boldsymbol{\psi}^\top \left(\frac{w^3}{12\mu}\right) \boldsymbol{\nabla}\boldsymbol{\psi} d\Omega + \int_{\Omega_f} \boldsymbol{\psi}^\top \frac{2\bar{c}_l}{\sqrt{t - t_0}} \boldsymbol{\psi} d\Omega
\end{aligned} \tag{4.17}$$

4.3 Dynamic Stimulation of a Wellbore

In this section, we study the numerical simulation for the dynamic stimulation of a vertical well containing two initial 4 cm fractures. Stimulation is assumed to create a bi-wing vertical fracture, which is modeled using a plane-strain assumption, as depicted in Figure 4.4. Stimulation occurs at an average depth of 2400 m. The wellbore diameter is $D_w = 2R_w = 0.24\ m\ (\simeq 9.625\ in)$. The sandstone reservoir has properties given in Table 4.1. Fluid pressure in the reservoir before injection is assumed to be equal to the hydro-static pressure. The stress regime is assumed to be a normal faulting regime (i.e., $\sigma_{max} = \sigma_v$) with the components of the *in situ* stress field being $\sigma_v = 55\ MPa$, $\sigma_h = 40\ MPa$, and $\sigma_H = 50MPa$. Hence, vertical hydraulic fractures are expected to initiate and propagate in the formation. σ_h is assumed to act parallel to the y-axis of the simulated domain. Simulations are carried out for a unit thickness of the reservoir.

The mechanical properties of sandstone can vary depending upon its porosity, clay content, and other components. Chang et al. [21] provided a comprehensive discussion of published correlations between the material properties of sandstone and its porosity. Nonetheless, using the presented correlations to estimate all the material properties required in this study was not feasible. For example, for properties such as fracture toughness, multiple correlations would have to be evoked and this lead to unphysical values and unexpected trends. To simplify this study, we have introduced simple linear correlations with porosity, which lead to material properties falling within reasonable bounds, as observed in experiments by Chen et al. [23].

In this study, we consider sandstone with three different sets of mechanical properties as

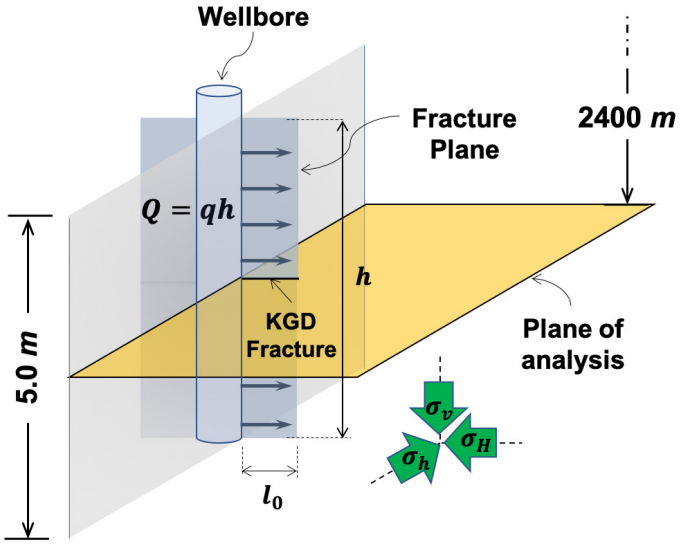

Figure 4.4: Schematic of the reservoir and the plane of analysis

presented in Table 4.2. For all cases, we assumed a Poisson's ratio of $\nu = 0.2$. To estimate other material properties, the porosity of the sandstone is presumed for each case and the mechanical properties are calculated through simple correlations to the porosity. We assumed an exponential relationship between porosity and permeability of the sandstone. Other properties are derived through linear approximations. The correlation used for each mechanical property is presented in Table 4.2.

Simulations are carried out on a 20 m × 20 m domain centered at the wellbore, as illustrated in Figure 4.5. The domain mesh is divided into two subdomains: 1) the near-wellbore region, which is a circular area centered on the wellbore and has a radius of $10R_w$. 2) the far-field region, which covers the rest of the domain from $10R_w$ to the outer boundaries (see Figure 4.5).

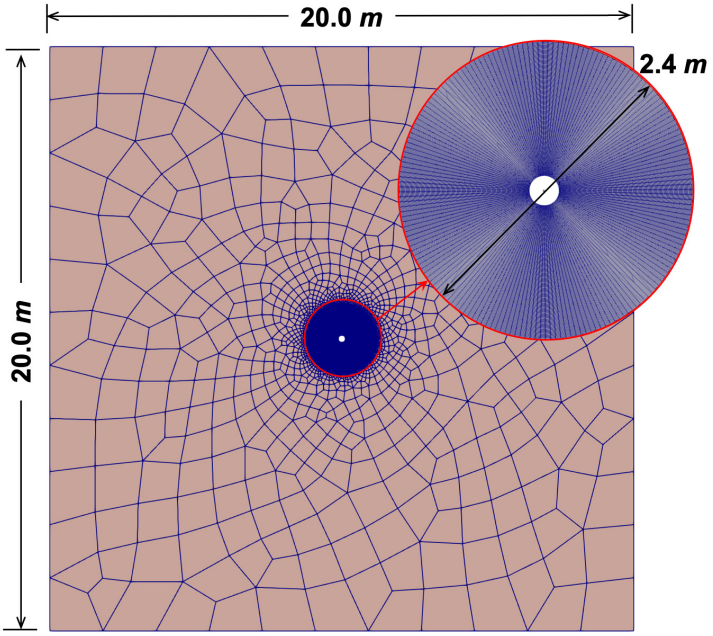

Figure 4.5: Domain of the problem with the corresponding subdomains and the numerical mesh

The near-wellbore region is discretized using a radially structured mesh of bilinear quadrilateral elements. The mesh in the near-wellbore area is finer than that used for the rest of the domain, as hydraulic fracture propagation is expected to occur mainly in this area. An unstructured mesh of the same type of elements is used at the far-field region. The effective mesh size of the near-wellbore region varies from $h_e = 0.013\ m$, at the wellbore, to $h_e = 0.042\ m$ at $10R_w$. The far-field region has an average effective mesh size of $h_e = 0.046\ m$ at $10R_w$ and $h_e = 1.49\ m$ at the outer boundary. We also use fixed time increments of $\Delta t = 2.5 \times 10^{-5}\ s$ in all simulations, which was sufficiently small to obtain convergence.

Table 4.1: Injected fluid characteristics

Material properties	Unit	Water
Mass density (ρ_f)	kg·m^{-3}	1000
Compressibility (c_f)	Pa^{-1}	4.2×10^{-10}
Dynamic viscosity (μ)	Pa·s	0.001

Table 4.2: Material properties of the reservoir

Material property	Unit	Case 1	Case 2	Case 3	Correlation
Porosity (ϕ)	%	15	20	25	-
Permeability (k)	mD	1	10	100	$2\times10^{-3}e^{0.4605\phi}$
Mass density (ρ_s)	kg·m^{-3}	2600	2467	2333	$1000\left[2.6-\frac{0.4}{15}(\phi-15)\right]$
Elasticity modulus (E)	GPa	17	11	5	$35-1.2\phi$
Poisson's ratio (ν)	-	0.2	0.2	0.2	-
Bulk modulus (K_s)	GPa	9.4	6.1	2.7	$\frac{E}{3(1-2\nu)}$
Ultimate tensile strength (f_u)	MPa	4.0	3.33	2.67	$6-\frac{2}{15}\phi$
Fracture energy (G_c)	J·m^{-2}	80	70	60	$110-2\phi$
Fracture toughness (K_{Ic})	MPa·m$^{\frac{1}{2}}$	1.29	1.05	0.79	$10^{-6}\sqrt{\frac{EG_c}{1-\nu^2}}$
Compressibility (c_s)	Pa^{-1}	9×10^{-11}	1.2×10^{-10}	1.8×10^{-10}	$10^{-9}\frac{1}{K_s}$

4.3.1 Stimulation by Pressure Pulses

The wellbore is assumed to contain two initial $4cm$ fracture aligned with the maximum horizontal stress.

Dynamic stimulation of the wellbore is performed through application of a sequence of pressure pulses. Each pulse takes $T_{pulse} = 1\ ms$ and has an amplitude of $p_{max} = 40\ MPa$ over the hydro-static pressure. For the purpose of simplicity, we approximate each pulse with a sinusoidal function with the same amplitude and period as

$$p_w(t) = \begin{cases} p_{max} \sin\left(\frac{\pi t}{T_{pulse}}\right) & 0 < t \leq T_{pulse} \\ 0 & t > T_{pulse} \end{cases} \tag{4.18}$$

A rest period is assumed between each pulse, sufficiently long for the simulation domain to dissipate dynamic effects and return to a static equilibrium state. This is a reasonable assumption consistent with pressure pulsing achieved with current field technologies [144]. Dynamic simulation is carried out for the period of the pulse followed by an addition 1.5 ms of the rest period (total time of 2.5 ms). After this time, the dynamic effect of the wellbore and fracture have sufficiently dissipated and the fracture has returned to a status close to its static equilibrium. No further significant dynamic effects are expected at this stage; hence, a quasi-static steady-state analysis is performed to re-establish a state of equilibrium prior to the next pulse.

Fracture Aperture and Length

Figure 4.6(a) shows the variation of fracture aperture at the wellbore over time during the first cycle of stimulation in each of the three cases. The figure shows that the maximum wellbore aperture observed in time for each case, increases with porosity and permeability. Therefore, case 1 and 3 respectively produce the narrowest and widest hydraulic fractures, respectively. The behavior seen in Figure 4.6(a) can be explained by considering the effect of porosity on the elasticity and bulk moduli of sandstone. Table 4.2 indicates that sandstone formations with higher porosity are generally softer than those with lower porosity. Therefore, under a specific wellbore pressure, fractures in case 3 tend to open wider than fractures in cases 1 and 2, as the formation of 3 shows less resistance to opening.

The shape of the aperture vs time curves in Figure 4.6(a) show a phase lag when compared to the loading pressure pulse. In the early response time ($t < 0.2\ ms$) the lag is due to inertia resistance to fracture opening and in later times ($t > 1.0\ ms$) the lag is due to momentum driven opening. This dynamic response can be contrasted with that of a quasi-static HF model, in which there is no phase lag between injection pressure and wellbore aperture. Figure 4.6(a) also shows non-sinusoidal response to a sinusoidal pressure pulse. It is notable that the time at which the peak wellbore aperture is observed does not correspond to the peak well-bore pressure. This behavior is quite different from that of the quasi-static case in which the peak wellbore aperture and pressure coincide. Lastly, it can be observed in Figure 4.6(a) that the period of the wellbore aperture response is different for each case, with the $\phi = 15\%$ case having the shortest period of response. This action is again different for that of the quasi-static case in which the period of response of

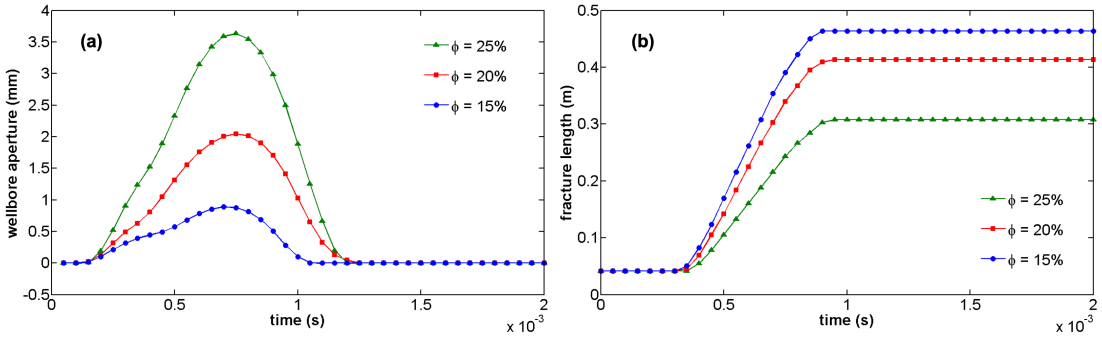

Figure 4.6: Time variation of (a) fracture aperture at the wellbore and (b) fracture length, for the first cycle of stimulation

the wellbore aperture would not depend upon the properties of the formation. Lastly, it is interesting to note that the fractures close smoothly (no bouncing) due to the damping effect of the fluid in the fracture.

The fracture extension in each case is directly affected by the leak-off rate. Figure 4.6(b) illustrates the evolution of hydraulic fractures over time during the first stimulation cycle in each of the three cases. The figure demonstrates that hydraulic fractures in case 1 (smallest porosity and permeability) are the longest. Final fracture length after the first pulse increases in a non-linear way with porosity and permeability. From Figure 4.6(b) is can be observed that no fracture propagation occurs during about the first 40% of the pulse; however, the rate of fracture propagation is nearly constant for the during of the second half of the pulse. The complex competition between energy dissipation mechanisms is also seem in Figure 4.6(b). In case 1, $\phi = 15\%$, fracture energy, tensile strength, and toughness are largest, yet case 1 yields the longest final fracture length. This occurs because permeability and porosity (and also leak-off velocity) are also largest for case 1. Lastly, a comparison of Figure 4.6(a) and (b) illustrates an inverse relationship between maximum

aperture and fracture length.

Figure 4.7 depicts the variation of fracture aperture at the wellbore and fracture length over time. The curves are plotted for three different time increments spanning two orders of magnitude from $\Delta t = 2.5 \times 10^{-5}\ s$ to $\Delta t = 2.5 \times 10^{-7}\ s$. As seen in the figure, the solution of the two smaller time increments are indistinguishable from each other which indicates that the solution is converged for sufficiently small time increments.

The dynamic propagation of hydraulically induced fractures is a complex process affected by several competing time dependent dissipation mechanisms. Therefore, trends other than the ones illustrated in Figure 4.6 may be expected if different material properties corelations are introduced. For instance, if a higher viscosity fluid was considered ($\mu = 1\ Pa \cdot s$), leak-off would be significantly reduced, the trends between porosity and fracture length could be inverted.

Multiple Cyclic Pressure Pulses

Consider a four-cycle pressure pulse stimulation using the pulse given in (4.18). The evolution of fracture length during multiple pulses is depicted in Figure 4.8. The figure shows that the fracture length increment decreases from the first cycle to the fourth cycle. This behavior is expected because (i) more energy is viscously dissipated when flowing a fluid down a longer crack than a shorter crack; (ii) more fluid will leak-off from a longer fracture than a shorter crack, since more fluid is exposed to the permeable formation; and (iii) more fluid is stored in longer fractures. Hence, the increment in fracture decreases with each fixed amplitude pressure pulse.

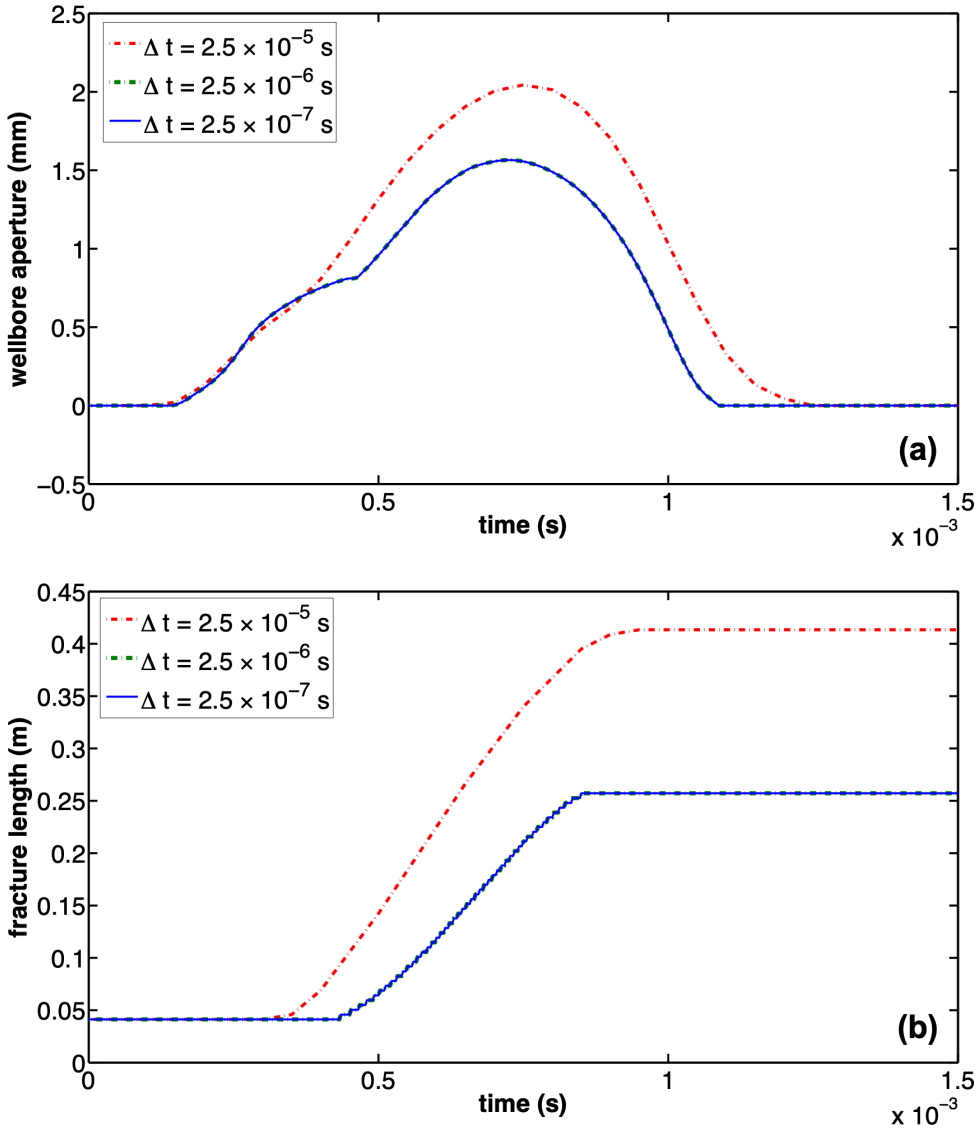

Figure 4.7: Time variation of (a) fracture aperture at the wellbore and (b) fracture length, for the first cycle of stimulation in case 2

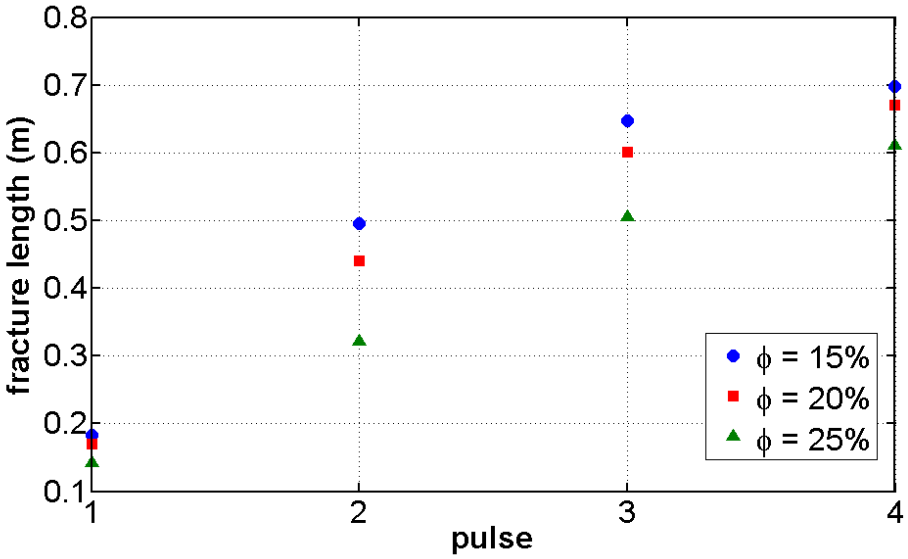

Figure 4.8: Final fracture length at the end of each cycle of stimulation

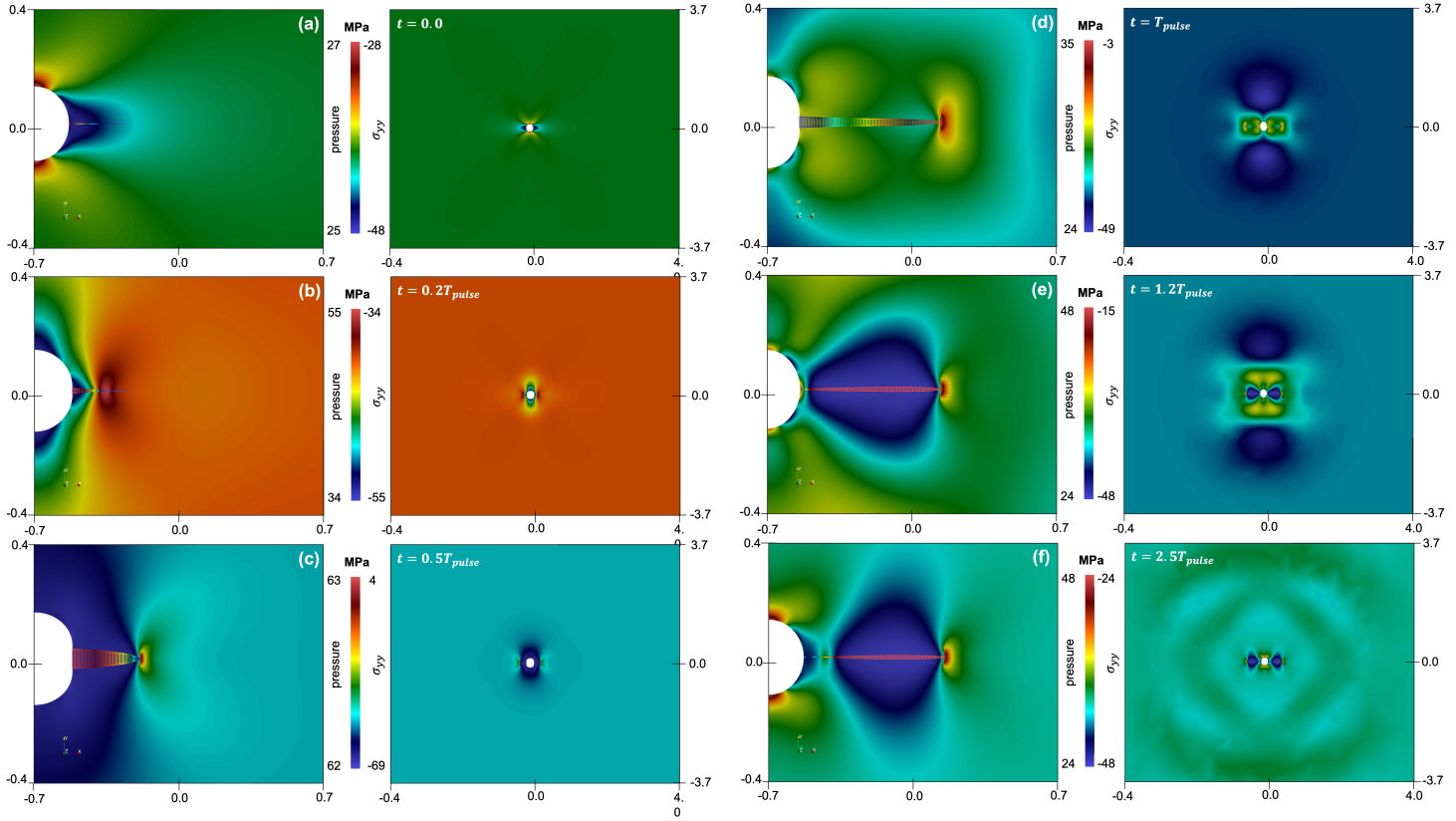

Figure 4.9: Contours of σ_{yy} and fluid pressure at different time steps during and after one pulse of stimulation: fracture view (left) and wellbore view (right)

Near-wellbore Stress and Fracture Closure Mechanism

In this section the evolution of the component of the total stress normal to the fracture plane, σ_{yy}, the fracture aperture, and fracture fluid pressure during the course of a single pressure pulse are discussed. The second stimulation cycle for case 2 is illustrated in Figure 4.9, in which the distribution of pressure along the fracture is also depicted by color contours on the fracture, the aperture of the fracture is magnified by a factor of 50, and the rock mass is colored by contours of σ_{yy}. The following states of stress are observed during the evolution of the hydraulic fractures due to a pressure pulse. *a) Initial stress state:* Figure 4.9(a) illustrates the stress concentration at the wellbore due to the interaction of the in-situ stresses and the well. Prior to the stimulation, the fracture is closed and the wellbore is in an equilibrium state with the *in situ* stress field and hydro-static pressure. The interaction of the wellbore with the *in situ* stress field generates a concentration of compressive stress around the wellbore. The fluid pressure has to overcome this stress concentration in order to open and propagate the fracture, as would be expected from the Kirsch equations [72].

b) Pressurization of the initial fracture: When the wellbore is pressurized, fluid pressure starts to develop along the fracture and the fracture opens from the wellbore towards the tip (Figure 4.9(b)). A tensile stress concentration develops at the physical tip and the cohesive zone develops. The physical tip moves towards the mathematical tip, leading to a smaller cohesive zone.

c) Pre-pressure Peak Fracture Propagation: Once the stress concentration at the fracture tip overcomes the tensile strength of the formation, hydraulic fracture propagates

(Figure 4.9(c)). During the fracture opening and propagation stages of the stimulation cycle, the region around the wellbore is under high compressive stresses (see Figure 4.9(b) and (c)).

d) Post-pressure Peak Fracture Propagation: Propagation continues after the pressure pulse reaches its maximum amplitude p_{max} (Figure 4.9(d)). The pressure in the fracture towards the fracture tip remains higher than the wellbore pressure and continues to drive fracture propagation. However, this reversal of the pressure gradient in the fracture, also leads to flow of fluid from the fracture back into the well. Due to leak-off, flow-back to the well, and fracture extension, the pressure everywhere in the fracture reduces over time and propagation stops.

e) Fracture Closure: At the onset of closure, high compressive stresses have built up along the fracture (Figure 4.9(e&f)). The fracture closes first at the wellbore; closure then propagates from the wellbore towards the tip. This occurs due to the initial compressive stress concentration at the well. Once closure at the wellbore occurs, flow-back of fluid into the well is significantly reduced, the impact of which is a rapid increase in the fluid pressure in the fracture. This increase in fluid pressure in the fracture accelerates fluid leak-off. Once the fracture is pinched-off at the well, the rate of fracture closure is controlled by the rate at which fluid leaks-off into the formation. The final drainage and complete closure of the fracture occurs under quasi-static equilibrium conditions. Once the fracture is completely closes equilibrium and the compressive stress concentrations at the wellbore are re-established.

A slightly different closure mechanism can be observed in a highly permeable formation

with very low bulk modulus. When wellbore pressure decreases, fluid leaks from the fracture into the formation at a very high rate that is almost uniformly along the whole length of the fracture. This results in closure initiating from the tip towards the wellbore. At a later times when pressure sufficiently decreases in the tip region due to the leak-off, a pinch point is seen at a location close to the wellbore (but not in its immediate vicinity). This pinch point is the point with the highest leak-off rate along the fracture. Closure extends from the pinch point towards the fracture tip and the wellbore, as time passes.

Wave Emission and Propagation

The stimulation of a wellbore with pressure pulses results in acoustic wave emissions. The emitted waves depend upon the response of the wellbore and the fractures.

Figure 4.10 illustrates the magnitude of solid velocity, for the second stimulation cycle of Case 2. For a complete stimulation cycle with the pressure pulse (4.18), six different emission patterns are observed.

a) Initial wellbore expansion: Upon pressurizing the wellbore, a radial wave front propagates away from the wellbore (Figure 4.10(a)). The emissions consist of dilation waves due to the expansion of the wellbore under fluid pressure.

b) Fracture opening: When pressure builds up in the wellbore, fluid flows into the fractures and opens them. Fracture deformation generates a wave front propagating from the fracture and causes the radial wave form to change. In the case shown in Figure 4.10(b), the fracture is aligned with the orientation of the maximum horizontal stress. Therefore, the dominant emission is a dilation wave resulted from the fracture opening. If

the fracture was inclined with respect to the *in situ* stress field, emissions from the fracture could contain a mix of dilation and shear waves.

c) Fracture propagation: The second wave pattern detected during the stimulation is the wave emitted from the fracture tip when it propagates (Figure 4.10(c)). Fracture propagation creates new fracture surfaces whose deformation generates new wave fronts. The pattern observed from these waves is similar to the one detected during fracture opening with the exception that this wave emits only from the fracture tip (i.e., from the new surfaces created as the fracture propagates).

d) Wellbore and fracture unloading: When pressure decreases, fluid starts to leak off from the fracture. Both wellbore and fracture deformations reverse and the system deforms to reach its equilibrium state. In this stage, fracture aperture is continuously decreasing, but the fracture is still open (Figure 4.10(d)).

e) Fracture closure and pressure rebuild in the fracture: When fracture closes at the wellbore, the contact between fracture surfaces on the closed portion of the fracture also generates wave emissions from the fracture. In addition, since the fluid pressure in the fracture goes up in the open portion of the fracture, the fracture is reloaded and slightly re-opens it. This mechanism generates a wave front propagating away from the fracture, which decays as fluid leaks off into the formation (Figure 4.10(e)).

f) Return to the equilibrium state: When sufficient time passes from the stimulation cycle (about 1 ms in the above simulations) The wellbore and pressure return to the equilibrium state and the emitted waves propagate away from the wellbore. No significant emissions from the wellbore is detected after this stage (Figure 4.10(f)).

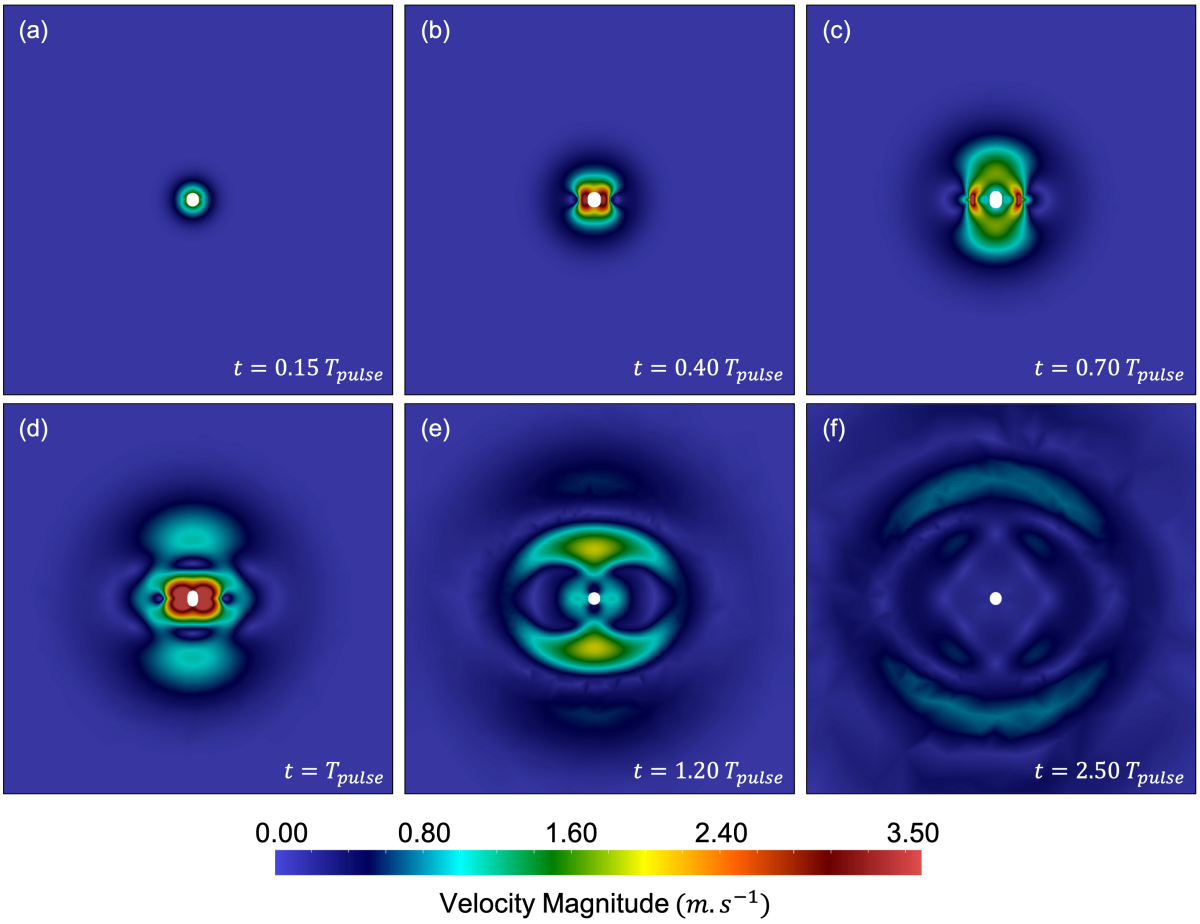

Figure 4.10: Contours of particle velocity magnitude indicating acoustic emissions from (a) Initial wellbore expansion, (b) Fracture opening, (c) Fracture propagation, (d) Wellbore and fracture unloading, (e) Fracture closure and pressure rebuild in the fracture, and (f) Return to the equilibrium state

4.4 Conclusions

The dynamic stimulation of a perforated wellbore drilled in a layered formation with a wide range of permeability and stiffness was investigated. The propagation of hydraulic fractures from the wellbore in different layers is also studied. The numerical model for

the fracture evolution was presented in the framework of the XFEM. The flow model was presented in the standard FEM framework. Wellbore stimulation was simulated under cyclic pressure-controlled and conditions.

Numerical simulations showed that the physical characteristics of hydraulic fractures are impacted by permeability and stiffness of the formation. High permeability formations develop short and wide fractures, whereas long narrow fractures are developed in low permeability formations.

The fracture closure mechanism is also affected by the formation permeability. In low permeability layers, fracture closure starts with a pinching at the wellbore and fracture closes from the wellbore to the tip. In high permeability layers, the fracture closes from the tip to the wellbore followed by a late time pinching in the middle of the fracture close to the wellbore.

The response of the wellbore and hydraulic fractures to the stimulation is detectable from the wave patterns emitted from the stimulated wellbore. Recognition of the emitted wave patterns can assist in the interpretation of recorded seismicity and recognition of the mechanisms involved in more complex hydraulic fracturing processes.

Chapter 5

Conclusions and Future Work

5.1 Conclusions

This PhD thesis had three objectives. The first objective of the thesis was to develop a stable sequential coupling algorithm for hydraulic fracture simulations using the analogy of the undrained split in poromechanics. The second objective of the thesis was to develop a stable sequential coupling algorithm for hydraulic fracture simulations using the analogy of the fixed stress split in poromechanics. The third objective of the thesis was to develop a dynamic hydraulic fracture model with leak-off for the simulation of dynamic wellbore stimulation using pressure pulses.

Chapter 1 presented an introduction to the hydraulic fracturing and reviewed hydraulic fracture models available in the literature. An overview of the available coupling algorithms for hydraulic fracture simulation was provided. A brief discussion of some of the current challenges in hydraulic fracture simulation and the objectives of this research to overcome these challenges was also provided. The methodologies used for fulfilling each of the objectives are also briefly discussed.

The first objective was realized in Chapter 2, in which a new sequential coupling algorithm for the simulation of hydraulically induced fractures was presented. The fracture was assumed to be replaced by an analogous porous medium, and the Biot's poroelasticity theory was employed to develop an iterative coupling algorithm that, at each iteration, solves the solid equation first. The algorithm was developed assuming an APM under undrained conditions and, hence, was named the undrained HF split. The developed coupling strategy was shown, through numerical examples, to be stable in the applications that the conventional drained HF coupling algorithm ($P \rightarrow W$) exhibits numerical insta-

bility. Solution of the undrained HF split converges to the solution of the fully coupled model; however, the undrained HF split was shown to require more iterations to converge.

The second objective was realized in Chapter 3, in which the derivation of a second new iterative coupling algorithm for the simulation of hydraulic fractures was elaborated. The algorithm was developed based on the analogy of the fixed stress split in poromechanics, which at each iteration, solves the fluid subproblem first. Similar to the undrained HF split, the hydraulic fracture was assumed to be replaced by an APM and the fixed stress HF split was developed using Biot theory. Through numerical examples, the fixed stress HF split was shown to be stable and to converge to the solution of the fully coupled model. Chapter 3 also presented an algorithm for the automatic partitioning of the injected fluid between fractures. The algorithm was developed based on the satisfaction of the global conservation of mass. The efficiency of the automatic partitioning algorithm was also demonstrated through numerical examples in Chapter 3.

The third objective was realized in Chapter 4, in which, a dynamic hydraulic fracture model was developed using the fully coupled solution strategy. A one dimensional leak-off model was implemented to account for fluid leak-off from the fractures. The model was used to investigate the effects of formation porosity and permeability on the response of wellbore and hydraulic fractures to short-period pressure pulses. Fracture closure mechanisms, stress perturbation near the wellbore and the alteration of fluid pressure within fractures were explained. Propagation of the emitted waves from the wellbore and hydraulic fractures were also discussed.

In addition to the rapidly changing hydraulic loads, such as short-period pressure pulses,

the dynamic hydraulic fracture model developed in this research is capable of simulating dynamic mechanical loads, such as impact. Rapidly changing mechanical loads are generated, for example, during wellbore perforation or when nearby wellbores are dynamically stimulated. The emitted wave patterns, near wellbore stress perturbation due to dynamic mechanical loads, and the dynamic response of hydraulically induced fractures can be studied using the dynamic hydraulic fracture model presented in Chapter 4. Stress shadowing and the effect of pressurized fractures on the propagation of adjacent hydraulic fractures can also be investigated using the hydraulic fracture model developed in this research.

5.2 Future Work

The following potential topics are suggested for the extension of the research performed in this PhD dissertation.

- A complementary study on the convergence and stability of the proposed undrained and fixed stress HF splits and a parametric study of the two algorithms by comparing the results of the undrained HF split and the fixed stress HF split
- Optimization of the flow partitioning algorithm by implementing an optimization algorithm that automatically calculates the optimum correction coefficient
- Verification of the results obtained by the proposed numerical algorithms in this research with similar numerical simulations and available semi-analytical models
- The coupling algorithms provided in this research are capable of being extended to incorporate the coupling of other physical processes, such as proppant transport, and thermal and chemical processes involved in hydraulic fracturing
- Extending the dynamic/quasi-static models presented in this research to two- and three-dimensional poromechanics
- Extending the fluid model to a dynamic model that accounts for the inertial effects in the fluid would be a challenging but valuable contribution

References

[1] S. Abbas, E. Gordeliy, A. Peirce, B. Lecampion, D. Chuprakov, and R. Prioul. Limited height growth and reduced opening of hydraulic fractures due to fracture offsets: An XFEM application. In *Society of Petroleum Engineers - SPE Hydraulic Fracturing Technology Conference 2014*, pages 587–599, 2014.

[2] J. Adachi, E. Siebrits, A. Peirce, and J. Desroches. Computer simulation of hydraulic fractures. *International Journal of Rock Mechanics and Mining Sciences*, 44(5):739–757, 2007.

[3] S.H. Advani, T.S. Lee, and J.K. Lee. Three-dimensional modeling of hydraulic fractures in layered media. Part I. Finite element formulations. *Journal of Energy Resources Technology, Transactions of the ASME*, 112(1):1–9, 1990.

[4] Alberta Energy Regulator. What is Hydraulic Fracturing?, Alberta Energy Regulator, 2016.

[5] Alberta Energy Regulator. What is unconventional oil and gas?, Alberta Energy Regulator, 2016.

[6] A.A. Andreev, A.N. Galybin, and O.Y. Izvekov. Modelling of hydraulic fractures trajectories in inhomogeneous stress field. In *Poromechanics V - Proceedings of the 5th Biot Conference on Poromechanics*, pages 2344–2350, 2013.

[7] R. Asadi and B. Ataie-Ashtiani. A comparison of finite volume formulations and coupling strategies for two-phase flow in deforming porous media. *Computers and Geotechnics*, 67:17–32, 2015.

[8] R. Asadi and B. Ataie-Ashtiani. Numerical modeling of subsidence in saturated porous media: A mass conservative method. *Journal of Hydrology*, 542:423–436, 2016.

[9] K. Atefi Monfared and L. Rothenburg. Poro-elasto-plastic response of an unconsolidated formation confined with stiff seal rocks under radial injection. *International Journal for Numerical and Analytical Methods in Geomechanics*, 40(13):1799–1826, 2016.

[10] I. Babuška. The finite element method with lagrangian multipliers. *Numerische Mathematik*, 20(3):179–192, 1973.

[11] O.R. Barani, A.R. Khoei, and M. Mofid. Modeling of cohesive crack growth in partially saturated porous media; A study on the permeability of cohesive fracture. *International Journal of Fracture*, 167(1):15–31, 2011.

[12] G.I. Barenblatt. *The Mathematical Theory of Equilibrium Cracks in Brittle Fracture*, volume 7 of *Advances in Applied Mechanics*. 1962.

[13] K.-J. Bathe. The inf-sup condition and its evaluation for mixed finite element methods. *Computers & Structures*, 79(2):243 – 252, 2001.

[14] T. Belytschko, N. Moës, S. Usui, and C. Parimi. Arbitrary discontinuities in finite elements. *International Journal for Numerical Methods in Engineering*, 50(4):993–1013, 2001.

[15] T.J. Boone and A.R. Ingraffea. A numerical procedure for simulation of hydraulicallydriven fracture propagation in poroelastic media. *International Journal for Numerical and Analytical Methods in Geomechanics*, 14(1):27–47, 1990.

[16] T.J. Boone, A.R. Ingraffea, and J.-C. Roegiers. Simulation of hydraulic fracture propagation in poroelastic rock with application to stress measurement techniques. *International Journal of Rock Mechanics and Mining Sciences and*, 28(1):1–14, 1991.

[17] E.C. Bryant, J. Hwang, and M.M. Sharma. Arbitrary fracture propagation in heterogeneous poroelastic formations using a finite volume-based cohesive zone model. pages 687–703. Society of Petroleum Engineers, 2015. cited By 13.

[18] T.D. Cao, F. Hussain, and B.A. Schrefler. Porous media fracturing dynamics: stepwise crack advancement and fluid pressure oscillations. *Journal of the Mechanics and Physics of Solids*, 111:113–133, 2018.

[19] B. Carrier and S. Granet. Numerical modeling of hydraulic fracture problem in permeable medium using cohesive zone model. *Engineering Fracture Mechanics*, 79:312–328, 2012.

[20] B.J. Carter, J. Desroches, A.R. Ingraffea, and P.A. Wawrzynek. Simulating fully 3D hydraulic fracturing. Modeling in geomechanics. Wiley Publishers, New York, 2000.

[21] C. Chang, M.D. Zoback, and A. Khaksar. Empirical relations between rock strength and physical properties in sedimentary rocks. *Journal of Petroleum Science and Engineering*, 51(3-4):223–237, 2006.

[22] E. Chekhonin and K. Levonyan. Hydraulic fracture propagation in highly permeable formations, with applications to tip screenout. *International Journal of Rock Mechanics and Mining Sciences*, 50:19–28, 2012.

[23] Z. Chen, M. Chen, Y. Jin, and R. Huang. Determination of rock fracture toughness and its relationship with acoustic velocity. *International Journal of Rock Mechanics and Mining Sciences*, 34(049):3–4, 1997.

[24] S. Cherny, V. Lapin, D. Esipov, D. Kuranakov, A. Avdyushenko, A. Lyutov, and P. Karnakov. Simulating fully 3D non-planar evolution of hydraulic fractures. *International Journal of Fracture*, 201(2):181–211, 2016.

[25] S.R. Chowdhury and R. Narasimhan. A cohesive finite element formulation for modelling fracture and delamination in solids. *Sadhana*, 25(6):561–587, 2000.

[26] R.J. Clifton and A.S. Abou-Sayed. Variational approach to the prediction of the three-dimensional geometry of hydraulic fractures. *Society of Petroleum Engineers of AIME, (Paper) SPE*, pages 457–465, 1981.

[27] R.J. Clifton and J.-J. Wang. Robust mesh generation for areas with advancing boundaries. In *Computers in Engineering, Proceedings of the International Computers in Engineering Conference and Exhibit*, volume 2, pages 23–28, 1992.

[28] B.C. Crittendon. The Mechanics of Design and Interpretation of Hydraulic Fracture Treatments. 1959.

[29] P.A. Cundall and O.D.L. Strack. Discrete numerical model for granular assemblies. *Geotechnique*, 29(1):47–65, 1979.

[30] A. Dahi Taleghani, M. Gonzalez, and A. Shojaei. Overview of numerical models for interactions between hydraulic fractures and natural fractures: Challenges and limitations. *Computers and Geotechnics*, 71:361–368, 2016.

[31] A.A. Daneshy. On the Design of Vertical Hydraulic Fractures. 1973.

[32] V. de la Cruz and T.J.T. Spanos. Thermomechanical coupling during seismic wave propagation in a porous medium. *Journal of Geophysical Research: Solid Earth*, 94(B1):637–642, 1989.

[33] R.H. Dean and J.H. Schmidt. Hydraulic-fracture predictions with a fully coupled geomechanical reservoir simulator. *SPE Journal*, 14(4):707–714, 2009.

[34] U.S. Energy Department. Annual Energy Outlook, 2016.

[35] E. Detournay. Propagation regimes of fluid-driven fractures in impermeable rocks. *International Journal of Geomechanics*, 4(1):35–45, 2004.

[36] E. Dontsov and A. Peirce. A Lagrangian Approach to Modelling Proppant Transport with Tip Screen-Out in KGD Hydraulic Fractures. *Rock Mechanics and Rock Engineering*, 48(6):2541–2550, 2015.

[37] E. Dontsov and A. Peirce. A multiscale Implicit Level Set Algorithm (ILSA) to model hydraulic fracture propagation incorporating combined viscous, toughness, and leak-off asymptotics. *Computer Methods in Applied Mechanics and Engineering*, 313:53–84, 2017.

[38] E.V. Dontsov. An approximate solution for a plane strain hydraulic fracture that accounts for fracture toughness, fluid viscosity, and leak-off. *International Journal of Fracture*, 205(2):221–237, 2017.

[39] M.B. Dusseault. Geomechanical Aspects of Shale Gas Development, 2013.

[40] M. Faivre, B. Paul, F. Golfier, R. Giot, P. Massin, and D. Colombo. 2D coupled HM-XFEM modeling with cohesive zone model and applications to fluid-driven fracture network. *Engineering Fracture Mechanics*, 159:115–143, 2016.

[41] W. Ferguson, G. Richards, A. Bere, U. Mutlu, and F. Paw. Modelling near-wellbore hydraulic fracture branching, complexity and tortuosity: A case study based on a fully coupled geomechanical modelling approach. Society of Petroleum Engineers, 2018. cited By 2.

[42] F. Frezzi. On the existence, uniqueness and approximation of saddle-point problems arising from lagrangian multipliers. *Revue francaise d'automatique, informatique, recherche opera- tionnelle. Analyse numerique*, 8:129–151, 1974.

[43] T.-P. Fries. A corrected XFEM approximation without problems in blending elements. *International Journal for Numerical Methods in Engineering*, 75(5):503–532, 2008.

[44] W. Fu, A.A. Savitski, B. Damjanac, and A.P. Bunger. Three-dimensional lattice simulation of hydraulic fracture interaction with natural fractures. *Computers and Geotechnics*, 107:214–234, 2019. cited By 0.

[45] D.I. Garagash. Plane-strain propagation of a fluid-driven fracture during injection and shut-in: Asymptotics of large toughness. *Engineering Fracture Mechanics*, 73(4):456–481, 2006. cited By 63.

[46] D.I. Garagash and E. Detournay. Plane-strain propagation of a fluid-driven fracture: Small toughness solution. *Journal of Applied Mechanics, Transactions ASME*, 72(6):916–928, 2005. cited By 78.

[47] J. Geertsma and F. de Klerk. A Rapid Method of Predicting Width and Extent of Hydraulically Induced Fractures. 1969.

[48] J. Geertsma and F. De Klerk. A Rapid Method of Predicting Width and Extent of Hydraulically Induced Fractures. *Journal of Petroleum Technology*, 21(12):1571–1581, 1969.

[49] P.H. Geubelle and J.S. Baylor. Impact-induced delamination of composites: A 2D simulation. *Composites Part B: Engineering*, 29(5):589–602, 1998.

[50] A. Ghaderi, J. Taheri-Shakib, and M.A. Sharif Nik. The distinct element method (DEM) and the extended finite element method (XFEM) application for analysis of interaction between hydraulic and natural fractures. *Journal of Petroleum Science and Engineering*, 171(June 2017):422–430, 2018.

[51] E. Gordeliy and E. Detournay. A fixed grid algorithm for simulating the propagation of a shallow hydraulic fracture with a fluid lag. *International Journal for Numerical and Analytical Methods in Geomechanics*, 35:602–629, 2011.

[52] E. Gordeliy and A. Peirce. Coupling schemes for modeling hydraulic fracture propagation using the XFEM. *Computer Methods in Applied Mechanics and Engineering*, 253:305–322, 2013.

[53] E. Gordeliy and A. Peirce. Implicit level set schemes for modeling hydraulic fractures using the XFEM. *Computer Methods in Applied Mechanics and Engineering*, 266:125–143, 2013.

[54] E. Gordeliy and A. Peirce. Enrichment strategies and convergence properties of the XFEM for hydraulic fracture problems. *Computer Methods in Applied Mechanics and Engineering*, 283:474–502, 2015.

[55] A.C. Gringarten, H.J. Ramey, and R. Raghavan. Unsteady-State Pressure Distributions Created by a Well With a Single Infinite-Conductivity Vertical Fracture. *Society of Petroleum Engineers Journal*, 14(04):347–360, 1974.

[56] P. Gupta and C.A. Duarte. Simulation of non-planar three-dimensional hydraulic fracture propagation. *International Journal for Numerical and Analytical Methods in Geomechanics*, 38(13):1397–1430, 2014.

[57] P. Gupta and C.A. Duarte. Coupled formulation and algorithms for the simulation of non-planar three-dimensional hydraulic fractures using the generalized finite element method. *International Journal for Numerical and Analytical Methods in Geomechanics*, 40(10):1402–1437, 2016.

[58] S. Ham and K.-J. Bathe. A finite element method enriched for wave propagation problems. *Computers & Structures*, 9495:1–12, 2012.

[59] E. Harrison, W.F. Kieschnick, and W.J. McGuire. The Mechanics of Fracture Induction and Extension, 1954.

[60] G. Hattori, J. Trevelyan, C.E. Augarde, W.M. Coombs, and A.C. Aplin. Numerical Simulation of Fracking in Shale Rocks: Current State and Future Approaches. *Archives of Computational Methods in Engineering*, 24(2):281–317, 2017.

[61] B. He. Hydromechanical model for hydraulic fractures using XFEM. *Frontiers of Structural and Civil Engineering*, pages 1–10, 2018.

[62] Z. He and B. Duan. Significance of the dynamic stress perturbations induced by hydraulic fracturing. *Journal of Petroleum Science and Engineering*, 174(November 2018):169–176, 2019.

[63] M. Hossain and M.K. Rahman. Numerical simulation of complex fracture growth during tight reservoir stimulation by hydraulic fracturing. *Journal of Petroleum Science and Engineering*, 60(2):86–104, 2008.

[64] G.C. Howard and C.R. Fast. Optimum Fluid Characteristics for Fracture Extension, 1957.

[65] G. hua Shi and R.E. Goodman. Discontinuous Deformation Analysis - A New Method Forcomputing Stress, Strain And Sliding Of Block Systems, 1988.

[66] M.K. Hubbert and D.G. Willis. Mechanics Of Hydraulic Fracturing, 1957.

[67] A.R. Khoei, O.R. Barani, and M. Mofid. Modeling of dynamic cohesive fracture propagation in porous saturated media. *International Journal for Numerical and Analytical Methods in Geomechanics*, 35(10):1160–1184, 2011.

[68] A.R. Khoei, M. Hirmand, M. Vahab, and M. Bazargan. An enriched FEM technique for modeling hydraulically driven cohesive fracture propagation in impermeable media with frictional natural faults: Numerical and experimental investigations. *International Journal for Numerical Methods in Engineering*, 104(6):439–468, 2015.

[69] A.R. Khoei, M. Vahab, and M. Hirmand. Modeling the interaction between fluid-driven fracture and natural fault using an enriched-FEM technique. *International Journal of Fracture*, 197(1):1–24, 2016.

[70] J. Kim, H.A. Tchelepi, and R. Juanes. Stability and convergence of sequential methods for coupled flow and geomechanics: Drained and undrained splits. *Computer Methods in Applied Mechanics and Engineering*, 200(23-24):2094–2116, 2011.

[71] J. Kim, H.A. Tchelepi, and R. Juanes. Stability and convergence of sequential methods for coupled flow and geomechanics: Fixed-stress and fixed-strain splits. *Computer Methods in Applied Mechanics and Engineering*, 200(13-16):1591–1606, 2011.

[72] G. Kirsch. *Die Theorie der Elastizität und die Bedürfnisse der Festigkeitslehre*. Springer, 1898.

[73] M. Komijani and R. Gracie. An enriched finite element model for wave propagation in fractured media. *Finite Elements in Analysis and Design*, 125(November 2016):14–23, 2017.

[74] M. Komijani and R. Gracie. Enriched mixed finite element models for dynamic analysis of continuous and fractured porous media. *Computer Methods in Applied Mechanics and Engineering*, 343:74–99, 2019. cited By 0.

[75] M. Komijani, R. Gracie, and E. Sarvaramini. Simulation of induced acoustic emission in fractured porous media. *Engineering Fracture Mechanics*, 2018. cited By 1; Article in Press.

[76] E.J.L. Koning. *Waterflooding under fracturing conditions*. PhD thesis, Technical University of Delft, 1988.

[77] O.A. Ladyzhenskaya. *The mathematical theory of viscous incompressible flow*. Gordon and Breach, New York, 1969.

[78] B. Lecampion. An extended finite element method for hydraulic fracture problems. *Communications in Numerical Methods in Engineering*, 25(2):121–133, 2009.

[79] B. Lecampion, A. Bunger, and X. Zhang. Numerical methods for hydraulic fracture propagation: A review of recent trends. *Journal of Natural Gas Science and Engineering*, 49(July 2017):66–83, 2018.

[80] B. Lecampion and J. Desroches. Simultaneous initiation and growth of multiple radial hydraulic fractures from a horizontal wellbore. *Journal of the Mechanics and Physics of Solids*, 82:235–258, 2015.

[81] B. Lecampion and E. Detournay. An implicit algorithm for the propagation of a hydraulic fracture with a fluid lag. *Computer Methods in Applied Mechanics and Engineering*, 196(49-52):4863–4880, 2007.

[82] B. Lecampion, A. Peirce, E. Detournay, X. Zhang, Z. Chen, A. Bunger, C. Detournay, J. Napier, S. Abbas, D. Garagash, and P. Cundall. The impact of the near-tip logic on the accuracy and convergence rate of hydraulic fracture simulators compared to reference solutions. In Andrew P. Bunger, John McLennan, and Rob Jeffrey, editors, *Effective and Sustainable Hydraulic Fracturing*, chapter 43. IntechOpen, Rijeka, 2013.

[83] S. Lee, M.F. Wheeler, and T. Wick. Pressure and fluid-driven fracture propagation in porous media using an adaptive finite element phase field model. *Computer Methods in Applied Mechanics and Engineering*, 305:111–132, 2016.

[84] C. Li, V.T. Chau, H. Xie, and Z.P. Baant. Recent advances in mechanics of fracking and new results on 2d simulation of crack branching in anisotropic gas or oil shale. *Acta Mechanica*, 229(2):975–992, 2018. cited By 0.

[85] A. Lisjak and G. Grasselli. A review of discrete modeling techniques for fracturing processes in discontinuous rock masses. *Journal of Rock Mechanics and Geotechnical Engineering*, 6(4):301–314, 2014.

[86] M.G. Mack and N.R. Warpinski. Mechanics of hydraulic fracturing. Reservoir Stimulation. Wiley, Chichester, 3 edition, 2000.

[87] O.K. Mahabadi, N.X. Randall, Z. Zong, and G. Grasselli. A novel approach for micro-scale characterization and modeling of geomaterials incorporating actual material heterogeneity. *Geophysical Research Letters*, 39(1), 2012.

[88] G. Meschke and D. Leonhart. A Generalized Finite Element Method for hydro-mechanically coupled analysis of hydraulic fracturing problems using space-time variant enrichment functions. *Computer Methods in Applied Mechanics and Engineering*, 290:438–465, 2015.

[89] C. Miehe and S. Mauthe. Phase field modeling of fracture in multi-physics problems. Part III. Crack driving forces in hydro-poro-elasticity and hydraulic fracturing of fluid-saturated porous media. *Computer Methods in Applied Mechanics and Engineering*, 304:619–655, 2016.

[90] C. Miehe, S. Mauthe, and S. Teichtmeister. Minimization principles for the coupled problem of Darcy-Biot-type fluid transport in porous media linked to phase field modeling of fracture. *Journal of the Mechanics and Physics of Solids*, 82:186–217, 2015.

[91] A. Mikelić, B. Wang, and M.F. Wheeler. Numerical convergence study of iterative coupling for coupled flow and geomechanics. *Computational Geosciences*, 18(3-4):325–341, 2014.

[92] A. Mikelić and M.F. Wheeler. Convergence of iterative coupling for coupled flow and geomechanics. *Computational Geosciences*, 17(3):455–461, 2013.

[93] A. Mikelić, M.F. Wheeler, and T. Wick. A phase-field method for propagating fluid-filled fractures coupled to a surrounding porous medium. *Multiscale Modeling & Simulation*, 13(1):367–398, 2015.

[94] M.E. Mobasher, L. Berger-Vergiat, and H. Waisman. Non-local formulation for transport and damage in porous media. *Computer Methods in Applied Mechanics and Engineering*, 324:654–688, 2017.

[95] N. Moës and T. Belytschko. Extended finite element method for cohesive crack growth. *Engineering Fracture Mechanics*, 69(7):813–833, 2002.

[96] N. Moes, J. Dolbow, and T. Belytschko. A finite element method for crack growth without remeshing. *International Journal for Numerical Methods in Engineering*, 46(1):131–150, 1999.

[97] S.G. Mogilevskaya. Numerical modeling of 2-D smooth crack growth. *International Journal of Fracture*, 87(4):389–405, 1997.

[98] S.G. Mogilevskaya, L. Rothenburg, and M.B. Dusseault. Growth of pressure-induced fractures in the vicinity of a wellbore. *International Journal of Fracture*, 104(4):25–30, 2000.

[99] T. Mohammadnejad and J.E. Andrade. Numerical modeling of hydraulic fracture propagation, closure and reopening using XFEM with application to in-situ stress estimation. *International Journal for Numerical and Analytical Methods in Geomechanics*, 40(15):2033–2060, 2016.

[100] T. Mohammadnejad and A.R. Khoei. An extended finite element method for hydraulic fracture propagation in deformable porous media with the cohesive crack model. *Finite Elements in Analysis and Design*, 73:77–95, 2013.

[101] T. Mohammadnejad and A.R. Khoei. Hydro-mechanical modeling of cohesive crack propagation in multiphase porous media using the extended finite element method. *International Journal for Numerical and Analytical Methods in Geomechanics*, 37(10):1247–1279, 2013.

[102] R.P. Nordgren. Propagation of a Vertical Hydraulic Fracture. 1972.

[103] M. Ortiz and A. Pandolfi. Finite-deformation irreversible cohesive elements for three-dimensional crack-propagation analysis. *International Journal for Numerical Methods in Engineering*, 44(9):1267–1282, 1999.

[104] P. Papanastasiou. The influence of plasticity in hydraulic fracturing. *International Journal of Fracture*, 84(1):61–79, 1997.

[105] P. Papanastasiou and M. Thiercelin. Influence of inelastic rock behaviour in hydraulic fracturing. *International Journal of Rock Mechanics and Mining Sciences and*, 30(7):1241–1247, 1993.

[106] A. Peirce. Modeling multi-scale processes in hydraulic fracture propagation using the implicit level set algorithm. *Computer Methods in Applied Mechanics and Engineering*, 283:881–908, 2015.

[107] A. Peirce. Implicit level set algorithms for modelling hydraulic fracture propagation. *Philosophical Transactions of the Royal Society A: Mathematical, Physical and Engineering Sciences*, 374(2078), 2016.

[108] A. Peirce and E. Detournay. An implicit level set method for modeling hydraulically driven fractures. *Computer Methods in Applied Mechanics and Engineering*, 197(33-40):2858–2885, 2008.

[109] A.P. Peirce and A.P. Bunger. Interference fracturing: Nonuniform distributions of perforation clusters that promote simultaneous growth of multiple hydraulic fractures. *SPE Journal*, 20(2):384–395, 2015.

[110] T.K. Perkins and L.R. Kern. Widths of Hydraulic Fractures. 1961.

[111] A. Pirayehgar and M.B. Dusseault. Simulation of Naturally Fractured Hard Rock Preconditioning via Hydraulic Fracturing, 2015.

[112] Hartley P.R. and K.B. Medlock. Energy Market Consequences of Emerging Renewable Eneregy and Carbon Dioxide Abatement Policies in the United States. *Energy Forum of the James A. Baker III Institute for Public Policy, Rice University*, 2010.

[113] M. Profit, M. Dutko, J. Yu, S. Cole, D. Angus, and A. Baird. Complementary hydro-mechanical coupled finite/discrete element and microseismic modelling to predict hydraulic fracture propagation in tight shale reservoirs. *Computational Particle Mechanics*, 3(2):229–248, 2016.

[114] M.L. Profit, M. Dutko, J. Yu, J.A. Armstrong, D. Parfitt, and U. Mutlu. Application of State of the Art Hydraulic Fracture Modelling Techniques for Safe-Optimized Design and for Enhanced Production. In *50th US Rock Mechanics / Geomechanics Symposium held in Houston, Texas, USA, 26-29 June 2016*. American Rock Mechanics Association, 2016.

[115] J. Rethore, R. Borst, and M.-A. Abellan. A two-scale model for fluid flow in an unsaturated porous medium with cohesive cracks. *Computational Mechanics*, 42(2):227–238, 2008.

[116] J. Rungamornrat, M.F. Wheeler, and M.E. Mear. A numerical technique for simulating nonplanar evolution of hydraulic fractures. In *Proceedings - SPE Annual Technical Conference and Exhibition*, pages 3813–3821. Society of Petroleum Engineers, 2005.

[117] J. Rungamornrat, M.F. Wheeler, and M.E. Mear. SGBEM/FEM for non-planar evolution of hydraulic fractures in 3D elastic media. In *67th European Association of Geoscientists and Engineers, EAGE Conference and Exhibition, incorporating SPE EUROPE2005 - Extended Abstracts*, volume 67th Europ, pages 3135–3138, 2005.

[118] P.N. Sahay, T.J.T. Spanos, and V. De La Cruz. Seismic wave propagation in inhomogeneous and anisotropic porous media. *Geophysical Journal International*, 145(1):209–222, 2001. cited By 31.

[119] S. Salimzadeh and N. Khalili. A three-phase XFEM model for hydraulic fracturing with cohesive crack propagation. *Computers and Geotechnics*, 69:82–92, 2015.

[120] S. Salimzadeh, A. Paluszny, and R.W. Zimmerman. Three-dimensional poroelastic effects during hydraulic fracturing in permeable rocks. *International Journal of Solids and Structures*, 108:153–163, 2017.

[121] D. Santillán, R. Juanes, and L. Cueto-Felgueroso. Phase field model of fluid-driven fracture in elastic media: Immersed-fracture formulation and validation with analytical solutions. *Journal of Geophysical Research: Solid Earth*, 122(4):2565–2589, 2017.

[122] D. Santilln, R. Juanes, and L. Cueto-Felgueroso. Phase field model of hydraulic fracturing in poroelastic media: Fracture propagation, arrest, and branching under fluid injection and extraction. *Journal of Geophysical Research: Solid Earth*, 123(3):2127–2155, 2018. cited By 1.

[123] E. Sarris and P. Papanastasiou. Modeling of Hydraulic Fracturing in a Poroelastic Cohesive Formation. *International Journal of Geomechanics*, 12(2):160–167, 2012.

[124] E. Sarris and P. Papanastasiou. Numerical modeling of fluid-driven fractures in cohesive poroelastoplastic continuum. *International Journal for Numerical and Analytical Methods in Geomechanics*, 37:1822–1846, 2013.

[125] E. Sarvaramini, M.B. Dusseault, and R. Gracie. Characterizing the stimulated reservoir volume during hydraulic fracturing-connecting the pressure fall-off phase to the geomechanics of fracturing. *Journal of Applied Mechanics, Transactions ASME*, 85(10), 2018.

[126] E. Sarvaramini, M.B. Dusseault, M. Komijani, and R. Gracie. A non-local plasticity model of stimulated volume evolution during hydraulic fracturing. *International Journal of Solids and Structures*, 2018. cited By 0; Article in Press.

[127] A. Settari. Simulation of Hydraulic Fracturing Processes. *Society of Petroleum Engineers Journal*, 20(06):487–500, 1980.

[128] E. Siebrits and A. Peirce. A efficient multi-layer planar 3D fracture growth algorithm using a fixed mesh approach. *International Journal for Numerical Methods in Engineering*, 53(3):691–717, 2002.

[129] I.N. Sneddon. The Distribution of Stress in the Neighbourhood of a Crack in an Elastic Solid. *Proc R Soc Lond A Math Phys Sci*, 187(1009):229, 1946.

[130] I.N. Sneddon and H.A. Elliot. The opening of a Griffith crack under internal pressure. *Quarterly of Applied Mathematics*, 4:262–267, 1946.

[131] J.L. Sousa, B.J. Carter, and A.R. Ingraffea. Numerical simulation of 3D hydraulic fracture using Newtonian and power-law fluids. *International Journal of Rock Mechanics and Mining Sciences and*, 30(7):1265–1271, 1993.

[132] T. Spanos, B. Davidson, M.B. Dusseault, D. Shand, and M. Samaroo. Pressure pulsing at the reservoir scale: A new IOR approach. *Journal of Canadian Petroleum Technology*, 42(2):16–27, 2003.

[133] D.A. Spence and P. Sharp. Self-similar solutions for elastohydrodynamic cavity flow. *Proceedings of the Royal Society of London, Series A: Mathematical and Physical Sciences*, 400(1819):289–313, 1985.

[134] Y. Su, L. Ren, F. Meng, C. Xu, and W. Wang. Theoretical Analysis of the Mechanism of Fracture Network Propagation with Stimulated Reservoir Volume (SRV) Fracturing in Tight Oil Reservoirs. *PLoS ONE*, 10(5):e0125319, 2015.

[135] N. Sukumar, D.L. Chopp, E. Bechet, and N. Moes. Three-dimensional non-planar crack growth by a coupled extended finite element and fast marching method. *International Journal for Numerical Methods in Engineering*, 76(5):727–748, 2008.

[136] S. Thallak, L. Rothenburg, and M.B. Dusseault. Hydraulic fracture (parting) simulation in granular assemblies using the discrete element method. *ASORTA Journal of Reseach*, 6:141–152, 1991.

[137] S. Thallak, L. Rothenburg, and M.B. Dusseault. Simulation of multiple hydraulic fractures in a discrete element. *Rock Mechanics as a Multidisciplinary Science*, 1991.

[138] M. Vahab, S. Akhondzadeh, A.R. Khoei, and N. Khalili. An X-FEM investigation of hydro-fracture evolution in naturally-layered domains. *Engineering Fracture Mechanics*, 191(November 2017):187–204, 2018.

[139] P.P. Valko and M.J. Economides. Fluid-Leakoff Delineation in High-Permeability Fracturing. *SPE Production & Facilities*, 14(02):110–116, 1997.

[140] P.J. Van Den Hoek. A Simple and Accurate Description of Non-linear Fluid Leak-off in High-Permeability Fracturing. Dallas, Texas, 2000. Society of Petroleum Engineers.

[141] L. Vandamme and J.H. Curran. A three-dimensional hydraulic fracturing simulator. *International Journal for Numerical Methods in Engineering*, 28(4):909–927, 1989.

[142] M. Wangen. Finite element modeling of hydraulic fracturing on a reservoir scale in 2D. *Journal of Petroleum Science and Engineering*, 77(3-4):274–285, 2011.

[143] X. Weng, O. Kresse, C. Cohen, R. Wu, and H. Gu. Modeling of Hydraulic Fracture Network Propagation in a Naturally Fractured Formation. *Simulation*, i(November):368–380, 2011.

[144] B.W. White, O.Y. Vorobiev, and S.D.C. Walsh. Modeling dynamic stimulation of geological resources. *48th US Rock Mechanics / Geomechanics Symposium 2014*, 1, 2014.

[145] Z.A. Wilson and C.M. Landis. Phase-field modeling of hydraulic fracture. *Journal of the Mechanics and Physics of Solids*, 96:264–290, 2016.

[146] G. Xu and S.-W. Wong. Interaction of multiple non-planar hydraulic fractures in horizontal wells. In *Society of Petroleum Engineers - International Petroleum Technology Conference 2013, IPTC 2013: Challenging Technology and Economic Limits to Meet the Global Energy Demand*, volume 6, pages 4693–4702, 2013.

[147] K. Yamamoto, T. Shimamoto, and S. Sukemura. Multiple fracture propagation model for a three-dimensional hydraulic fracturing simulator. *International Journal of Geomechanics*, 4(1):46–57, 2004.

[148] C. Yan and H. Zheng. Three-Dimensional Hydromechanical Model of Hydraulic Fracturing with Arbitrarily Discrete Fracture Networks using Finite-Discrete Element Method. *International Journal of Geomechanics*, 17(6):1–26, 2016.

[149] Y. Yao, L. Liu, and L.M. Keer. Pore pressure cohesive zone modeling of hydraulic fracture in quasi-brittle rocks. *Mechanics of Materials*, 83:17–29, 2015.

[150] C.H. Yew and X. Weng. Chapter 1 - Fracturing of a wellbore and 2D fracture models. Mechanics of Hydraulic Fracturing (Second Edition), pages 1–22. Gulf Professional Publishing, Boston, 2015.

[151] S.Y. Yi and M.L. Bean. Iteratively coupled solution strategies for a four-field mixed finite element method for poroelasticity. *International Journal for Numerical and Analytical Methods in Geomechanics*, 41(2):159–179, 2017.

[152] Z.Q. Yue, H.T. Xiao, L.G. Tham, C.F. Lee, and E. Pan. Boundary element analysis of three-dimensional crack problems in two joined transversely isotropic solids. *Computational Mechanics*, 36(6):459–474, 2005.

[153] X. Zhang and R.G. Jeffrey. Role of overpressurized fluid and fluid-driven fractures in forming fracture networks. *Journal of Geochemical Exploration*, 144(PA):194–207, 2014.

[154] X. Zhang, R.G. Jeffrey, A.P. Bunger, and M. Thiercelin. Initiation and growth of a hydraulic fracture from a circular wellbore. *International Journal of Rock Mechanics and Mining Sciences*, 48(6):984–995, 2011.

[155] X. Zhang, R.G. Jeffrey, and M. Thiercelin. Deflection and propagation of fluid-driven fractures at frictional bedding interfaces: A numerical investigation. *Journal of Structural Geology*, 29(3):396–410, 2007.

[156] A.K. Zheltov. 3. Formation of Vertical Fractures by Means of Highly Viscous Liquid, 1955.

[157] G. Zi and T. Belytschko. New crack-tip elements for XFEM and applications to cohesive cracks. *International Journal for Numerical Methods in Engineering*, 57(15):2221–2240, 2003.

[158] G. Zi, H. Chen, J. Xu, and T. Belytschko. The extended finite element method for dynamic fractures. *Shock and Vibration*, 12(2005):9–23, 2005.

[159] O.C. Zienkiewicz and A.H.C. Chan. *Coupled Problems and Their Numerical Solution*, pages 139–176. Springer Vienna, Vienna, 1989.